UNIVERSIDAD DE INVESTIGACIÓN DE TECNOLOGÍA EXPERIMENTAL YACHAY

Escuela de Ciencias Químicas e Ingeniería

Using mining industry wastewater to obtain Prussian blue analogues-silica monolith hybrids: a key to reduce water pollution

Trabajo de integración curricular presentado como requisito para la obtención del título de Química

Autor:

Kimberly Fernanda Montesdeoca Arredondo

Tutora:

Ph.D. Sommer-Marquez Alicia

Co-tutor:

Ph.D. Saucedo Juan Pablo

Urcuquí, Enero 2022

SECRETARÍA GENERAL
(Vicerrectorado Académico/Cancillería)
ESCUELA DE CIENCIAS QUÍMICAS E INGENIERÍA
CARRERA DE QUÍMICA
ACTA DE DEFENSA No. UITEY-CHE-2022-00018-AD

A los 20 días del mes de enero de 2022, a las 12:00 horas, de manera virtual mediante videoconferencia, y ante el Tribunal Calificador, integrado por los docentes:

Presidente Tribunal de Defensa	Dra. HIDALGO BONILLA, SANDRA PATRICIA , Ph.D.
Miembro No Tutor	Dr. NAVAS CÁRDENAS, CARLOS ANDRÉS , Ph.D.
Tutor	Dr. SOMMER MARQUEZ, ALICIA ESTELA , Ph.D.

El(la) señor(ita) estudiante **MONTESDEOCA ARREDONDO, KIMBERLY FERNANDA**, con cédula de identidad No. **1004332480**, de la **ESCUELA DE CIENCIAS QUÍMICAS E INGENIERÍA**, de la Carrera de **QUÍMICA**, aprobada por el Consejo de Educación Superior (CES), mediante Resolución **RPC-SO-39-No.456-2014**, realiza a través de videoconferencia, la sustentación de su trabajo de titulación denominado: **Using mining industry wastewater to obtain Prussian blue analogues-silica monolith hybrids: a key to reduce water pollution**, previa a la obtención del título de **QUÍMICO/A**.

El citado trabajo de titulación, fue debidamente aprobado por el(los) docente(s):

Tutor	Dr. SOMMER MARQUEZ, ALICIA ESTELA , Ph.D.

Y recibió las observaciones de los otros miembros del Tribunal Calificador, las mismas que han sido incorporadas por el(la) estudiante.

Previamente cumplidos los requisitos legales y reglamentarios, el trabajo de titulación fue sustentado por el(la) estudiante y examinado por los miembros del Tribunal Calificador. Escuchada la sustentación del trabajo de titulación a través de videoconferencia, que integró la exposición de el(la) estudiante sobre el contenido de la misma y las preguntas formuladas por los miembros del Tribunal, se califica la sustentación del trabajo de titulación con las siguientes calificaciones:

Tipo	Docente	Calificación
Tutor	Dr. SOMMER MARQUEZ, ALICIA ESTELA , Ph.D.	10,0
Miembro Tribunal De Defensa	Dr. NAVAS CÁRDENAS, CARLOS ANDRÉS , Ph.D.	10,0
Presidente Tribunal De Defensa	Dra. HIDALGO BONILLA, SANDRA PATRICIA , Ph.D.	10,0

Lo que da un promedio de: **10 (Diez punto Cero)**, sobre 10 (diez), equivalente a: **APROBADO**

Para constancia de lo actuado, firman los miembros del Tribunal Calificador, el/la estudiante y el/la secretario ad-hoc.

Certifico que *en cumplimiento del Decreto Ejecutivo 1017 de 16 de marzo de 2020, la defensa de trabajo de titulación (o examen de grado modalidad teórico práctica) se realizó vía virtual, por lo que las firmas de los miembros del Tribunal de Defensa de Grado, constan en forma digital.*

MONTESDEOCA ARREDONDO, KIMBERLY FERNANDA
Estudiante

Dra. HIDALGO BONILLA, SANDRA PATRICIA , Ph.D.
Presidente Tribunal de Defensa

SANDRA PATRICIA HIDALGO BONILLA
Firmado digitalmente por SANDRA PATRICIA HIDALGO BONILLA
Fecha: 2022.01.22 07:58:14 -05'00'

Dr. SOMMER MARQUEZ, ALICIA ESTELA , Ph.D.
Tutor

ALICIA ESTELA SOMMER MARQUEZ
Firmado digitalmente por ALICIA ESTELA SOMMER MARQUEZ
Fecha: 2022.01.21 13:43:31 -05'00'

Dr. NAVAS CÁRDENAS, CARLOS ANDRÉS , Ph.D.
Miembro No Tutor

YEPEZ MERLO, MARIELA SOLEDAD
Secretario Ad-hoc

AUTORÍA

Yo, **KIMBERLY FERNANDA MONTESDEOCA ARREDONDO**, con cédula de identidad 1004332480 declaro que las ideas, juicios, valoraciones, interpretaciones, consultas bibliográficas, definiciones y conceptualizaciones expuestas en el presente trabajo; así cómo, los procedimientos y herramientas utilizadas en la investigación, son de absoluta responsabilidad de el/la autor(a) del trabajo de integración curricular. Así mismo, me acojo a los reglamentos internos de la Universidad de Investigación de Tecnología Experimental Yachay.

Urcuquí, enero 2021

_____

Kimberly Fernanda Montesdeoca Arredondo

C.I.:1004332480

AUTORIZACIÓN DE PUBLICACIÓN

Yo, **KIMBERLY FERNANDA MONTESDEOCA ARREDONDO**, con cédula de identidad 1004332480, cedo a la Universidad de Investigación de Tecnología Experimental Yachay, los derechos de publicación de la presente obra, sin que deba haber un reconocimiento económico por este concepto. Declaro además que el texto del presente trabajo de titulación no podrá ser cedido a ninguna empresa editorial para su publicación u otros fines, sin contar previamente con la autorización escrita de la Universidad.

Asimismo, autorizo a la Universidad que realice la digitalización y publicación de este trabajo de integración curricular en el repositorio virtual, de conformidad a lo dispuesto en el Art. 144 de la Ley Orgánica de Educación Superior.

Urcuquí, enero 2021.

_____

Kimberly Fernanda Montesdeoca Arredondo

C.I.:1004332480

Dedication

To my parents,

nothing would be the same without you.

Kimberly Montesdeoca Arredondo

Acknowledgment

Resumen

Se sintetizaron materiales con porosidad jerárquizada y funcionalizados con diferentes metales como cobre (II), zinc (II), hierro (II) y hierro (III) para obtener monolitos de sílice para el tratamiento de aguas residuales de extracción minera. Los monolitos de sílice se sintetizaron utilizando el método de emulsión con alto contenido de fase interna (HIPE) por sus siglas en inglés. Posteriormente los monolitos funcionalizados fueron impregnados con ferrocianuro de potasio o con agua residual de extracción minera emulada en el laboratorio, para precipitar *in situ* análogos de azul de Prusia y reducir el contenido de cianuros en el agua.

La impregnación con ferrocianuro se realizó por contacto bajo condiciones controladas, mientras que la impregnación con aguas residuales se realizó por flujo laminar no continuo. Posteriormente se determinó la cantidad de cianuro (CN^{-1}) adsorbida, de forma que se exploró la posible formación de análogos de azul de Prusia (AAP) en el interior del monolito, con el fin de obtener materiales que puedan ser utilizados para el almacenamiento de energía (baterías monovalentes o almacenamiento de H_2). Esta posible formación se determinó mediante la caracterización de las muestras durante las fases de funcionalización e impregnación mediante XRD, ATR-FTIR, DRS-UV-Vis, medidas de susceptibilidad magnética y SEM-EDX. Para la fase de funcionalización, se obtuvo información de las técnicas ATR-FTIR, EDX y DRS-UV-Vis, mostrando que los metales estaban presentes en forma de óxidos. Para la fase de impregnación con ferrocianuro, los AAP's se formaron en la estructura de monolito, lo que fue confirmado por ATR-FTIR, DRS-UV-Vis XRD, mediciones de susceptibilidad magnética, y SEM-EDX. Para la fase de impregnación con agua emulada en flujo laminar utilizando los monolitos como micro-reactores, se formaron complejos que no son necesariamente AAP y se observó que la concentración de CN disminuyó al menos un 30% de su concentración inicial. Este trabajo presenta una forma potencial e interesante de utilizar las aguas residuales para mitigar la contaminación por CN y metales pesados y, a su vez, fabricar materiales que podrían utilizarse en el almacenamiento de energía.

Palabras clave: Cianuro, monolitos de sílice, extracción minera, AAP, mitigación, porosidad jerarquizada.

Abstract

Materials with hierarchical porosity and functionalized with different metals such as copper (II), zinc (II), iron (II) and iron (III) were synthesized to obtain silica monoliths for the treatment of wastewater from mining extraction. Silica monoliths were synthesized using the high internal phase emulsion method (HIPE). After functionalizing the structure with the metals they were subsequently impregnated with Ferrocyanide or synthetic wastewater from mining extraction, to in situ precipitate Prussian blue analogues (PBA's) and to reduce the cyanides content in the water.

Ferrocyanide impregnation was performed by contact under controlled conditions, while impregnation with wastewater was performed by non-continuous laminar flow. The amount of adsorbed CN was then determined as well as the possible formation of Prussian Blue Analogues (PBA's) inside the monolith in order to obtain materials to be possible used for storage energy (batteries or H_2 storage). This possible formation was determined by the characterization of the samples during the functionalization and impregnation phases by XRD, ATR-FTIR, DRS-UV-Vis, magnetic susceptibility measurements, and SEM-EDX. For the functionalization phase, information was obtained from ATRFTIR, EDX and DRS-UV-Vis techniques showing that metals were present in the form of oxides. For the ferricyanide contact impregnation phase the PBAs were formed in the monolith structure, which was confirmed by ATRFTIR, DRS-UV-Vis XRD, Magnetic susceptibility measurements, and SEM-EDX. For the impregnation phase with synthetic water in laminar flow using the monoliths as microreactors, complexes were formed that are not necessarily PBA and it was observed that the CN concentration decreased at least 30% of initial concentration. This work presents a potential and interesting way to use wastewater to mitigate CN and heavy metal contamination and in turn to manufacture materials that could be used in energy storage.

Keywords: Cyanide, silica monoliths, mining, PBA, mitigation, hierarchical porosity.

Content index

List of Figures

List of Tables

Chapter 1

Background

1 INTRODUCTION TO CYANIDES AND CYANIDES COMPOUNDS

Cyanide group (C≡N) is constituted by one atom of carbon (C) and one atom of nitrogen (N) and it has a negative charge equivalent to -1; both are linked by a triple covalent bond [1]. Also, cyanide has strong ability to attract metals, it is a weak acid, it is soluble in water and, it has a characteristic smell of bitter almonds [1–3].Cyanide and transition metals form stable complex compounds. Most are soluble in water for example Prussian blue [1].

Properties of cyano compounds can be change depending on the type of bonding formed and on the atom that the cyanide group can be linked [4]. Cyanide can also form polymeric chains, or crystalline networks, since it can be bonded at either of its two constituent ends [4].There are three forms of cyanides: a) free cyanides, b) weak acid dissociable (WAD) cyanides and c) total cyanides [2]. These are shown in Table 1. Also, it is possible to classify them into organic and inorganic compounds [3].

Table 1 General classification of cyanide compounds [2].

Cyanide classification	Examples
Free cyanides	CN^-
WAD cyanide	Weak and moderately strong metal-cyaide complexes (Ex: Ag, Cd, Cu,, Hg, Ni, Zn).
Total cyanide	Strong metal-cyanide complexes (Au, Co, Fe, Cu).

1.1 Cyano organic compounds

Organic cyanides are usually called nitriles, and they form covalent bonds. Nitriles are versatile synthetic intermediates in organic synthesis [5]. Moreover, organic cyano compounds are colorless, with the smell of bitter almonds, very volatile, and they behave like nucleophiles in conjugate additions reactions [5–7].

These compounds are distributed in three categories based on aminoacids content. They are α and β unsaturated nitriles, alkanitriles and aromatic nitriles [8]. Besides these compounds are found in a wide range of natural products extracts. For example, marine sources are the broadest source of nitriles with medicinal activity. There are more than 120 natural nitriles from terrestrial and marine sources reported.

Also, some of the cyano compounds that one can find in this category are of the thiocyanate type. Thiocyanates are anions that have an oxygen or sulfur atom added to the cyano group, this is attached to carbon through a covalent bond and as a functional group the negative charge equal to -1 is maintained. [9].

1.2   Cyano inorganic compounds

Inorganic cyano compounds are divided into three groups: salts, complex compounds, and hydrogen cyanide.

1.2.1   Salts

The cyano functional group is capable of forming ionic bonds with alkali metals and fluorin [4]. These compounds have melting points ranginge between 550°C to 650°C and they are soluble in water. Cyanide salts dissociate easily at neutral pH, have a low melting point and a high boiling point. At ordinary temperatures, sodium cyanide (NaCN), potassium cyanide (KCN), and rubidium cyanide (RbCN) crystallize with the halite structure (Figure 1a) a face-centered cubic packing, where the cations are located in the octahedral holes. While cesium cyanide (CsCN) and thallium cyanide (TaCN) crystallize with the cesium chloride structure (Figure 1b) [10,11].
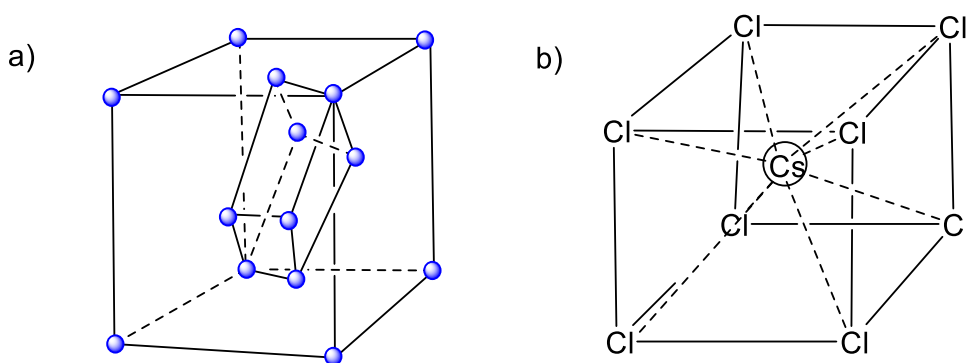
Figure 1 Schematic representation of crystalline structures: a) Halite, b) Cesium Chloride structure. Adapted from Huheey, Keiter and Keiter, 1993. [11]

1.2.2   Cyano complex compounds

In inorganic cyano complexes the cyano functional group acts as monodentate ligand with the central metal binds to the carbon of the ligand. However, these compounds are characterized by their ability to behave as bidentate ligand, this is possible when the metal center also binds with nitrogen. In other words, these compounds are polynuclear complexes [4,12]. These cyano complex are formed from a polymerization of the compound between the covalent bonds of central metal and carbon of the group.

The stability and nature of the complexes is given by the pH of the medium and by its coordination number. There are two types of geometries for cyanide complexes: octahedral and tetragonal geometry (Figure 2). Octahedral complexes could be represented with the general formula $[M^{m+}(CN)_6]^{m-6}*nH_2O$, where M corresponds to the transition metal with d orbitals. While for the tetragonal structure the general formula is $[M^{m+}(CN)_4]^{m-4}*nH_2O$ [4].
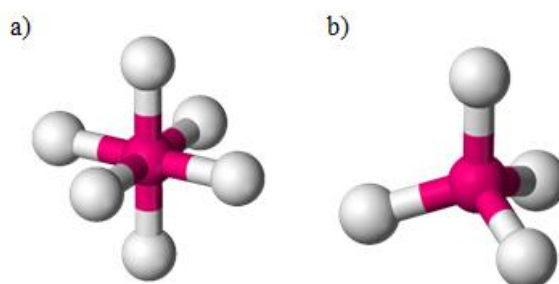
Figure 2 Geometrical structure, a) octahedral, b) tetrahedral. Adapted from Huheey, Keiter and Keiter, 1993.[13]

Also, there are compounds that contain the thiocyanate group (Figure 3) like a monodentate ligand, this ion has greater polarization and forms stable complexes with cations with greater ionic radius. In other words, it forms stable complexes, although the polarization effect of the cations is less.
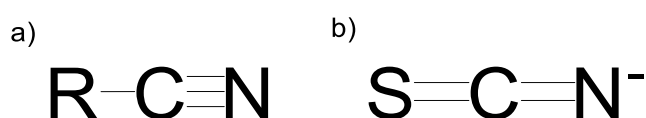
Figure 3 Functional groups:

a) cyanide and b) thiocyanate anion. Adapted from Klein, 2017. [14]

The most used cyano complex is Prussian Blue (PB). Since 1970s this compound was used for painting, printing and dyeing industries. Since its discovery, technological development has been a key element for the field of application of PB to expand [12]. Currently, one of the areas of interest for scientists is the study of the properties of PB and its analogues (PBA) for energy storage.

1.3   Toxicity of cyanide compounds

Cyanide is a toxic chemical species, regardless of whether its origin is natural or synthetic [1]. It can cause damage to living beings since this compound directly affects the nervous system, and the limit of cyanide consumption for humans is 50 mg to 200 mg [15].

In the organisms cyanide inhibits the cytochrome c oxidase complex, which blocks the electron transport chain, immediately affecting the cellular respiration process [15]. As a consequence, an over stimulation of biological processes is generated. For living beings, the organism has a biological process that convert the cyano compounds to be assimilated by the conversion into thiocyanate [7,9,16]. In other words, when these ions enter the organism of living beings, they immediately interrupt the process of cellular respiration. CN blocks the mitochondrial respiration chain and the formation of intracellular adenosine triphosphate [17–19].

Mining companies and metallurgical industries release wastewater with high concentrations of cyanide compounds. The main reason for its toxicity is because CN's ability to bind iron ions is similar to CO [20,21]. From there, the cyanide group it can find in three important forms: free cyanide, Weak Acid Dissociable (WAD) cyanide, and total cyanides [1,2].

Free cyanides are the most reactive species of the group because in small periods of time they can react with other chemical substance, and they can produce new compounds [9]. The problem is the uncertainty in the toxicity of the new compounds because they can be more or less toxic than cyanide [22]. However, there are some mechanisms and technologies for environmental remediation treatments [1,2].

2 METHODS FOR OBTAINING CYANIDES

Cyanide compounds can be found in environment, biological materials, and industrial processes [3]. That is, cyanide compounds have two sources of origin: natural and non-natural.

2.1 Natural sources

Cyanides are produced by living beings because it is present in some animals and plants. The natural sources of cyanide encompass a wide range of life forms, the most representative of which are: photosynthetic bacteria, algae, fungi, plants, and food [23]. These cyanide compounds are not lethal to their producers because they are produced in small quantities and many microbial species degrade them into ammonia and carbonate during the metabolism process [22].

Natural products comprise the main source of naturally occurring cyanides. Cyanide can be obtained from cyanogenic glycosides. These are a class of secondary plant metabolites, which constitute the chemical defense systems of plants and insects. The compound obtained from natural product extractions is amygdalin. It consists of a disaccharide molecule where the cyano group is attached to a CH in the chemical structure (Figure 4) and is produced by a hydrolysis process.
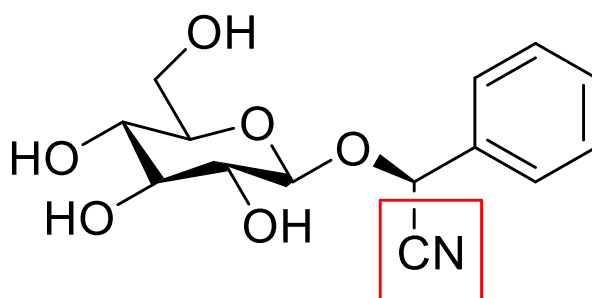
Figure 4 Representation of amigdaline structure.

Adapted from Qadir and Fatima, 2017. [24].

Table 2 shows the most important seeds that contain cyanogens in their structure. It can be seen that the cyanide content varies within the same species, for example, in the case of plum, in spite of being the same species, green plum has the highest cyanide content. For this reason, the processes and nutritional content of the crop can cause the cyanide content of the seeds to vary [25]. For example, in the case of cassava, the cyanide content changes according to: the type of cassava, the time in which the crop was grown, the amount of protein it contains, and the extraction process carried out [26].

Table 2 Content of cyanide in different kinds of seeds

Seeds	Quantity of cyanide (CN^{-1})	Ref.
Apple	2.80±0.02 mg/kg	27
	1-3.9 mg/g	23
	108 mg/100g	28
Flax	7.3 mg/100g	28
Apricot	1.88±0.07 mg/kg	27
	14.3±0.28 mg/g	23
Peach	710 ppm	29
	196 ppm	29
	696 ppm	29
Bean	1.76-1.77 mg/kg	3
Millet	2.11-2.14 mg/kg	3
Almond	7.4 mg/100g	28
Plum	247 mg/100g	28
Green Plum	17.5 mg/g	23
Black Plum	10 mg/g	23
Red cherry	3.9 mg/g	23
Black cherry	2.7 mg/g	23
Cassava	2 mg/g	26

As shown in Table 2 several of these products are commercially consumed. However, to avoid poisoning by their consumption, procedures such as peeling, crushing, shredding, grating, soaking, fermenting and drying are used [25]. There are also processes for the loss of hydrogen cyanide (HCN) to the atmosphere by the action of microbial enzymes or plant enzymes [23]. For this reason, the cyanides of natural sources in small quantities are not lethal for living beings, and they do not cause damage at the ecosystem level.

2.2 Non-natural sources

Cyanide production from non-natural sources is directly linked to anthropogenic activities. The production of HCN, NaCN, and KCN are the most representative forms of

these activities. Furthermore, the most significant quantities of cyanide compounds are obtained in the industrial sector as a by product of the processes. Examples are coal gasification and coking, steelmaking, and petroleum refining [19]. The primary ways to synthesis cyano compounds are: cyanide substitution, oxidative addition, indirect synthesis of the cyanide ligand or by electrochemical reactions [12].

Some of the industries where cyanide is used are in the metal finishing, mineral extraction and hydrometallurgy industries, in the plastic production of all kinds of dyes, and laboratory chemical products [1,30]. Additionally, cyanides can be released into the environment because of tobacco smoke, industrial fires, sewage, and as industrial waste. The environment can be affected by the release of cyanide compounds, being a pollution problem. Therefore, these compounds can adversely affect living beings and the ecosystems. The toxicity of cyanide largely depends on the form in which it is found (salts, complexes, free ions). The most toxic form of cyanide is a free ion because it is easier for organisms to absorb [31].

So, the contributions of non-natural sources of cyanide to the environment are greater in quantity than the natural contributions [19]. Therefore, the impact that cyanide compounds have on the environment and living beings, the need was born to find methods of quantification and determination of cyanide in the different elements that make up the biosphere, (atmosphere, water, soil) and in products. consumption, (food, beverages, topical products, medications, etc).

3 METHODS OF QUANTIFICATION AND DETERMINATION OF CYANIDES

Because of the high toxicity of cyanide and the poor environmental control by the authorities, several entities worldwide have established a limit for cyanide concentration in freshwater bodies of 0.2 mg/L [1,2,22,32]. From this, various methods of qualification and quantification of cyanide ions have been developed. These methods can be divided in colorimetric, and non-colorimetric methods. Some fields in which they are used are: water and soil treatment, pharmacology, agronomy, food industry, among others [33].

This section shows the most used methods for the determination of cyanides in water bodies, taking into account the analytical classification of Anning *et al* 2019 [1].

3.1 Colorimetric methods

Colorimetric methods are qualitative tests that allow the identification of a reagent by the color change that is experienced in the presence of an analyte [34]. In the case of cyanide, these tests are viable because this is a powerful ligand for many metal ions. By this way the colors of the complexes function as indicators [27]. This type of test is sensitive to high concentrations greater than 10 mg/mL [17,32,35,36].

However, in this type of method there may be interference due to the presence of sulfides, thiocyanates, thiosulfates, and some specific metals [34]. The most used colorimetric methods are: Magnin assay, Aldridge method based on the König synthesis, and Weehuizen method.

3.1.1 Magnin assay

This method is based on the formation of a Prussian Blue [17]. It is a dark blue precipitate. The test occurs by an alkalinization phenomenon, when iron II sulfate is added to an acid sample. (Bark and Higson 1963; Greene, Robert, and Breazeale 1937). One of the applications of this method is to detect cyanides and ferrocyanides in wines [32].

3.1.2 Aldridge method based on the König synthesis

This method consists of reacting the cyanide with an excess of bromine, and allowing it to react with a pyridine-benzidine reagent [34]. As a result, the deep orange solution will turn red. Excess of bromine in the test can be removed with arsenic acid[32]. This method is usually applied in commercial effluents as it is recommended by the Joint Committee of the Association of British Chemical Manufacturers and the Society for Analytical Chemistry [32].

3.1.3 De Von Liebig reaction

This method is carried out by a sulphocyanide reaction, where an intense red complex is obtained [17]. The reaction takes place when a solution with cyanide ions reacts with a polysulfide to form a sulfocyanide [17,33] . Finally, the red complex $[Fe(SCN)_2]$ is formed when an acid pH is stabilized and ferric chloride ($FeCl_3$) is added [17].

3.1.4 Weehuizen method

This method is carried out by the oxidation of phenolphthalein by cyanogen, which is released when copper (Cu) reacts with CN⁻ ions [32]. This test requires a copper solution and a phenolphthalein solution to react with the cyanide-containing sample [27,35]. This method can give false positives because the potassium ferrocyanide inhibits the effect of the pink color of phenolphthalein, so there is no reaction [35].

There are more colorimetric tests that can be grouped into complex formation with specific metals [32]. However, these are usually combined with spectroscopic techniques, because some complexes are unstable or the test does not have low sensitivity[36–38].

In general, it is important to mention that these colorimetric methods are unreliable for determining cyanide in small quantities.

3.2 Non-Colorimetric methods

Non-colorimetric methods for determination of cyanides in water involve gravimetric methods to determine the end point by instrumental endpoint detection and visual end-point indicators, voltammetry methods and chromatographic methods [32].

In addition, gravimetric methods allow quantification through stoichiometric reactions or calibration curves [39]. In both cases, the determination is possible through the transformation of the reagents into insoluble products of high purity[39]. Besides, voltammetry corresponds to an electroanalytical method, where information about the analyte is obtained by the change in current when the potential is modified [39]. While chromatographic methods correspond to a physical separation method, in which the components are distributed in two phases. A stationary phase and a mobile phase [39].

3.2.1 Gravimetric methods with visual endpoint indicator

The Liebig's method uses a visual end-point indicator which determines cyanides ions with silver ions [40]. The titration is based on the formation of silver cyanide (AgCN) by a substitution reaction between silver nitrate (AgNO₃) and a solution containing cyanide ions, as shown in reaction (1) [17].

$$2CN^- + AgNO_3 \rightarrow Ag(CN)_2 + NO_3^- \qquad (1)$$
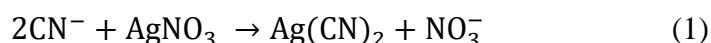
This method allows the quantification of free cyanide, zinc and copper cyanides with a sensitivity of 1 mg/L [1]. It is important to mention that Liebig's method is the most representative of this work. However, there are other methods that involve modifications

and extensions of the Liebig's method that include the formation of specific complexes for the determination of cyanides [40–42]. These methods have a small range of application, because they need complementary procedures such as ion exchange chromatography, fluorimetry and liquid chromatography.

3.2.2   Gravimetric methods with instrumental end point detection

The gravimetric method with instrumental method is a potentiometric titration that can be expressed as the combination of the gravimetric method with a visual endpoint indicator using a potentiometer [32]. It can be consider as an extension of the Liebig's method [40]. This electrochemical method allows the identification of the titration endpoint at a lower limit than using the indicator [43]. This is an amperometric titration method with silver nitrate and has the same accuracy-precision as Liebig's visual method [1].

3.2.3   Voltammetric and polarographic methods

The voltammetry method utilizes the advent of modern sensitive waveforms such as differential pulse polarography for the determination of cyanide at concentrations down to 1.5 μg/L [34]. For this reason, the use of this method is recommended for the determination of cyanide at low concentrations. The procedure is remarked that ionic cyanide depolarizes the mercury electrode to produce an anodic wave [1,44].

3.2.4   Chromatographic methods

This method is widely used for analysis of biological samples. These methods are often complemented with other types of detectors to increase sensitivity [45]. For example, mass spectrometry detectors, the nitrogen-phosphorus detector and an electron capture detector [27]. The detection limit varies according to the technique used, however it is below 0.1 mg/L [32,46]. In addition, this method can be automated, for example gas chromatography can perform a flow-through analysis with a detection limit of 10 μg/L [34].

The application of chromatographic techniques is wide, from detection of contaminants to quality control of products for human consumption [44]. This is because detection limits can be modified and are easily coupled to spectrophotometric methods [45].

3.3 Miscellaneous methods

Several colorimetric methods can be complemented by spectroscopic techniques in order to validate the formation of the complexes and quantify the cyanide ions. For example

the Weehuizen's method with UV-Vis spectroscopy [36,44]. In addition, there are other methods that are also used such as fluorometry, chemiluminescence, atomic absorption, and near-infrared cavity ring down spectroscopy [27,46,47].

The method chosen depends on the group of cyanides to be analyzed and the parameters for each of the tests such as detection limit, precision, interferences, medium and reproducibility.

4 HCN SPECIAL CASE

Hydrogen cyanide (HCN) is colorless weak conjugated acid, which has a characteristic aroma of bitter almond [1,48]. The origin of the $HCN_{(aq)}$ is by the direct reaction of alkanes with ammonia, or as a by-product of the manufacture of acrylonitrile. It is an unstable tautomer of hydrogen isocyanide [31]. Its boiling point is 25.70 °C while the melting point is -13.24 °C [49]. Hydrogen cyanide is soluble in ether and it dissociates completely in water and alcohol [48]. Equation (2) describes how cyanide anionis released when hydrolyzing [1]. HCN can be found in aqueous $HCN_{(aq)}$ or gaseous $HCN_{(g)}$ state [33].

$$HCN_{(aq)} + H_2O_{(l)} \rightarrow CN^-_{(aq)} + H_3O^+_{(aq)} \qquad (2)$$
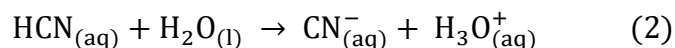
As mentioned above, the cyanide compounds present in water can be classified as follows (a) free cyanide, (b) Weak Acid Dissociable (WAD) cyanide, and (c) total cyanides [1,2]. These aqueous cyanide compounds exist as cyanides, cyanates and simple and complex nitriles [1]. Its salts are strong oxidants, incompatible with nitrates, chlorates and acids [23]. This is one of the most representative compounds of the cyano group, both in abundance and applications.

$HCN_{(aq)}$ is one of the most representative compounds that contain the cyano functional group because it is very abundant in the solar system. It can also be found as poly-HCN in a solid state, this is brown or dark in color and does not have a characteristic odor. Poly-HCN is easily formed on the surfaces of celestial bodies, since the dark color that covers them is attributed to this polymer [50].

HCN is easily produced over a variety of reducing atmospheres, high temperatures, ionizing radiation, or the action of electrical discharges. Also in the laboratory, $HCN_{(g)}$ can be prepared by two common ways. In first way, HCN is produced by a reaction between sulfuric acid and cyanide salt such as: sodium cyanide, potassium cyanide,

ferrocyanide. While, the second way propose a reaction between ammonia and methane with an air over a platinum catalyst at 826.85 K [50,51].

4.1 HCN associated to origin of life

The theory of the origin of life associated with HCN was put forward in 1924 by the Russian biochemist Alexandre Oparin and was later supported by the Stanley Miller experiment [52,53]. This hypothesis affirms that life was generated spontaneously thanks to the particular conditions that existed in the early stages of Earth's history [54,55]. Hydrogen cyanide (HCN) is considered a fundamental molecule in prebiotic chemistry experiments because it had an important role as a raw material to form more complex molecules essential for life [54].

Furthermore, this compound could be an intermediate molecule in chemical reactions such as: oligomerization reactions of CN^-, redox reactions to produce urea and carboxylic acids, formation of HCN – Derived Thermal Polymer (HCN-DTP), condensations of lactate and malonate, formation of nucleobases and nucleotides, and Strecker condensation to produce amino acids [7,8,54,55].

The Urey-Miller experiments sought to replicate the chemical processes that were carried out for the formation of HCN in the reducing atmosphere of Hadean Earth [52,53]. This was composed of ammonia, hydrogen and water that would later collaborate with the polymerization of HCN (Barajas et al, 2020). These experiments showed that hydrogen cyanide is an important precursor for the formation of organic molecules essential for life, such as: derivatives of carboxylic acids, amino acids, purines, pyrimidines and other carbonyl compounds [52].

4.2 HCN polymerzation

HCN polymerizes easily when it is not stabilized or is not completely pure [1]. Liquid ($HCN_{(aq)}$) has a tendency to polymerize at room temperature in the presence of a base. The spontaneous process results in a dark brown solid [56]. HCN polymers can be synthesized from pure HCN, cyanide salts, or from HCN oligomers, trimers and tetramers, consequently, HCN-poly comprises a large number of complex organic substances [56]. Some examples are in Figure 5.
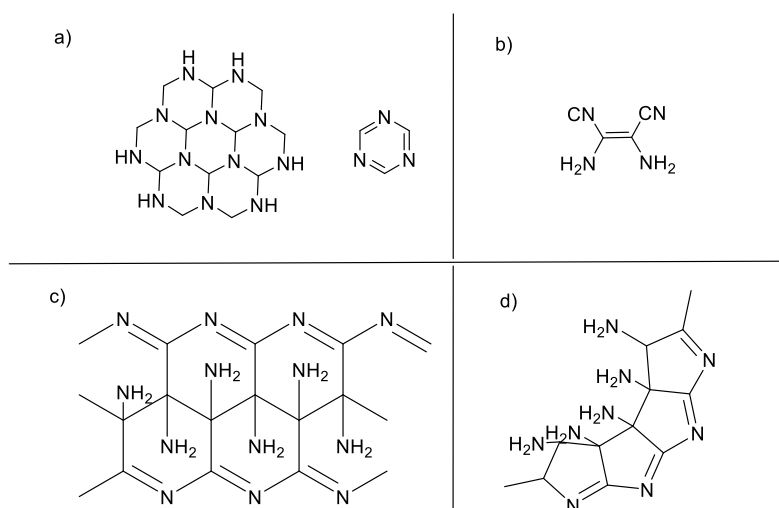
Figure 5 Structures of HCN-polymer: a) addition polymer fragment structure, b) Diaminomaleonitrile (DAMN), c) Volker structure, d) Umemoto structure. Adapted from Matthews, 2004 [57].

HCN-poly is easily formed when HCN is irradiated by charged particles [50]. In 1960 the ladder structure was proposed for this polymer made up of HCN dimer repeats [50,56]. It can be divided into three forms: true polymeric $(HCN)_n$, HCN heteropolymer (non-polymer), polymer in aqueous solution [50]. The applications of HCN-poly are still under investigation due to its solubility properties, since they do not allow the correct characterization of this polymer [56]. However, this polymer promises great contributions in the area of evolutionary chemistry and materials and surface sciences.

Some examples of these applications are biomedical devices, development of multifunctional materials with properties of semiconductivity, ferroelectricity, catalysis, photocatalysis and heterogeneous organosynthesis [56]. In addition, HCN-poly is key in the reconstruction of the first protometabolic systems, which to understand cell life as a function of probiotic chemistry theory [52].

According to the previous information one can see that starting from $HCN_{(aq)}$ it is possible to obtain many different compounds among them the prussian blue and Prussian blue analogues which are a very promising polymer compounds or complex compounds for energy storage among other very interesting applications already mentioned. A deeper study about these compounds will be treated in next section.

4.3 Compounds obtained from HCN

From the compound $HCN_{(aq)}$ several types of compounds can be formed that are important in different fields of science and industry. Among these compounds is the formation of cyanohydrins by the addition to carbon-carbon double bonds with carbonyl groups of aldehydes or ketones [49].Also, cyanuric chloride is an essential reagent for the chemistry of s-triazines, it is formed when HCN is mixed with chloride [49,55]. In addition, the acid can form carbides and nitrides when reacted with metals at temperatures above 873.15 K [29,49,56].

In polymerization processes, HCN carries out an autocatalytic polymerization reaction to form the cyano compounds essential in prebiotic synthesis, iminoacetonitrile and diaminomaleonitrile [7,49,55]. For example, HCN forms azulmic derivatives in the presence of alkali. Besides, HCN can be hydrolyzed for giving formic acid or ammonia [49].

Metal cyanides are another type of compound that can be formed from HCN. These are compounds with a metal center that is attached to cyanide ions as ligands. They are represented by the formula $M(CN)_y$ where n depends on the oxidation state of the metal and M is a metal [4,49]. From these compounds appear the cyanide complexes that are described by the formula $A_x[M(CN)_y]$, where A is an alkali metal and M is a transition metal. These cyano compounds tend to be very stable, however their dissociation is highly dependent on pH, concentration and valence of the metal center [10,49,58].

4.3.1   Prussian Blue (PB)

Prussian blue (PB) is an inorganic complex compound. It constituted by an iron liked to six cyanide groups that acts like ligands of the coordination sphere $Fe^{III}[Fe^{III}(CN)_6]$ is insoluble in water. PB has electrochromism, this is a property that some compounds have to change color reversibly when an electrical charge is applied [59]. So, it presents magnetism at low temperatures, and semiconductor behavior [59].

The color of Prussian blue pigments results from an intervalence electron transfer absorption band at 700 nm that corresponds to the transfer of an electron from an iron (II) to an iron (III) ion when light is absorbed [59]. The composition of Prussian blue consists of bonds of the Fe (II) -CN-Fe (III) type. One is Fe (II) -C distances of 1.92 Å and other is Fe (III) -N distances of 2.03 Å. The Fe (II) centers, which have a low spin, are

surrounded by six carbon ligands. The Fe (III) centers, which have on the contrary a high spin, are surrounded on average by 4 nitrogen centers and by 1.5 oxygen centers [4,12].

PB has a wide range of application in applied and research fields. Since its discovery the main application of this compound has been as a paint pigment because it is recognized like the first synthetic pigment [10]. It is also used as a drug to counteract the effects of cesium radioactivity [60]. In recent years, its magnetic and optical properties have been investigated for the development of energy storage, semiconductors, sensors for nonelectroactive cations, biosensors and as an advanced transducer for hydrogen peroxide [61–64].

4.3.2   Prussian blue analogues (PBA)

Prussian Blue Analogs (PBA) are microporous inorganic solids [65]. They have an octahedral coordination sphere of [Fe(CN)$_6$] coordinated to 3d transition metals, with a general formula $A_xM[Fe(CN)_6]$, where M represents transition cations coordinated to nitrogen and A represents interstitial sites forming cavities of approximately 8 Å in diameter [65]. Prussian blue analogs have a face-centered cubic crystal system (fcc) [64]. They have the ability to store gases, conduct and immobilize metal ions. In addition, because they present structural vacancies, they can transport mass in a reversible way (Simonov et al. 2020). Figure 6 shows the unit cell for the PBA [62].
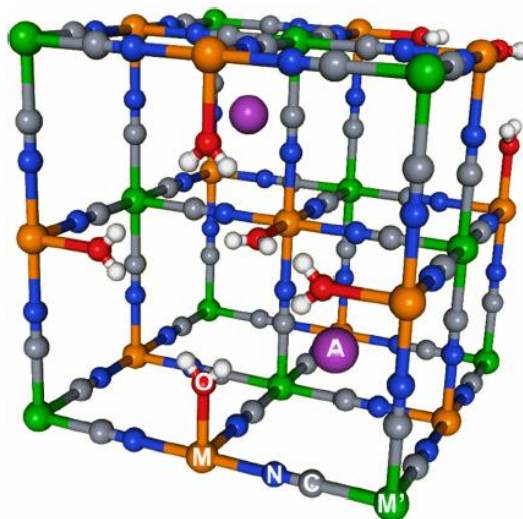
Figure 6 Schematic representation of unit cell of prussian blue analogues, where orange M is transition metal, green M' is metallic center of the complex, purple A is a element for vacancy, and other ballons represent the elements present: blue-nitrogen, white-hydrogen, grey-carbon and red-oxygen. Adapted from Lejeune *et al,* 2014 [62].

From the stability constants, the compounds can be classified as very strong or weak complexes.

For this work, the strongest complex is the iron complex (logK: 52), followed by the copper complex (LogK: 27.3) and the zinc complex (LogK: 16.9), the latter being considered a weak complex. [58]. The synthesis of PBA's is carried out with the mixture of Fe(III) or Fe(II) ions with hexacyanoferrate with different oxidation state than the Fe ions to be used. Some PBAs do not precipitate directly but form colloidal suspensions [49,65].

4.3.3 Properties of PB and PBA

PB and PBAs are mainly used in research in the fields of energy storage and conversion by studying and optimizing the properties of these compounds. PBA's present three-dimensional networks with large spaces to host large alkali ions, such as Li^+, Na^+ and K^+ [66]. The structure of PBA's is defined by the Fe-C and Metal-N bonds that make up the crystal lattice structure of the analog. Three polymorphisms can be found: monoclinic, cubic and rhombohedral [62,65].

The structure depends on the amount of alkali ions present in the structure, where x is their concentration. They are: a) x < 1 Cubic; b) x = 1.72 Monoclinic; c) 1 < x < 1.72 Cubic and monoclinic. Also through refinements to the crystal structures mentioned above one can arrive at the rhombohedral structure [65,67]. In the unit cell, the alkaline metal is placed into the lattice cavities of unit cell to balance charge with $M[CN_y]$ ions and water molecules are placed in the defective sites of the lattice [61,68].

Prussian blue is paramagnetic at room temperature, this phenomenon is attributed to the presence of low spin Fe(III) in the chemical structure (S=1/2) [64,67]. However, the ferromagnetic behavior of PB and PBA's depends on the Curie temperature at which their properties are being analyzed [10]. In the crystal lattice of PBA's it is expected to have low spin/high spin combinations for metals. Changes in the electronic configuration change the color of the complexes by a shift in the electromagnetic spectrum [10,63,64]. Table 3 shows some values of the mass susceptibility for such complexes. These data are related to the paramagnetic character in the temperature range 84-294 K [69].

Table 3 Magnetic susceptibility data for some complex compounds [69]**.**

Complex compound	$X_M(*10^{-3})$
$Cu_2[Fe(CN)_6]*14H_2O$	1.9/Cu
$Co_3[Fe(CN)_6]_2*14H_2O$	23.5/Co
$Fe_4[Fe(CN)_6]_3*14H_2O$	13.9/Fe
$Co_2[Fe(CN)_6]*9H_2O$	9.2/Co

4.3.3.1 Uses of PB and PBA

Some of the applications of blue analogues are the storage energy is the most researched application of Prussian Blue Analogues. PB/PBA can be used to derive various metallic nanostructures for electrochemical applications.

The most relevant uses for PBA research are in the fields of monovalent metal ion batteries such as: cathodes and anodes in Li-ion batteries, Na, K, Mg, Ca, Al and Zn-ion batteries, for storage energy, supercapacitors, electrochemical catalysis, and conversion energy [65,67,68,70]. These applications are influenced by the ionic radius, the ionic charge, the crystal lattice, the characteristics of the metal centers, among others. Besides, it has been identified that vacancies in the crystal structures of PBA's have an effect on energy storage [65,67,68,70]. Then, Table 4 shows a brief summary of PBA's applications

Table 4 Brief summary of PBA's applications

Area	Application	Ref.
Electrochemical catalysis	Catalysts for oxygen evolution reaction (OER) is a crucial part of water splitting, CO_2 reduction and rechargeable metal-air batteries.	65 64
Hydrogen Storage	PBA composites, as a kind of microporous coordination solid with 3D-framework and high surfaces, have been considered suitable hosts capable of hydrogen storage.	70
Ion batteries	Multivalent ion batteries (Zn^{2+} / Mg^{2+} / Ca^{2+} / Ba^{2+} / Al^{3+})	68 65
Supercapacitors	The metal centers are redox-active sites for Faradaic reactions improving the charge storage capacity.	68 65

As it was previously mentioned, mining extraction generates wastes which mainly contain HCN and some heavy metals. Then next section will briefly describe some necessary concepts to understand the out coming of this thesis work.

5. WASTEWATER COMING FROM MINING EXTRACTION

Mining activity has always had a great value for human beings, however, since its beginnings it has been related to environmental problems such as water air and soil pollution. In general the mining effluents are compounded by heavy metals, radioactive metals, cyanide, and metalloids in different concentrations [1,2]. As mentioned earlier in this work, cyanide is a very toxic and harmful product for living beings and ecosystems. So, the main problem is due to extraction companies often exceed the limit for cyanide concentration in freshwater bodies of 0.2 mg/L [71]

5.1   Golden mine wastewater

Mining is an industrial activity that uses cyanide for the leaching of precious minerals such as gold and silver [1]. This activity corresponds to approximately 20% of the total cyanide production [72]. Among the main uses of global gold production one can state the following ones; about 75% is destined for jewelry, 10-15% is used for industrial applications, and about 10% is used for medicine, dentistry, and as government reserves [19].

The content of gold mining wastewater varies between heavy metals (Cu, Zn, As, Fe, Pb) and high concentrations of cyanide that are highly toxic to living beings and the ecosystem [1]. The permissible limit for cyanide in water according to the US EPA is 0.2 mg/L [1,33]. The concentration range of dilute cyanide solutions for gold leaching is between 0.01-0.05% [33]. Also, The pH range of the extraction solution is 6-10, this pH is maintained during the cyanidation process to avoid excessive loss of reagent by hydrolysis [33].

The process starts with crushing the ore and then proceeds to leaching. In this process, lime raises the pH, while cyanide and oxygen oxidize the suspended ore [1]. In addition, the cyanide solution dissolves the gold from the crushed material and precipitated gold is collected out of solution [1,19,21]. This procedure can be simplified to the following reaction (3) and it is usually called Elsner's equation [21,33].

$$4Au + 8NaCN + O_2 + 2H_2O \rightarrow 4\ Na[Au(CN)_2] + 4NaOH \qquad (3)$$
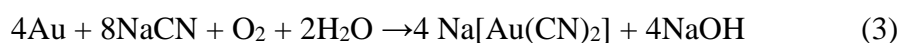
The gold extraction process aims at the formation of $Au(CN)_2$-iron complexes with a stability constant of $2x10^{38}$ [33]. From this compound gold is recovered [19]. There are some treatments to remove with cyanide such as alkaline oxidations and chlorination in order to reduce its toxicity [1]. Some environmental parameters such as pH, temperature and composition of the environment can influence the nature of cyanide reactions released in wastewater [19].

Table 5 shows the set acceptable discharge limits of total cyanides by some organizations. Also like see in Table 5 the cyanide concentration limit for fresh water is 0.200mg/L as this is the limit that is accepted by most countries. In the same way this limit is the one used in Ecuador.

Table 5 Permissible limit of cyanide residues in freshwater [1,2,30,33]

Organizations	Cyanide concentration limit in freshwater (mg/L)
World Health Organization (WHO)	0.05
United State Environmental Protection Agency (USEPA)	0.200
Indian Central Pollution Control Board (CPCB)	0.200
México	0.200

Nevertheless, several mining companies do not comply with the aforementioned wastewater cyanide limits [73]. The measurement of cyanide concentration can vary according to the area of the river where sampling is performed [18].This is because in dry seasons, in the upper part where the river carries less water the concentration of cyanides is very high, while in areas where the river flow is wider the concentration of cyanides is lower because they are more diluted [18]

5.2   Ecuador mining industry

Metal mining in Ecuador has been developed on an artisanal small-scale basis since the late 20th century [74]. Artisanal and illegal gold mining in southern Ecuador has generated a high environmental impact own to the release of highly toxic pollutants into the environment, such as cyanide compounds, heavy metals and mercury [20,74]. An example of this is the mining areas of Portovelo-Zaruma and Ponce-Enríquez where there is

evidence of decreased biodiversity and contamination of soil and water [18,75]. Some of the rivers that have been affected are: The Puyango, Siete, Gala and Chico rivers. These are part of the mining wastewater disposal system, so they have a high contaminants content [75].

In addition, according to data from the Central Bank of Ecuador, it was determined that more gold was produced annually than silver over a 10-year period from 2004 to 2014 [76]. The Au average production is approximately 5527,2 kg per year. Table 6 shows the approximate amount produced in Kg per year in Ecuador. It can be seen an increment during 2013 and 2014, possibly because of the lack of regulation in this field [76].

Table 6 Annual production of metallic minerals of the mining sector in Ecuador, period 2004-2014 [76].

	Minerals	
Period	**Au [Kg]**	**Ag [Kg]**
2005	5337,68	283,2
2006	5168,2	158,83
2007	4587,71	448,96
2008	4132,89	304,78
2009	5392,19	115,6
2010	4592,76	1168,9
2011	4923,33	1589,06
2012	5138,94	2934,24
2013	8676,42	1198,39
2014	7322,11	577,05

In 2015 the ministry of environment, water and ecological transition created a project dedicated to sustainable mining. The objective of this project was to create a mining policy with principles of sustainability and development since the mining area is a strategic sector for Ecuador [76].

Also, the Government of Ecuador seeks to promote large-scale mining in a sustainable context because mining activity has an important role in the economic and labor development of the country [73,74,77]. For this reason, the reserves are explored before exploitation and a broader analysis of the area is carried out, including the environmental and social impact. An example of this is the Sigchos project located in the Cotopaxi province, in which copper, silver and gold are mined [78]. Moreover, the mining concession

explorations increased from 3% to 13% between 2016 and 2017, these was authorized by the country's mining ministry and the analysis was focused on sustainable production [74].

In recent years, the trouble of artisanal and illegal mining has grown a lot in the country as reserves located in private areas are not fully regulated by the state, as they are considered independent from the state [18,73]. This is a problem for entities seeking to bring sustainable mining to the country. There are shortcomings in the control of compliance with mining pollution control and mitigation regulations, so the development of sustainable mining in Ecuador is still a distant reality.

As mentioned in the previous sections, there are some techniques for contaminant mitigation in wastewater. Such are: colorimetric, volumetric and chromatographic techniques. There also some strategies to mitigate the cyanide and heavy metals concentration in wastewater from mining activities [1,18]. In this context, strategies have been developed for the removal of chemical compounds involving the use of silica monoliths through the adsorption of contaminants [79].

6. HIERARCHICAL SILICA MONOLITHS FOR REMOVING POLLUTANTS

The design of the hierarchical porous materials is an important factor for the application of them. Commonly copolymer-emulsion double template is used for this purpose [41,80–82]. Hierarchical monoliths have been obtained by high internal phase emulsion (O/W) to be used in water treatment [83]. The oily phase acts as a base template, for the formation of macropores and the surfactant molecules (copolymers) ensure the formation of mesoporosity [81,84]. The porous skeleton of the material are formed by interconnection between pores, when micelles agglomerate to form larger particles, leaving holes between them [82,85]. These type of materials are promising because of the following physicochemical properties: they have thermal stability, they are optically transparent, mechanically and chemically inert [79,83].

Also, the hierarchical porosity of the materials allows a wider application for the mitigation of contaminants as it allows the encapsulation of a diverse range of organic and inorganic contaminants within the structure, as they act as molecular sieves and at the same time selective adsorption media [83,85–89]. Some examples of these applications are the use of of PBA-functionalized monoliths to adsorb radioactive cesium[83], microalgae-functionalized monoliths for the bioextraction of heavy metals[88], or the

functionalization with copper for the treatment of Total Coliforms and *E. Coli* in drinking water [89].

Chapter 2

Problem Statement

Mining is an activity that causes major environmental problems. Even though each country has legislative regulations for the control and monitoring of these activities, environmental contamination is evident. Mining activity uses approximately more than 100 thousand liters of water per kg of gold. In addition, during the extraction process, contaminants are released into freshwater bodies, most of which are heavy metals and different forms of cyanide that are lethal to living beings. This is a problem, because water is a non-renewable natural resource, and is essential for living beings. In addition, substances containing cyanide are very harmful to living beings and the ecosystem in which they are found. Today, it is a challenge to establish strategies that allow the development of sustainable mining. Within the framework of environmental contamination, research has been carried out for the development of remediation processes and mitigation of contaminants in wastewater.

On the other hand, the toxicity of cyanide varies according to the form in which it is found. That is to say that some cyano compounds have lower toxicity, for example metal complexes. In this branch of cyanide compounds are the Prussian blue analogues (PBA), which have a wide range of applications in batteries, sensors, catalysts, absorption, and adsorption processes. This project evaluates the possibility of *in situ* synthesizing PBA's in a metal-functionalized silica material with hierarchical porosity. For this proposal, the concept of circular economy is considered since it seeks to give an added value to the cyanide content of mining wastewater by obtaining materials which can be used for hydrogen storage electrochemical catalysis, or CO_2 capture.

In this case, the hierarchical functionalized silica monolith acts as a microreactor for the formation of PBA's using the cyanide found in mining wastewater. Thus, PBA monoliths can be used for various applications in the fields of radiation decontamination and energy storage.

2.1   Objectives

2.1.1   General Objective:

To form *in situ* Prussian blue analogues of metal-functionalized silica monoliths with hierarchical porosity through contact and laminar flow impregnation processes to verify their activity as a wastewater decontamination agent.

2.1.2   Specific Objectives:

- To use the High Internal Phase Emulsion (HIPE) method to obtain a material with hierarchical porosity (macroporous-mesoporous).

- To functionalize the monoliths with copper, zinc, iron and copper-zinc mixture.

- To obtain Prussian blue analogs (PBA) *in situ* through contact and laminar flow impregnation processes.

- To characterize the funtionalized monoliths by different characterization techniques to determine the *in situ* product of the functionalized monoliths (SEM, XRD, DR-UV-Vis, ATR-FTIR, Magnetic Susceptibility Measurements).

- To verify the reduction of the cyanide concentration removal of the mining wastewater emulated in the laboratory by the use of Fe(II) and Fe(III) functionalized silica monoliths.

Chapter 3

Methodology

The methodology is divided into 4 stages which are: a) Synthesis of metal functionalized monoliths by HIPE method, b) Impregnation of functionalized monoliths under controlled conditions, c) Impregnation of functionalized monoliths by laminar flow and determination of cyanides ions, d) characterization of the monolith samples by: Scanning Electron Microscopy (SEM), X-Ray Powder Diffraction Spectroscopy (XRD), Attenuated Total Reflection FTIR Spectroscopy (ATP-FTIR), Diffuse Reflectance UV-Vis Spectroscopy (DRS-UV-Vis), Magnetic Susceptibility Measurement (MSM)**.**

3.1 Synthesis of metal-functionalized silica monoliths by HIPE method

The procedure for the synthesis of silica monoliths was based on the High Internal Phase Emulsion (HIPE) method reported by literature [81,90].

3.1.1 Materials and reagents

The reagents required for the experimental part of this project were: Pluronic P123 (purity 99%), hydrochloric acid (HCl 37%), tetraethyl orthosilicate (TEOS, 98%), sodium fluoride (NaF), copper (II) nitrate trihydrate ($Cu(NO_3)_2 * 3H_2O$, 99%) from Sigma Aldrich, iron (III) nitrate nonehydrate ($Fe(NO_3)_3 * 9H_2O$, 99%) from Alfa Aesar, zinc (II) nitrate hexahydrate ($Zn(NO_3)_2 * 6H_2O$, 98.5%) from Scharlau, iron (II) sulphate heptahydrate ($FeSO_4*7H_2O$, 99.5%) from IsoLab.

3.1.2 Experimental procedure

For the synthesis, a 20% wt. Pluronic P123 solution with pH = 2 was first prepared. Then in a 100 mL beaker on a stirring plate, the Pluronic P123 solution was added together with a nitrate or sulfate salt ($Fe(NO_3)_3*9H_2O$, $Cu(NO_3)_2*3H_2O$, $Zn(NO_3)_2*6H_2O$, $FeSO_4*7H_2O$) as appropriate. This mixture was stirred at approximately 300 rpm until the salt was completely dissolved. Then, drop by drop of TEOS was added to the acidic solution and mixed during 30 min at 400rpm allowing the TEOS hydrolyzation. After this time passed, NaF was added to regulate the polymerization of the silica precursor and the stirring was increased to approximately 700 rpm. Then cyclohexane was slowly added, and the emulsification process started. After 6 min the emulsion turned white, and the viscosity increased.

The emulsion was then poured into plastic vials to obtain the form of a monolith and was stored under a cyclohexane atmosphere and at room temperature for 8 days into a desiccator. The containers were then placed in the oven at 40 °C for 8 days.

In these last two steps, the solvent slowly evaporated and allowed the formation of macropores within the monolith. Finally, the monoliths were pyrolized in a muffla at 500 °C for 6 h with a heating rate of 1 °C/min, in order to eliminate the P123 from the structure and allow mesoporosity to appear. Figure 7 shows the flow chart of the procedure for the synthesis of metal functionalized monoliths.
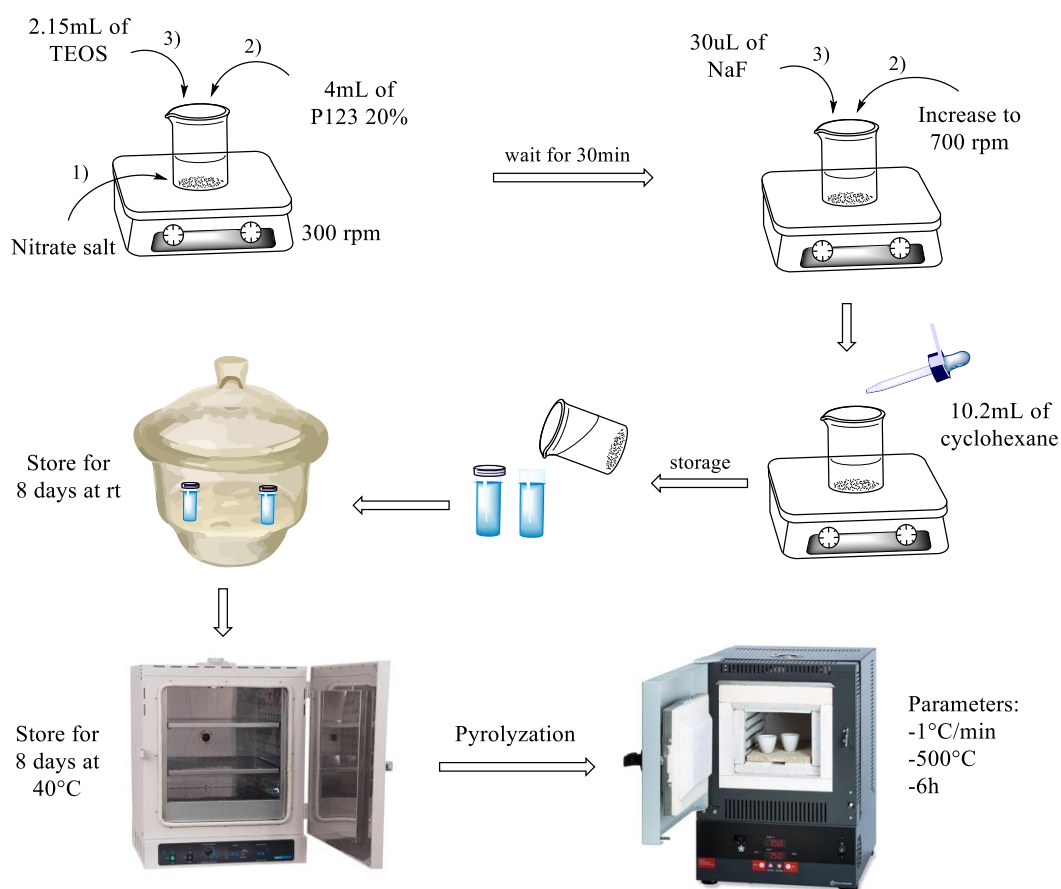
Figure 7 Flow chart of metal functionalized monoliths synthesis by HIPE method.

Moreover, the details for this experimental project about the synthesis parameters of the most relevant metal-functionalized silica monoliths are shown in the Table 7.

Table 7 The most relevant monoliths with their synthesis parameters.

Name	P123 [mL]	TEOS [mL]	NaF [µL]	Metal [mg]
Mo-FeIII	4.00	2.15	30.00	38.90
Mo-Cu	4.00	2.15	30.00	23.26
Mo- Zn	4.00	2.15	30.00	40.04
Mo- ZnCu	4.00	2.15	30.00	Zn: 40,04 Cu: 11,63
Mo-FeII	4.00	2.15	30.00	26.77
Mo-FeIII-3T	6.72	6.45	40.00	160.00
Mo-FeII-3T	6.72	6.45	40.00	160.00
Mo-Blank	4.00	2.15	30.00	No metals

3.2   Impregnation of metal-functionalized silica monoliths with ferrocyanides under controlled conditions.

The procedure for the synthesis of silica monoliths was based on the High Internal Phase Emulsion (HIPE) method because this method allows to formation of a hierarchical porous structure.reported by literature [83].

3.2.1   Materials and reagents

The reagents required for the experimental part of this project were: potassium ferrocyanide ($K_4[Fe(CN)_6]$, 99%) from Loba Chemie PVT, potassium ferricyanide ($K_3[Fe(CN)_6]$, 99%), from sigma Aldrich, distilled water, concentrated nitric acid (HNO_3, 67%).

3.2.2   Experimental procedure

First, between 0.13 g to 0.15 g of the monolith was weighed, it was placed in a 100 mL beaker. Then a 0.1 M solution of $K_4[Fe(CN)_6]$ was added. 171 µL of concentrated HNO_3 was dropped and the beaker was placed on the orbital shaker at 130 rpm. It was stirred during 4 h. The solid was then filtered under vacuum and washed until water was transparent. It was left to dry for 72 h in the oven at 40 °C. Figure 8 shows the flow chart for the ferrocyanide impregnation in metal-functionalized silica monoliths under controlled conditions.
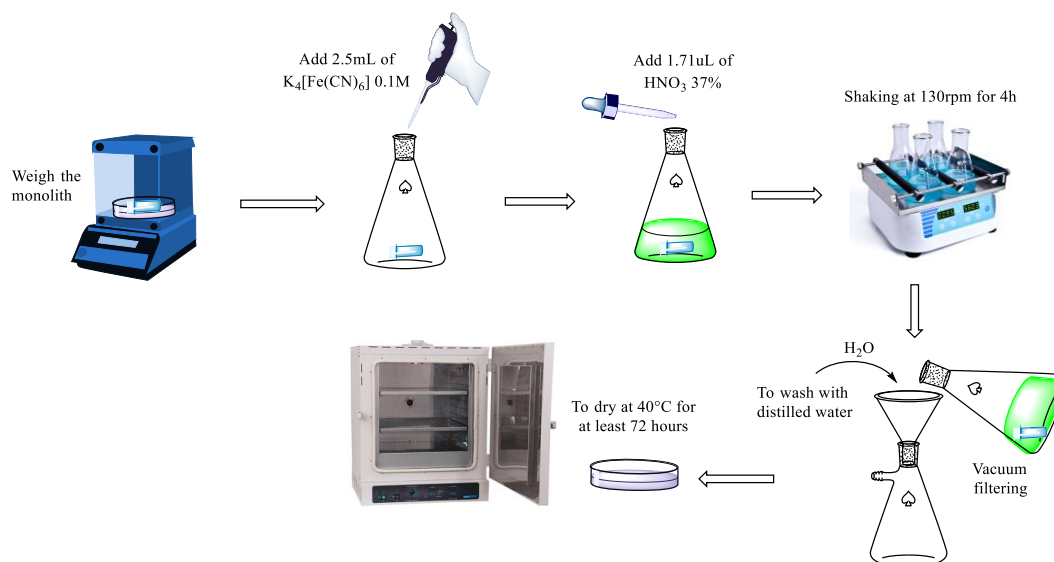
Figure 8 Flow chart of impregnation of functionalized monoliths under controlled conditions.

3.3 Impregnation of metal-functionalized silica monoliths by laminar flow and determination of cyanides ions

This procedure consists of two parts, first, the monolith was used as a microreactor in a laminar flow that simulates mining wastewater. Synthetic wastewater was prepared from the mixture of metal salts and cyanide in a 1:2 ratio. Then, the aliquots obtained from the laminar flow were analyzed to evaluate the cyanides concentration to verify if their concentration decreased.

3.3.1 Materials and reagent

0.3 mm diameter hoses, thermoplastic, heat gun (black-), syringes, 15 mL burette, 100 mL Erlenmeyer, Tefflon, 100-50 mL beakers, silver nitrate (AgNO$_3$, 99.7%) from J.T Baker, Rhodamine 6G, sodium cyanide (NaCN, bulk), iron (II) sulphate heptahydrate (FeSO$_4$*7H$_2$O, 99.5%) from IsoLab, copper (II) nitrate trihydrate (Cu(NO$_3$)$_2 * 3$H$_2$O, 99%) from Sigma Aldrich, zinc (II) nitrate hexahydrate (Zn(NO$_3$)$_2 * 6$H$_2$O, 98.5%) from Scharlau, universal holder, pasteur pipettes, syringe pump (Harvard apparatus) and tweezers.

3.3.2 Experimental procedure

Part I

Before starting the procedure, solutions of 0.5 M $FeSO_4*7H_2O$, 0.5 M $Cu(NO_3)_2*3H_2O$, 0.5 M $Zn(NO_3)_2*6H_2O$ and a 1 M NaCN solution were prepared for synthetic wastewater. Hoses with a length of 28 cm and a diameter of 3 mm were also measured and cut. Afterwards, the monolith sample was cladded with thermoplastic using a heat gun at T=500 °C. The hoses and monolith were joined as shown in Figure 9 and one end was connected to a syringe containing the emulated wastewater. The syringe was then placed in the Harvard apparatus, setted up at 2 ml/min of flow rate. The flow of wastewater passed only once through the monolith liner. In addition, aliquots were collected at the end for later quantification.

Parameters:
Rate: 2mL/min
vol: 30mL
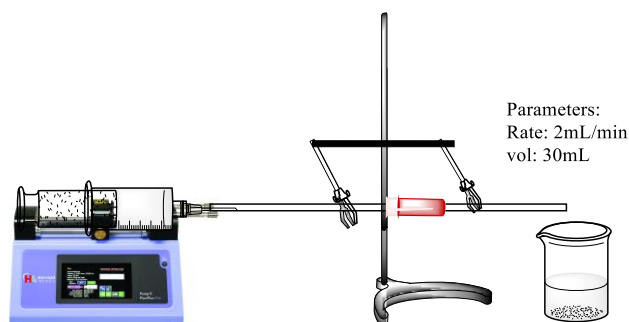
Figure 9 Flow chart of impregnation of metal-functionalized silica monoliths by laminar flow.

Part II

To analyze the concentration of cyanides in the emulated solution, a calibration curve was performed with concentrations of: 0.04 M, 0.08 M, 0.1 M, 0.3 M, 0.5 M, 0.8 M, and 1 M of NaCN. This curve had a determination coefficient (R^2) equal to 0.9974 (see in Appendix 8).

In the titration procedure, a 0.1 M solution of $AgNO_3$ and a 0.1 mg/mL solution of rodamine 6G were prepared. With the aid of a burette, $AgNO_3$ solution was dropped meanwhile 3 mL of each of the aliquots that were collected from the laminar flow were taken and 2 drops of the rhodamine 6G solution were added. The equivalence point was reached when the solution turns violet and loses its fluorescence (Figure 10).

Figure 10 Flow chart of titration technique.

3.4   Characterization techniques

The characterization of the monolith samples allowed to determine the properties of the material considering the analysis of the structure, texture and composition. The techniques used for the characterization of the material were: Scanning Electron Microscopy (SEM), Energy Dispersive Spectroscopy (EDS), X-Ray Powder Diffraction Spectroscopy (XRD), Attenuated Total Reflection FTIR Spectroscopy (AT-FTIR), Diffuse Reflectance UV-Vis Spectroscopy (DRS-UV-Vis), y Magnetic Susceptibility Measurement (MSM). In addition, the titration argentometric method was used to determine cyanides in the water flow. This volumetric method was described in part II of section 3.3.2.

3.4.1   Scanning Electron Microscopy (SEM)

SEM allows to obtain information about the texture of the samples. The technique consists in the analysis of surfaces with an electron beam and images are produced from reflected electron beams [91]. In the images it is possible to observe the characteristics that the sample presents on its surface. For this characterization the samples were taken from the dry monoliths in the different stages of the experimental process.

SEM images were obtained from the Phenom ProX microscope with an optical light magnification of 27-160 X and an electron optical magnification range of 160-350000 x. Magnifications of 1000 x, 3000 x, 5000 x, and 10000 x were used for this experiment. In addition, the energy dispersive X-ray spectrometry (EDX) experiment was carried out with the standard detector of the equipment using an accelerating voltage of 10 kV to 15 kV.

3.4.2 X-Ray Powder Diffraction Spectroscopy (XRD)

The XRD technique allows the characterization of solids by loading particles of the material with X-rays to quantify the crystallinity of the material. This technique consists of causing an X-ray beam to interact with the planes of atoms within the material [92,93].

Initially the samples were pulverized, and the analysis was carried out using the MiniFlex-600 X-ray diffractometer from Rigaku with D/tex Ultra2 detector. The diffractograms were taken at a scanning speed of 30°/min with a step of 0.01 ° in the 2 θ' range of 3 ° - 140 °.

3.4.3 Attenuated Total Reflection FTIR Spectroscopy (ATR-FTIR)

The principle of the IR technique uses the vibrational information of the covalent bonds of organic and inorganic compounds which is possible to identify the type of bond based on the absorption of electromagnetic radiation frequencies in the infrared region ($400cm^{-1}$ to $4000cm^{-1}$) that occur when the molecules are excited [94]. This is possible because there is a characteristic vibrational frequency for each type of bond, similar to fingerprints.

The Agilent Cary 630 FTIR spectrophotometer with attenuated total reflactance (ATR) sampling module and diamond tip was used for infrared spectrophotometry. The samples were evaluated in the range of 400-4000 cm^{-1}. All spectra result from the average of 64 measured scans.

3.4.4 Diffuse Reflectance UV-Vis Spectroscopy (DRS-UV-Vis)

DRS-UV-Vis is a non-destructive surface analytical technique. It allows to obtain information about solid materials by analyzing their surface. The principle of this technique is based on measuring the relative change in the amount of light reflected from a surface in the near and mid-infrared regions [95]. To do this, the sample is irradiated with an electromagnetic beam source which will be reflected as a function of wavelength following the principles of optical geometry [96]. The Kubelka Munk function is used to analyze the spectra obtained by DRS-UV-Vis [96].

To obtain the electronic absorption spectra, the PerkinElmer LAMBDA 1050 UV / Vis / NIR spectrophotometer was used, with deuterium and tungsten-halogen lamps. The

equipment was used with the Praying Mantis module in the range of 350 cm^{-1} to 800 cm^{-1} and commercial silica was used as a target.

3.4.5   Magnetic Susceptibility Measurement (MSM)

These measurements were taken with a magnetic balance which is a laboratory instrument that allows obtaining information about the magnetic susceptibility (X) of the compounds. The X is the magnetization capacity of the material by the intensity of an applied magnetic field [13].

The magnetic susceptibility was determined on the Sherwood scientific magnetic balance. Before starting the measurements, it is necessary to zero the magnetic balance and take the measurement of the target.

Chapter 4

Results and discussion

The analysis of the results is divided into three stages: a) synthesis and functionalization of the silica monoliths (pyrolized and non pyrolized), b) formation of PBA's in the monoliths by different impregnation processes and c) characterization of metal funtionalized silica monoliths by each of the experimental steps. Followed by a preliminary study to evaluate monoliths as mitigating agents for mining wastewater. First, it started to examine the monoliths in the process of synthesis and functionalization. The results of the non pyrolyzed monoliths are shown below. For this, the physical change of the monolith samples was analyzed, then the changes in the structure, texture and properties of the functionalized monoliths.

4.1   Metal-functionalized silica monoliths by HIPE method

The metal-functionalized silica monoliths were synthesized by the HIPE method to obtain hierarchical porosity (macroporosity-mesoporosity) within the material and with metals dispersed into the skelet [83].

Before the pyrolyzation process at 500 °C, changes in the shades of the monoliths were observed. The Mon-Zn sample is white because of the zinc, Mon-Cu is light blue because of the copper, Mon-ZnCu is slightly lighter blue, and the Mon-Fe is yellow because of the iron. All the colors of the monoliths have pastel shades (see Figure 11). The color change was caused to incorporating the metal nitrate hydrates in the structure of the material.
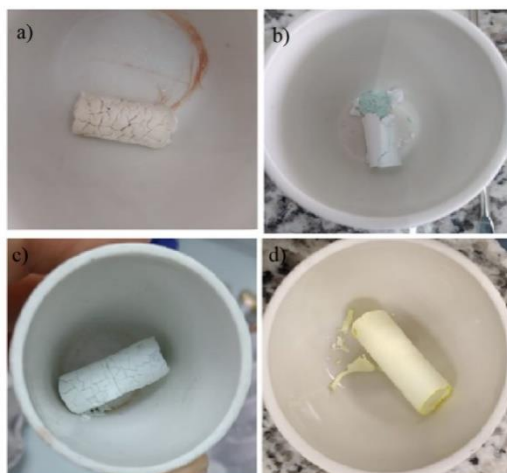
Figure 11 Metal-functionalized silica monoliths after the pyrolyzation process.
a)   Mon-Zn, b) Mon-Cu, c) Mon-ZnCu, and d) Mon-Fe

4.1.1 Attenuated Total Reflection FTIR Spectroscopy (ATR-FTIR)

The first characterization performed on the funcionalized silica monoliths was an ATR-FTIR analysis to check the change in chemical structure after pyrolyzation of the samples. Figure 12 shows the ATR-FTIR spectra corresponding to the analysis of the samples Mon-Zn, Mon-Cu, Mon-ZnCu, and Mon-Fe before pyrolyzing in the range of 400-4000 cm^{-1}.
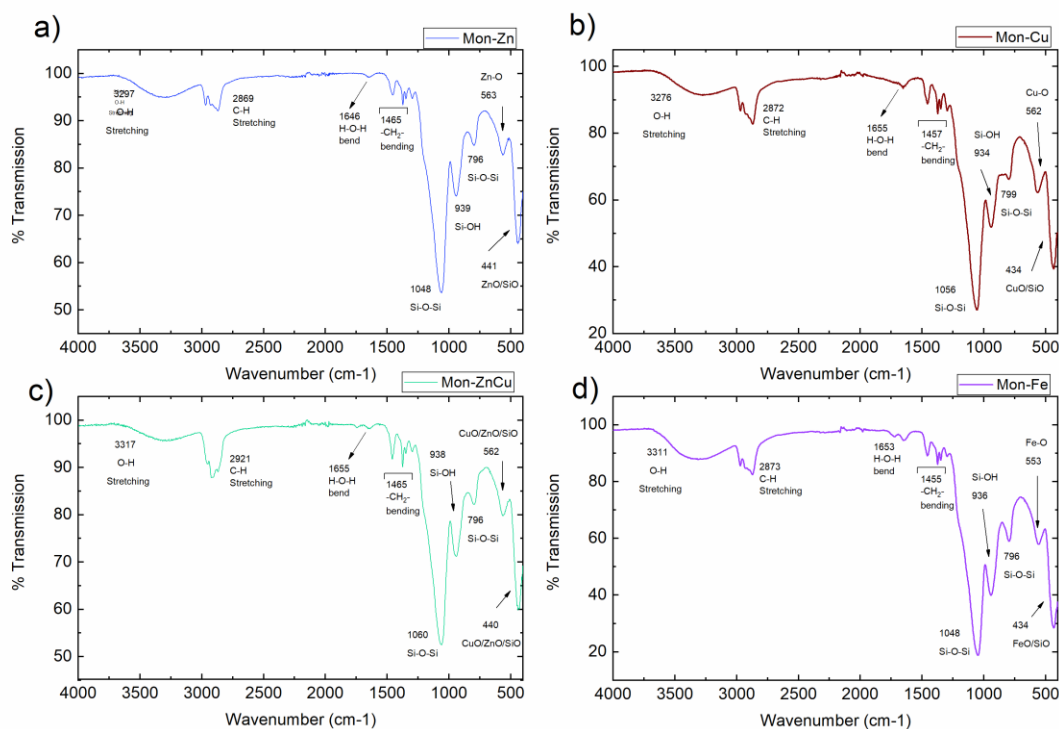
Figure 12 Infrared spectra of non-pyrolyzed metal functionalized silica monoliths samples: a) Zn monolith, b) Cu monolith, c) ZnCu monolith and d) Fe monolith

In general, in four spectra shown in Figure 12, the bands corresponding to water and the alkane group can be observed. The broad band observed in the range 3278-3317 cm^{-1} corresponds to the stretching vibration of the O-H group [39,94]. This signal corresponds to water molecules, as it is complemented by the bending vibration band found around at 1655 cm^{-1} [94,97,98]. Also, bands appearing in the range of 3000-2850 cm^{-1} are related to stretching vibrations of alkane group, and the bands found between 1455-1465 cm^{-1} are associated to bending vibrations.

The bands corresponding to the alkane group signals indicate the presence of Pluronic P123 in the structure of the functionalized monoliths before pýrolization. The bands around of 2865 cm^{-1} correspond to the presence of the copolymer chains still present in

the monolith structure, which serve as a template for the hierarchical porosity of the monolith. This signal disappears when the metal-functionalized monolith samples are pyrolyzed. [83,90]. It is important to mention, that the bands that indicate the structural changes in the synthesis and impregnation process are found in the fingerprint zone [62,97]. The bands that appear below 900cm-1 complement this information [62].

Furthermore, it is observed that the characteristic bands for the Si-O-Si bond are found between 434-441 cm^{-1} corresponding to the asymmetric bending vibration and the bands between 796-799 cm^{-1} are related with the symmetric stretching vibrations of Si-O-Si [99]. The band between 1048-1060 cm^{-1} belongs to the asymmetric stretching vibration of Si-O-Si bond [98].

The bands between 936-939 cm^{-1} are assigned to the Si-OH stretching vibration [100]. In each of the spectra, particular signals are found in the range from 400 cm^{-1} to 600 cm^{-1} since the signals corresponding to the Zn-O and Cu-O bonds appear in this zone [99,101].

However, the color change in the monolith after the calcination process indicates that the metals are functionalized in the silica matrix. The samples Mo-Zn, Mon-Cu, Mon-ZnCu, Mon-Fe samples were pyrolyzed them at 500 °C for 6 h at a rate of 1 °C/min. The spectra corresponding to the samples are shown in Figure 13.
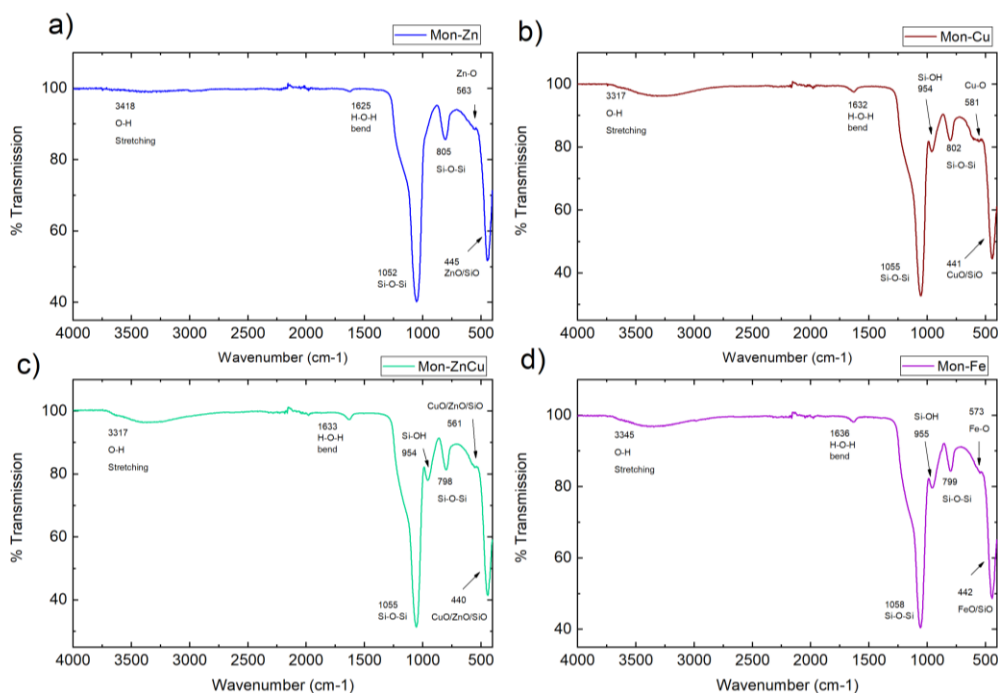
Figure 13 Infrared spectra of pyrolyzed metal functionalized silica monoliths. a) Zn monolith, b) Cu monolith, c) ZnCu monolith and d) Fe monolith

It can be generally observed that for whole samples the bands indicating the presence of Pluronic P123 in the structure are no longer shown in the spectra. This is due to the fact that in the pyrolyzation process the P123 was removed from the skeleton of the funtionalized monolith. In this sense, it can be said that the choose treatment was good enough to free the mesoporosity of the samples.

In addition, the band corresponding to the O-H stretching vibration signal in the 3278-3317 cm^{-1} range decreased in intensity because part of these groups was also removed by pyrolyzation. The H-O-H bond bending vibration signal corresponding to the water molecules in the structures remains present because silica is highly hydrophilic [97].

One of the objectives of the synthesis process was to obtain CuO/SiO_2, $CuZn/SiO_2$, ZnO/SiO_2, FeO/SiO_2. This can be verified on the pyrolyzed monoliths with this technique as well as DRS-UV-Vis, and XRD. To check the presence of ZnO in the structure two characteristic peaks are shown at 430 cm^{-1} and 499 cm^{-1} [101]. Figure 13a shows the 445 cm^{-1} band corresponding to the Zn-O signal. The 805 cm^{-1} band is assigned to the symmetric Si-O-Si stretching vibration, while the 1082 cm^{-1} band corresponds to the asymmetric Si-O-Si stretching vibration signal [97,98].

Figure 13b, shows the bands at 441 cm^{-1} and 510 cm^{-1}, these are associated with the Cu-O stretching vibrations [99]. The three peaks at 802 cm^{-1}, 954 cm^{-1}, and 1055 cm^{-1} correspond to the symmetric Si-O-Si stretching vibrations, silanol group signal, and asymmetric Si-O-Si stretching vibration respectively [97,98]. In Figure 13c one can see the 440 cm^{-1} and 512 cm^{-1} bands which are attributed to the presence of Cu-O or Zn-O because the signals are very close between them and they can overlap [99,101]. The bands at 798 cm^{-1}, 954 cm^{-1}, and 1055 cm^{-1} correspond to the aforementioned characteristic Si-O-Si signals [97,98].

In Figure 13d, the characteristic bands of silica are observed as well. The 442 cm^{-1} band corresponds to the Si-O-Si stretching vibrations, the 936 cm^{-1} band is assigned to the silanol group signal. While the band at 573 cm^{-1} corresponds to the Fe-O stretching vibrations [98].

4.1.3 Scanning Electron Microscopy (SEM)

Samples of the functionalized silica monoliths and the reference (silica monolith without metals Mon-Blank) were analyzed by SEM and EDX to visualize porosity, and the presence of metals.

In the Figure 14b the SEM analysis of the Mon-Blank is shown at a magnification of 5 Kx in which the porosity of the material before the pyrolyzation process can be observed. The pores are present in the structure, product of the evaporation of the cyclohexane used for the emulsification. The formation of these pores was promoted by the polycondensation of the silicon source around the oil droplets during the emulsion process[81,83]. While in the Figure 14b it can be observed how the pores of the Mon-blank sample are better defined because of the pyrolyzation process.
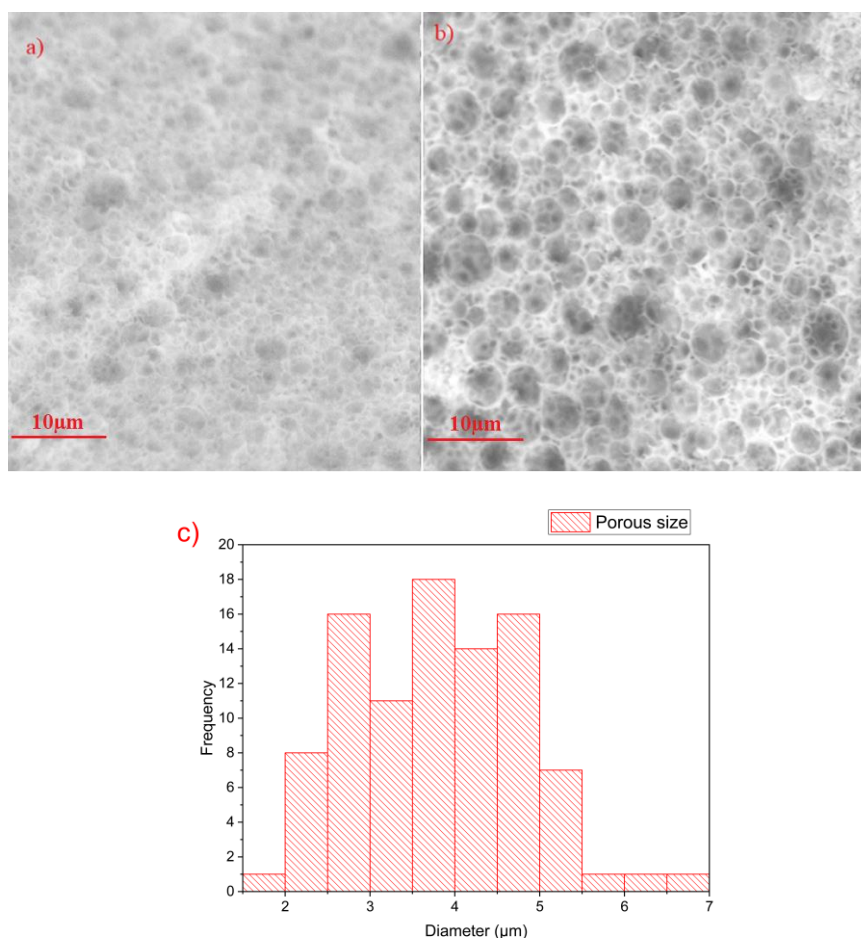
Figure 14 SEM images: a)non-pyrolyzed Mon-Blank at 5Kx magnification, b) pyrolyzed Mon-Blank at 5Kx magnification, and c) Porosity distribution of the pyrolyzed Mon-Blank performed by ImageJ.

Using the ImageJ program it was determined that the mean pore size distribution of pyrolyzed Mon-Blank was equal to 3.802 μm and standard deviation equal to 0.9806 μm. The length range for this distribution was 1,782 μm to 6,563 μm (Figure 14c).

This method used to determine the pore size distribution of the Mon-Blank sample is not applicable for SEM micrographs of the metal-functionalized silica monolith samples in this section (pyrolyzed and unpyrolyzed). As shown in Figures 15-16 it is not possible to differentiate the pore boundaries from each other.

Continuing with the SEM analysis of the Cu, Zn and Zn-Cu functionalized silica monoliths, the Figure 15 shows the samples before the pyrolysis process. In the three SEM micrographies, it can be seen that the material has defined porosity, and the skeleton walls of the silica structure are thin and compact for the three of them. The samples Mon-Cu, Mon-Zn, Mon-ZnCu and Mon-Blank (Figure 14a) samples show no differences before the pyrolyzation process.
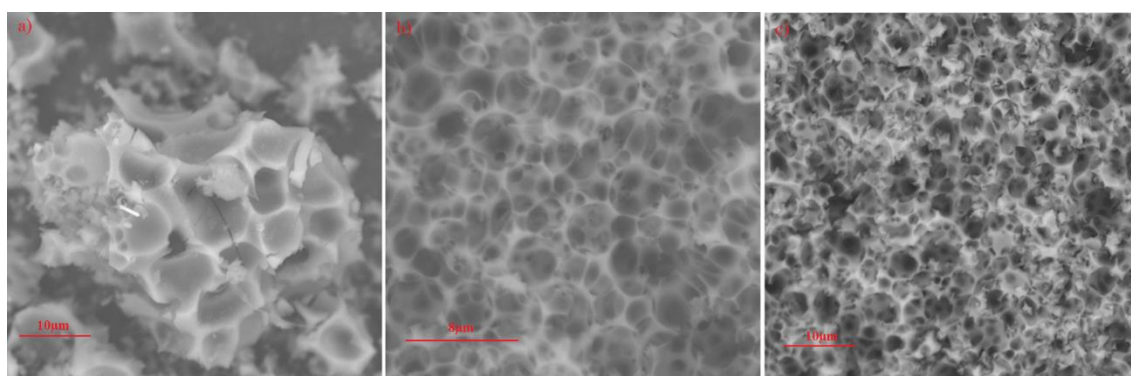
Figure 15 SEM images of non-pyrolyzed silica monoliths: a) Mon-Cu at 5Kx magnification, b) Mon-Zn at 10Kx magnification, c) Mon-ZnCu at 5Kx magnification.

Figure 16 shows the SEM images corresponding to the Mon-Cu, Mon-Zn, Mon-ZnCu samples after the pyrolyzation process. A higher definition is observed in the pores and in the skeleton of the material. It is expected that the metals are dispersed in the silica walls of the monolith. Furthermore, they should be located in the mesopores because they are dissolved in the aqueous phase of the emulsion corresponding to the surfactant molecules, which are removed in the pyrolyzation process.
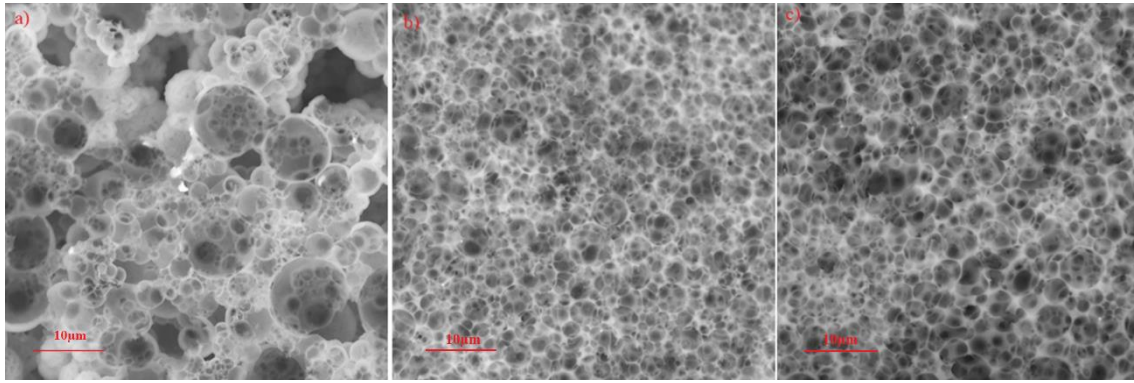
Figure 16 SEM images of pyrolyzed silica monoliths: a) Mon-Cu at 5Kx magnification, b) Mon-Zn at 5Kx magnification, c) Mon-ZnCu at 5Kx magnification

The elemental composition of the monoliths was determined by Energy Dispersive X-ray spectroscopy (EDX) analysis (see Table 8). It was found for non pyrolyzed and pyrolyzed monoliths silicon, and oxygen in higher percent. The Mon-Cu sample shows less percentage of silicon in the structure (4.46%), this is due to the fact that in the EDX analysis the zone being examined is delimited to a spot. The EDX images showing the analysis spots can be seen in the appendix section (see Appendix 1).

After the pyrolyzation process, large metallic dots can be observed in the image of item a). While the images of items b and c are small and higher magnification is needed to observe them better (Figure 16).

Table 8 Atomic percent of metals by Energy Dispersive X-ray (EDX) analysis in the pyrolized monoliths.

Samples	Atomic percent of metals (%)		Atomic percent of silicon (%)	Atomic percent of oxygen (%)
Mon-Cu	Cu: 1.34		4.46	48.56
Mon-Zn	Zn: 2.66		29.17	68.17
Mon-ZnCu	Cu: 1.49	Zn: 2.12	20.95	68.53

EDX analysis determined that the metals are found in atomic concentrations lower than 3 (see Table 8). The concentrations for copper and zinc are in ranges from 1.34% to 1.49% and from 2.12% to 2.66% respectively. In addition, the element found in the highest proportion in the monolith structure is oxygen. The percentage ranges from 48.56% to 68.53%. These results are generally in concordance with the literature [97].

4.1.2   X-Ray Powder Diffraction Spectroscopy (XRD)

After texture analysis of the metal-functionalized silica monoliths, XRD was used to examine the crystal structure of the monolith samples and compared with their respective non-pyrolized precursors. For this analysis, the samples were first pulverized.

The XRD results for the Mon-Cu, Mon-Zn and Mon-ZnCu samples before and after the pyrolyzation process are reported in Figure 17. The diffractograms show the characteristic profile for the amorphous silica phase, reported by Musić in 2011 and Prabhakaran in 2016 [97,98]. This broad peak appears near to $°2\theta = 22$ °.

Diffractogram of the non pyrolyzed samples show a peak with the equivalent Bragg angle at $°2\Theta = 14$ °. However, the peak signal reported in the literature is $°2\theta = 21\text{-}22$ ° which is closer to the signal of amorphous silica after the pyrolyzation process (Figure 17b). The peak observed for the samples after the pyrolyzation process is at $°2\theta = 22.26$ ° indicating that the amorphous silica structure because the broad peak is maintained. The shift can be attributed to an expansion of the porosity when the surfactant is released [102].
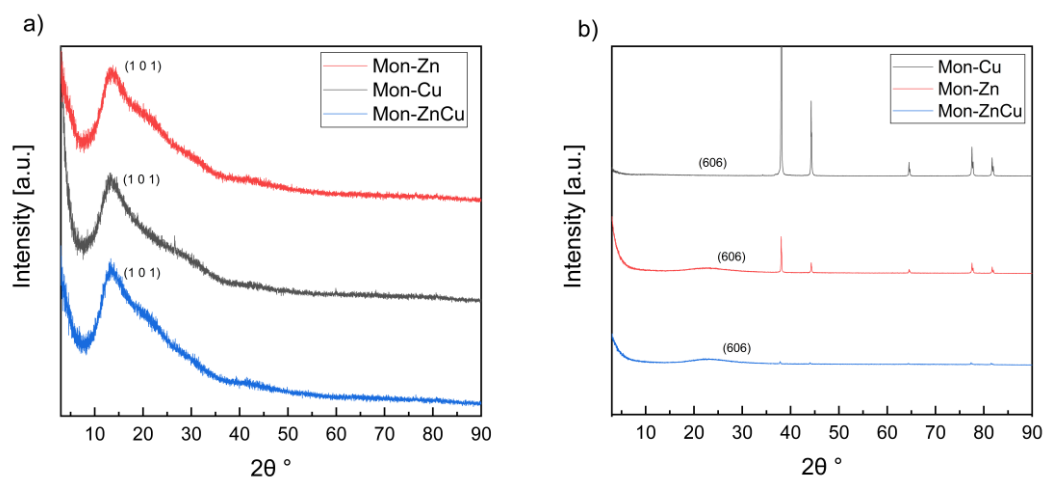
Figure 17 Diffractograms of metal functionalized silica monoliths. a) before pyrolysis and b) after pyrolysis.

The signals observed in Figure 17b for the Mon-Cu, Mon-Zn samples present more peaks in the range of $°2\theta = 40\text{-}140$ °, which correspond to the sample holder made of aluminum. In addition, in the patterns, peaks different from that of silica are not observed because the Metal/SiO_2 ratio is low and the detection limit of the equipment was programmed for higher contents.

4.1.4   Diffuse Reflectance UV-Vis Spectroscopy (DRS-UV-Vis)

DRS-UV-Vis spectrum made possible to determine the presence of the metal groups in the structure of the functionalized monoliths.

Figure 18 shows the absorption spectrum for the Mon-Blank. Figure 18a shows the spectrum of non pyrolized silica monoliths. Its absorption bands are observed at 376 nm, 480 nm, and 540 nm which are correlated to Si-O signals [103–105].

After pyrolyzed was obtained the follow absorption spectrum (Figure 18b). The absorption bands that appear at 379 nm and 488 nm is attributed to Si-O signals, and 760 nm that related to Si-O-Si signals [103,105]. The range of the absorption bands 200-800 cm^{-1} matches with literature [104]. Besides, these Si-O-Si related absorption bands confirm the information obtained from the ATP-FTIR results.
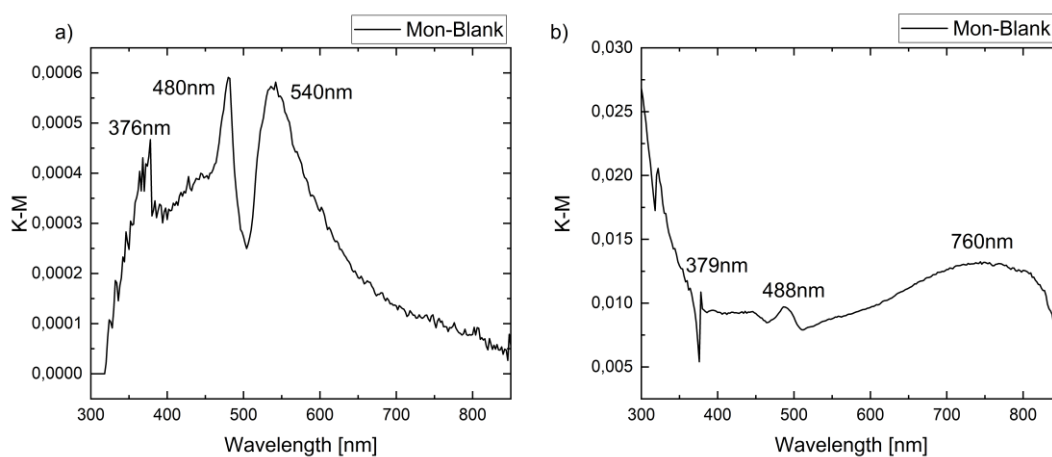
Figure 18 DRS-UV-Vis of Mon-Blank. a) before pyrolysis and b) after pyrolysis

These results are complemented with those of ATP-FTIR, confirming the presence of ZnO/SiO2, CuO/SiO2, and FeO/SiO2, dispersed within the silica matrix. Figure 19 shows the DRS-UV-Vis spectra corresponding to the analysis of the Mon-Zn, Mon-Cu, Mon-ZnCu and Mon-Fe non pyrolyzed samples.
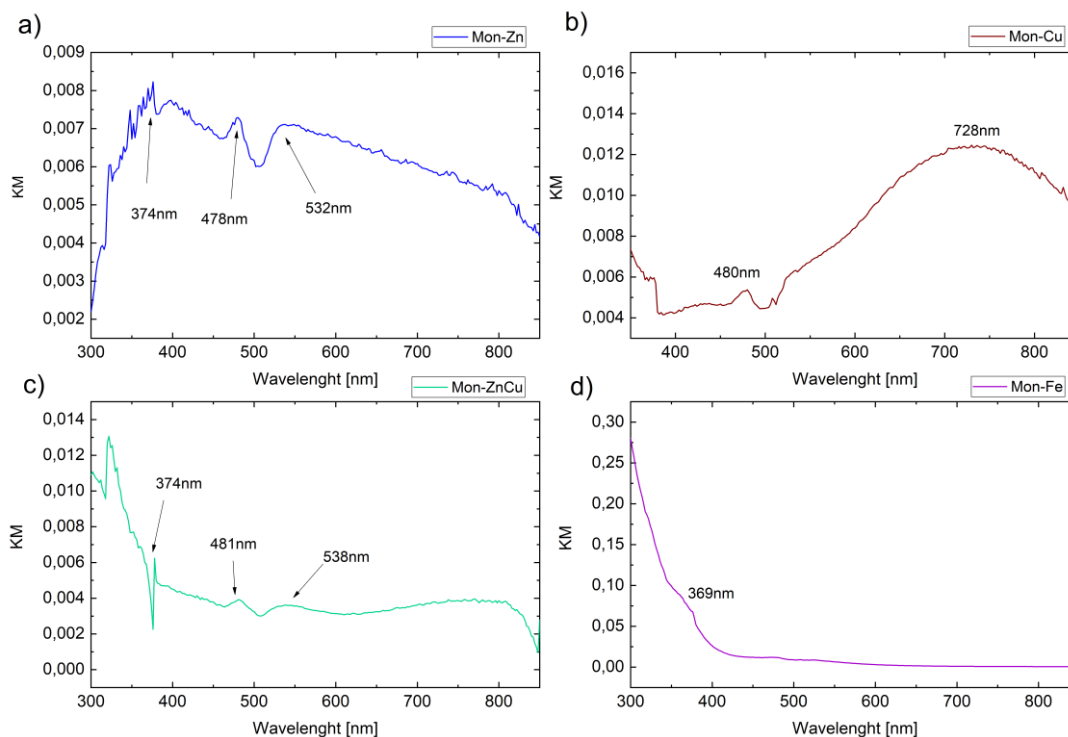
Figure 19 DRS-UV-Vis of non pyrolyzed metal functionalized silica monoliths. a)
Mon-Zn b) Mon-Cu, c) Mon-ZnCu, and d) Mon-Fe.

The spectra of the functionalized monolith samples before the pyrolysis process and of
the Mon-Blank sample show bands that match each other. The bands match the spectrum
of the Mon-Blank sample (Figure 18). In the Figure 19 it was found similar bands that
the ones for Mon-Blank before pyrolysis in the spectra a) and c). While in spectrum b)
the absorption band at 728 nm is related to the Cu(II) particles in the sample according to
literature [106]. The only absorption band in spectrum d) appears at 369 nm, which could
correspond to one of the Mon-Blank signals [107].

The spectra of the samples before and after the pyrolyzation process (Figure 20).
However, the Mon-Zn signals after this process are clearer. Figure 20 shows the DRS-
UV-Vis spectra corresponding to the analysis of the Mon-Zn, Mon-Cu, Mon-ZnCu and
Mon-Fe samples.
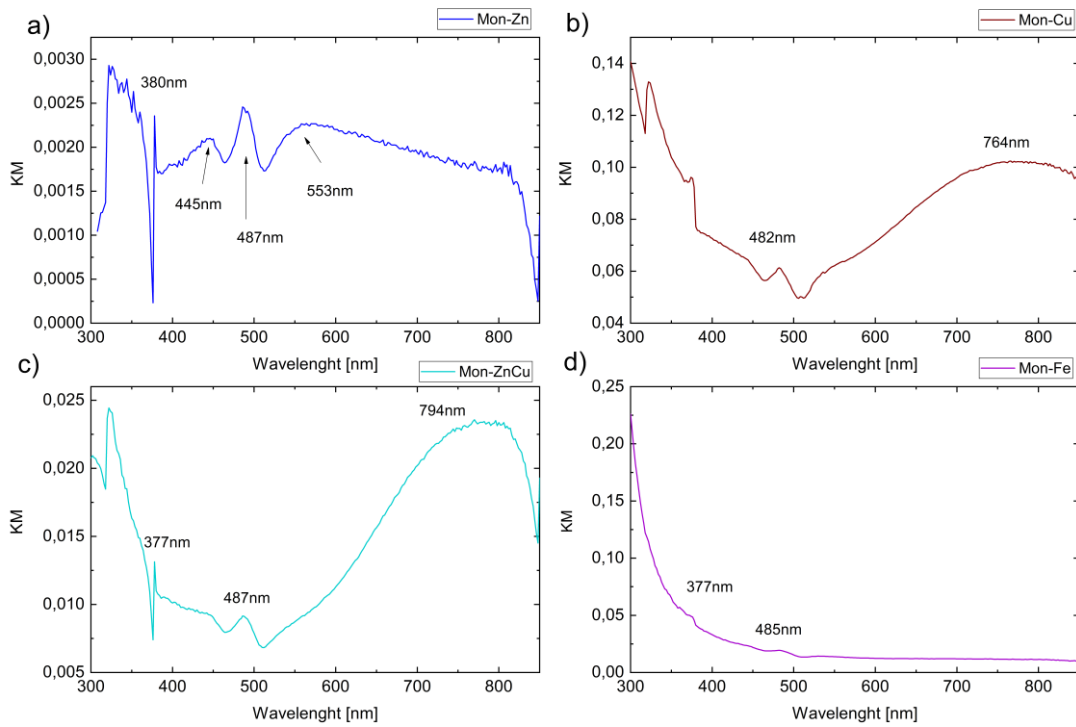
Figure 20 DRS-UV-Vis of pyrolyzed metal functionalized silica monoliths. a) Mon-Zn b) Mon-Cu, c) Mon-ZnCu, and d) Mon-Fe

The spectrum shown in Figure 20a corresponding to the Mon-Zn sample show peaks around 380 nm, indicat the presence of Zn [101,103].The absorption bands found around 800 nm and at 256 nm in Figure 20*Figure 19*b are assigned to the signal of Cu(II) in the porous structure [101]. While the signals around 410 nm and 520 nm in Figure 20d related to FeO bound. At the same time, this band can be attributed to the functionalization of iron in the matrix [101,108]. In the spectrum of Figure 20c, peaks corresponding to the presence of Zn and Cu can be found. This could be determined by the matches in the literature with the spectra obtained during the characterization [101,107,109,110].

When comparing the spectra of the pyrolyzed samples, it can see that the signals of pyrolized samples are clear because the silica matrix of monoliths only has metals in the skeleton (Figure 20) with the spectra of the Mon-Blank (Figure 18) it is observed that the spectra that have greater similarity with those that correspond to the Mon-Zn and Mon-ZnCu samples. However, similarities are also observed with the expected absorption bands for CuO/SiO_2, ZnO/SiO_2, FeO/SiO_2, are related with functionalization of the monolith.

The absorption bands observed in the different electronic spectra in Figure 18 and Figure 19 show bands >500nm these are attributed to charge transitions between the ligand and the central metal, while bands >500nm are related to charge transfer between the $\pi \rightarrow \pi^*$ orbitals in the ligand [101]. Table 9 shows the wavelength values for the absorption bands found in the spectra of Figure 19 and Figure 20 together with the expected bands for the metals in a silica matrix [100,101,111,112].

Table 9 Summary of signals for DRS-UV-Vis. Comparison between experimental signals and expected signals.

Monoliths samples	DRS-UV-Vis experimental signals of non pyrolyzed monoliths	DRS-UV-Vis experimental signals of pyrolyzed monoliths	DRS-UV-Vis expected signals for oxides in matrix
Mon-Zn	374 nm, 478 nm, 532 nm	380 nm, 445 nm, 487 nm, 553 nm	200-400 nm ˜380 nm
Mon-Cu	480 nm, 728 nm	482 nm, 764 nm	256 nm, 800 nm
Mon-ZnCu	374 nm, 481 nm, 538 nm	377 nm, 487 nm, 794 nm	256 nm, 380 nm, 800 nm
Mon-Fe	369 nm	377 nm, 485 nm	410 nm, 520 nm

As can be seen in Table 9, the Mon-Cu and Mon-ZnCu samples present absorption bands very close to the expected values. For the Mon-Zn sample it can be observed that there are bands complementary to the expected ZnO/SiO_2 signal and the bands of the Mon-Fe samples present a hypsochromic shift of the expected bands. It can be caused by the changed of metals in the structure. These shifts are very dependent on the polarity of the solvent when they are performed in liquid phase [102]. In the same way, when a solid matrix contains the analyte of interest acts just as the liquid solvent [106].

4.1.5 Magnetic Susceptibility Measurement

Through the measurement obtained in the magnetic balance, the value for mass suceptibility (Xg) and the magnetic character of the complex were determined (Table 10 and Porous silica has a diamagnetic character, however when it is doped with metal oxides its magnetic properties change [113.] Table 11 shows the magnetic susceptibility values for

Mon-Zn, Mon-ZnCu and Mon-Cu monoliths after the pyrolyzation process. These samples change their magnetic character.

Table 11).

Table 10 Experimental magnetic balance measurements of non pyrolyzed metal functionalized silica monoliths

Non Pyrolyzed Monolith	Experimental Measurement [ergs]	Magnetic Property
Mon-Zn	-1,48E-06	Diamagnetic
Mon-Cu	-1,59E-06	Diamagnetic
Mon-CuZn	-4,36E-07	Diamagnetic

Porous silica has a diamagnetic character, however when it is doped with metal oxides its magnetic properties change [113]. Table 11 shows the magnetic susceptibility values for Mon-Zn, Mon-ZnCu and Mon-Cu monoliths after the pyrolyzation process. These samples change their magnetic character.

Table 11 Experimental magnetic balance measurements of pyrolyzed metal functionalized silica monoliths

Pyrolyzed Monolith	Experimental Measurement	Magnetic Property
Mon-Zn	6,08E-07	Paramagnetic
Mon-Cu	1,40E-06	Diamagnetic
Mon-CuZn	3,32E-07	Paramagnetic

The change in the magnetic character of the monoliths is estimated to be because of the removal of Pluronic P123 and the metal ions are more exposed.

4.2 Impregnation with ferrocyanide of metal functionalized monoliths under controlled conditions

The impregnation process of the metal functionalized monoliths was carried out at room temperature for 4 h. Reaction (4) describes what was expected during the contact impregnation process, where the metals found in the silica matrix react with potassium ferrocyanide giving rise to Prussian blue analogs.

$$M^n + K_4Fe(CN)_6 \rightarrow K\_M^n_{6-m}[Fe^m(CN)_6]^{6-m}_n \qquad (4)$$
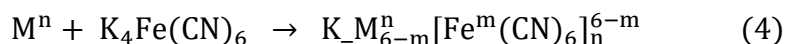
Some of the complexes expected for this section are: $A_2Cu[Fe(CN)_6]$, $A_2Zn[Fe(CN)_6]$, $A_2Fe[Fe(CN)_6]$ where A can be an alkali metal such as: sodium, potassium, or cesium. The compounds formed in the silica monoliths are insoluble in water, and present colors corresponding to the colloidal suspensions formed in the synthesis of PBA's [83,114,115]. Figure 21 shows the metal functionalized silica monoliths after impregnation under controlled conditions. The monoliths underwent a color change, indicating that a reaction occurred within the monoliths. So, Mon-Zn became yellowish color, Mon-Cu became wine-red color, Mon-ZnCu became gray color and Mon-Fe became blue color.
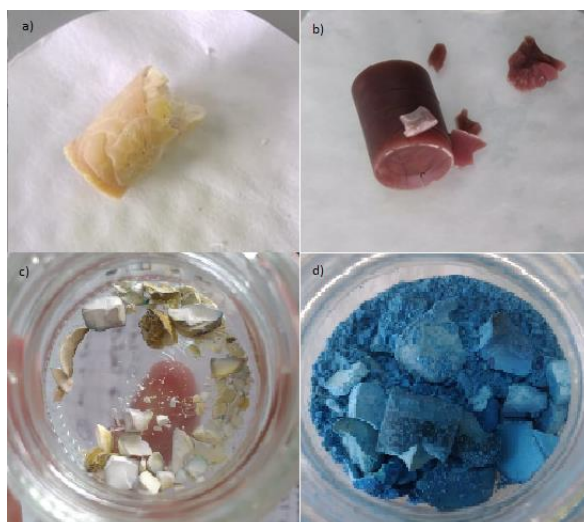
Figure 21 Metal functionalized silica monoliths after contact impregnation under controlled conditions

For this section work, the nomenclature of the monoliths samples changed for a better comprehension. Therefore, the impregnated samples are: Mon-ZnHF, Mon-CuHF, Mon-ZnCuHF, Mon-FeHF.

4.2.1 Attenuated Total Reflection FTIR Spectroscopy

At this point of the work, ATR-FTIR spectroscopy was used to analyze the chemical structure of the monolith after the contact impregnation process at controlled conditions. This was done in order to visualize the bands that confirm the PBA formation in the different functionalized silica monoliths. For the formation of PBA's the CN^- group binds to the metals through a σ bond with π bond, the signal observed for the stretching vibration of this bond varies as a function of changes in the electronegativity of the metals and their oxidation states [116].

Figure 22 shows ATP-FTIR spectrum for the samples Mon-ZnHF, Mon-CuHF, Mon-ZnCuHF, Mon-FeHF. Also, All FTIR spectra corresponding to Figure 22 present the signals corresponding to silica and water. The absorption bands are detailed in the previous section.
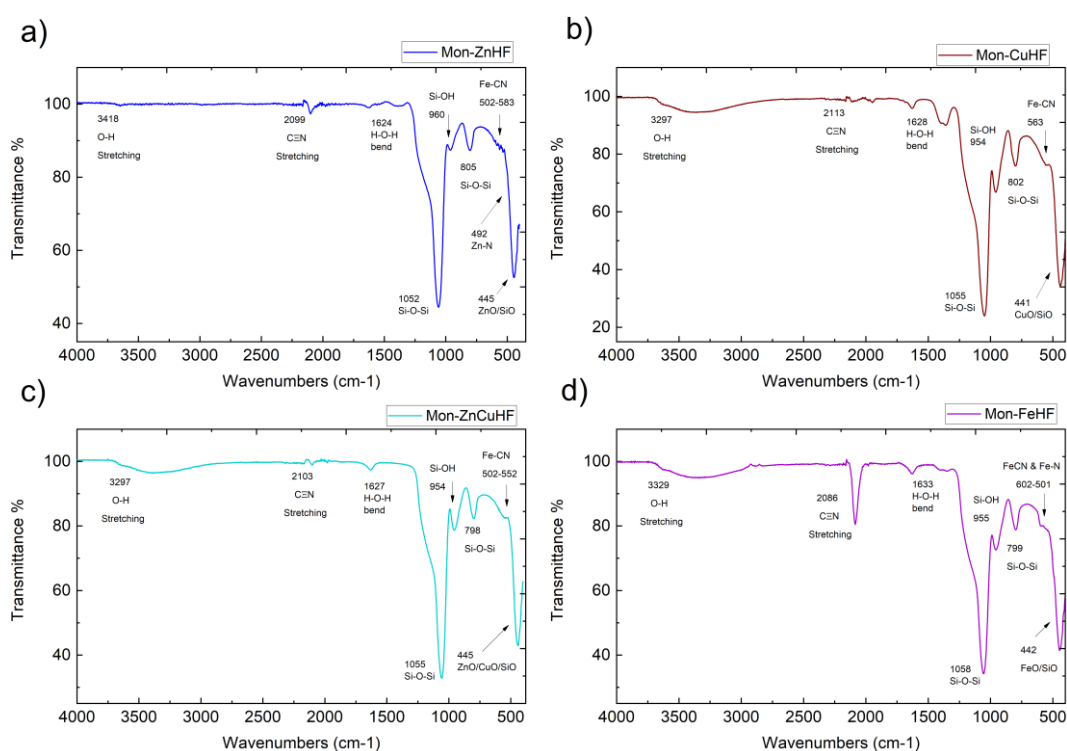
Figure 22 Infrared spectrum of metal functionalized silica monoliths after impregnation under controlled conditions. a) Mon-ZnHF, b) Mon-CuHF, c) Mon-ZnCuHF d) Mon-FeHF.

PBAs present five absorption bands in the IR spectrum, of which three bands are related to the $Fe(CN)_6$ molecular block [62,117]. The band appearing in the FTIR spectrum in the

range from 2200 cm^{-1} to 2000 cm^{-1} corresponds to the torsional vibration signal for the binding of the C≡N ligand in Prussian blue analogs [62,118]. This band allows the identification of the oxidation states of metals as the CN bond is very sensitive to changes in the surrounding environment. The stretching vibrations appearing around to 2000-2100 cm^{-1}, 2110-2150 cm^{-1}, 2145-2200 cm^{-1} correspond to the signals of Fe^{II}-CN-M^{II}, Fe^{II}-CN-M^{III}, Fe^{III}-CN-M^{II} bonds respectively [62,109,117–119]. Where M is equivalent to transition metals that complement the chemical structure of the complex.

In addition, the band around ~501 cm^{-1} corresponds to the elongation vibrations of the Fe-CN bond, so the torsional vibrations of the same bond are related to the ~598 cm^{-1} band [109,117]. The characteristic bands for Zn-PBA appear around 2091-20100 cm^{-1}, and 489 cm^{-1} corresponds to the Fe^{II}-CN-Zn and Zn-N stretching vibrations respectively [110,120,121]. The bands corresponding to the silica and water signals are observed. In addition, Table 12 details the signals assigned to Mon-ZnHF, these signals coincide with those reported in the literature.

Table 12 FTIR spectrum bands corresponding to Mon-ZnHF

Bands	υ (Fe^{II}-CN-Zn)	υ (Zn-N)	υ (Fe-CN)	δ (Fe-CN)
Mon-ZnHF	2099 cm^{-1}	492 cm^{-1}	502 cm^{-1}	583 cm^{-1}

The band corresponding to the Zn-N stretching vibration is superimposed with the signal of the asymmetric Si-O-Si bond appearing at 441 cm^{-1} [121].

The characteristic bands for Cu-PBA corresponding to the stretching vibrations of the Fe^{III}-CN-Cu^{II} and Fe^{II}-CN-Cu^{II} bond are very close 2178 cm^{-1} and 2093 cm^{-1}, respectively [116]. In the infrared spectrum corresponding to the Mon-CuHF sample (Figure 22b), a small signal is observed at 2113 cm^{-1} that could be attributed to the vibrations of the Fe^{III}-CN-Cu^{II} bond. The band corresponding to the Cu-N bond appears in the range 170-280 cm^{-1} so it is not possible to see them because the measurement was carried out in the middle region of IR [122]. However, a band around 563 cm^{-1} can be observed which is assigned to the vibrations of the Fe-CN bond [106,110,121].

Figure 22c the FTIR spectrum of the Mon-ZnCuHF sample shows an absorbance band at 2102 cm^{-1} that is associated with the stretching vibration signal of the Fe^{III}-CN-M^{II} bond.

This band is closer to the band formed by the bonding of the CN⁻ group with Zn. However, a signal around 489 cm^{-1} that is associated with the stretching vibrations of the Zn-N bond is not observed. The absorption band shown at 441 cm^{-1} corresponds to the signal from the asymmetric Si-O-Si vibrations. The signals shown in Table 13 correspond to the IR spectrum of Mon-ZnHF that showing in Figure 22c.

Table 13 FTIR spectrum bands corresponding to Mon-ZnCuHF

Bands	υ (Fe^{II}-CN-M^{II})	υ (Zn-N)	υ (Fe-CN)	δ (Fe-CN)
Mon-ZnCuHF	2103 cm^{-1}	492 cm^{-1}	502 cm^{-1}	552 cm^{-1}

For Mon-FeHF sample, bands around 2080 cm^{-1} and 2168 cm^{-1} are associated with Fe^{II}-CN-Fe^{III} and Fe^{III}-CN-Fe^{III} bonds; they correspond to bending vibrations [62,123,124]. In addition three absorption bands around 654 cm^{-1}, 540 cm^{-1}, and 430 cm^{-1} assigned to the stretching vibrations of Fe-N, Fe-CN, and the twisting vibration of the Fe-CN bond [62,109]. The signals shown in Table 14 correspond to the IR spectrum of Mon-FeHF shown in Figure 22d.

Table 14 FTIR spectrum bands corresponding to Mon-FeHF

Bands	υ (Fe^{II} -CN-Fe^{III})	υ (Fe-N)	υ (Fe-CN)	δ (Fe-CN)
Mon-FeHF	2086 cm^{-1}	602 cm^{-1}	501 cm^{-1}	445 cm^{-1}

The matches between the absorption bands of the reported spectra and the spectra of the metal functionalized silica monolith samples after ferrocyanide contact impregnation lead to the conclusion that PBA formation took place *in situ* in the material.

4.2.2 Scanning Electron Microscopy

Figure 23 shows the SEM micrographies correlated with the silica monolith samples after the impregnation process. For the Mon-CuHF sample it is observed that the porosity of the material is maintained and agglomerations of metallic compounds were formed in the pores of the material (see Figure 23a).

The silica walls of the sample thin. Figure 23b shows the image be in agreement with the Mon-ZnHF sample, it is observed that there are also small agglomerations in the pores of the material, and that the silica walls are thicker and more compact. Figure 23c shows the image matching to the Mon-ZnCuF sample and shows that the porosity of the material is maintained, the silica walls are thinner and there is also the presence of metals between the pores.
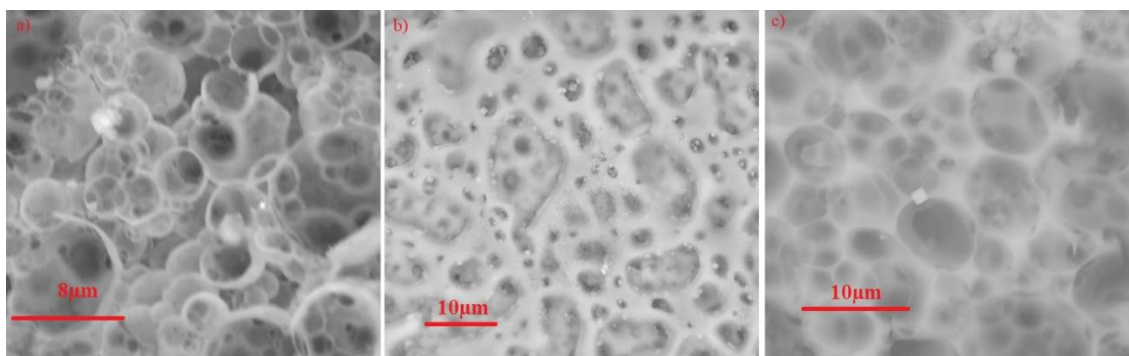
Figure 23 SEM images of metal functionalized silica monoliths after contact impregnation under controlled conditions: a) Mon-CuHF at 10Kx magnification, b) Mon-ZnHF at 5Kx magnification, c) Mon-ZnCuHF at 15Kx magnification.

The content of the particles agglomerations observed in the three images was determined from an EDX analysis with the same equipment, and detailed in Table 15(See in Appendix 2). Each of the samples presents higher percentage of oxygen concentration, followed by silicon and with concentrations between 0.06-3.28 for the metals. In addition, it is observed that in the Mon-CuHF sample the Fe and Sr signals could be shielding the signal for Cu.

Table 15 Atomic percent of metals by EDX analysis for metal functionalized silica monoliths after contact impregnation under controlled conditions.

Monoliths samples	Atomic percent of metals (%)	Atomic percent of silicon (%)	Atomic percent of oxygen (%)
Mon-CuHF	Sr: 1.03 Fe: 3.28 K: 1.39	19.65	74.65
Mon-ZnHF	Zn: 0.63 Fe: 0.92 K: 0.59	17.38	66.58
Mon-ZnCuHF	Cu:0.35 Zn: 1.91 Fe:0.81 K:0.06	21.82	52.15

Also, the EDX graphs can be found in the appendices.

The atomic percentage analysis of the samples allows confirming the composition of the silica monoliths functionalized with PBAs. At the same time this information supports the discussion of ATP-FTIR results.

4.2.3 X-Ray Powder Diffraction Spectroscopy

After performing the contact impregnation process, it is observed that the signals in the diffractogram do not change, and the silica peak remains present for all the monolith samples. The XRD patterns show a peak with the equivalent Bragg angle at $2\Theta= 21.1$ ° that correspond to amorphous signal of the material. According to the database of the equipment software (Revolutionary PDXL software), the other signals observed in each of the diffractograms in Figure 24 correspond to the sample holder of the equipment of aluminium. For this reason, it's not possible to determine the crystallinity size, crystal structure and phases of PBA.
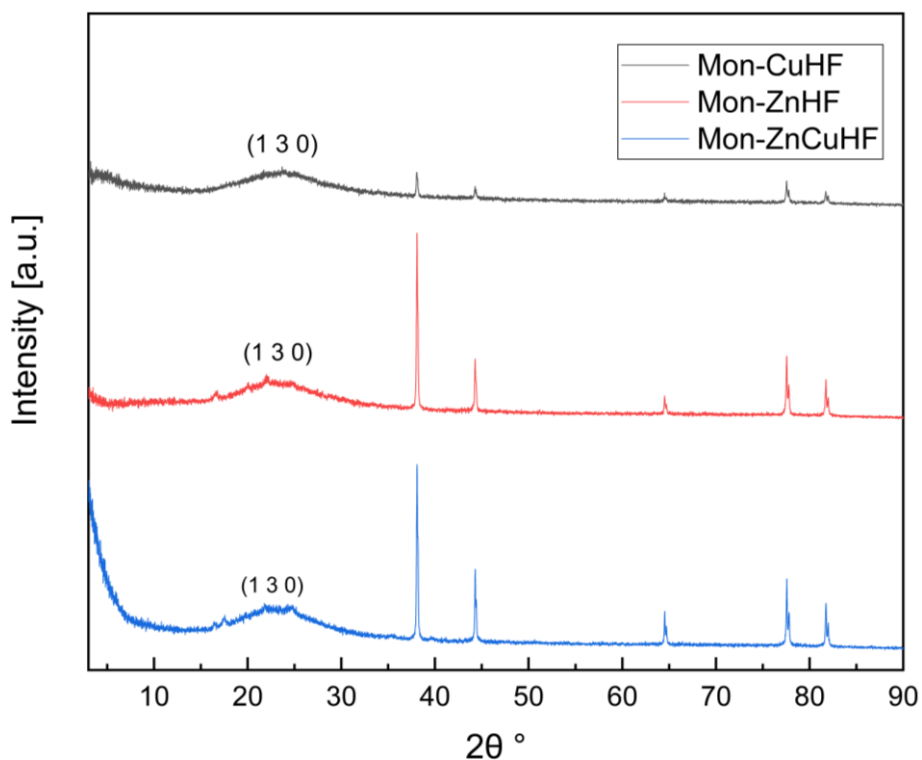
Figure 24 X-Ray Powder patterns spectra of metal functionalized silica monoliths after contact impregnation under controlled conditions. Black, red and blue correspond to Mon-CuHF, Mon-ZnHF, and Mon-ZnCuHF respectively.

4.2.4 Diffuse Reflectance UV-Vis Spectroscopy

For the analysis of the DRS-UV-Vis spectra, the formation of PBA's after the contact impregnation process was considered. Figure 25 shows the four absorption spectra (KM) corresponding to the Mon-CuHF, Mon-ZnHF, Mon-ZnCuHF and Mon-FeHF samples.
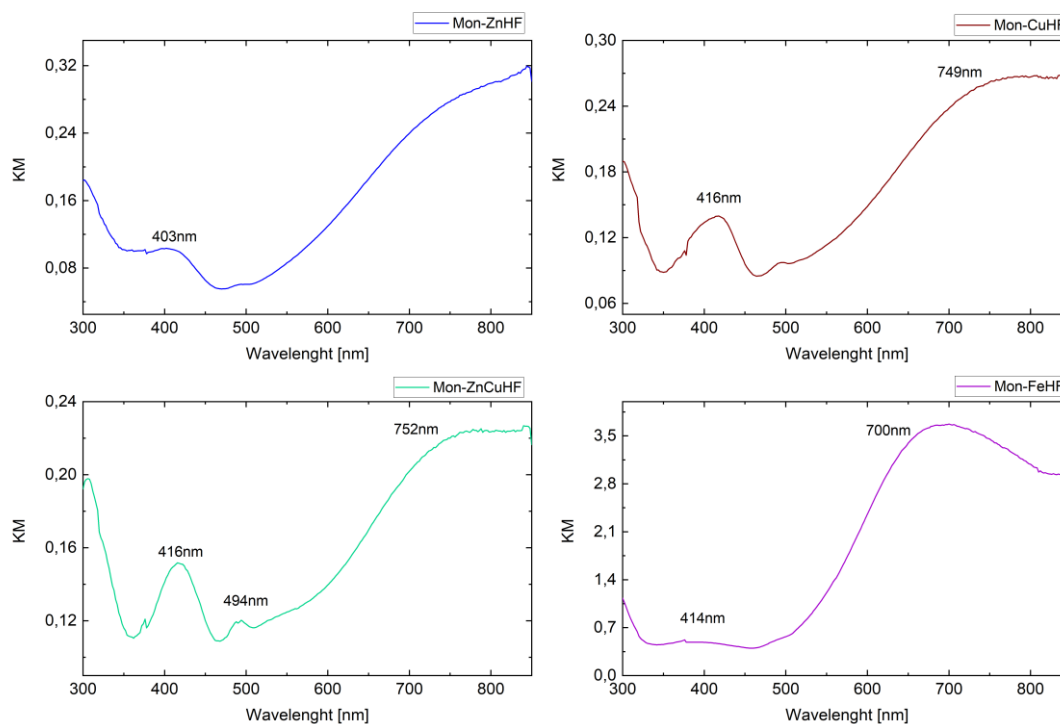

Figure 25 Diffuse Reflectance spectra of metal functionalized silica monoliths after contact impregnation under controlled conditions. a) Mon-CuHF,b)Mon-ZnHF,   c) Mon-ZnCuHF and d) Mon-FeHF

For the $K_4Fe(CN)_6$ compound, the bands observed in the 278-330 nm range are attributed specifically to the charge transfer between the Fe metal and the ligand[125]. In Figure 25 this signal is not clearly observed, town to the range used for the measurement, but it is expected that there are traces of the compound in the samples, since it was used in the contact impregnation process. Table 16 shows the observed and expected values for the absorption bands for these samples.

Table 16 Observed and expected absorption bands in the electronic spectrum metal functionalized silica monoliths after contact impregnation process.

Samples	Observed bands	Expected bands
Mon-ZnHF	403 nm	355 nm
Mon-CuHF	416 nm, 749 nm	377 nm, 550-700 nm
Mon-ZnCuHF	306 nm, 416 nm, 494 nm, 752 nm	355 nm, 550-700 nm
Mon-FeHF	414 nm, 700 nm	420 nm, 600-800 nm

In addition to the bands described in Table 16, the bands shown at wavelengths below 350 nm which can be attributed to the $K_4Fe(CN)_6$ signal. In the electronic spectrum of Zn (II), it is expected to find a signal around 355 nm, which is related to charge transfer between the metal center and CN^- ligands [62]. Since Zn does not show absorption bands because it has full d orbitals. This is of d^{10} type [62]. In addition, the spectrum shows a bathchromic shift that could be related to a change in the geometry of the complex and the interaction with the silica matrix [102,112].

For the Mon-CuHF sample, absorption bands were expected between 377 nm and in the range 550 nm to 700 nm when the copper ion is forming a pseudo octahedral structure [62,112,126]. This is possible due to the Janh Teller effect, which is produced by the affinity between the elements that constitute the network, since a distortion is generated by the change of counterion [13].

However, the signal observed in the spectrum presents a bathchromic shift that could be related by a change in the geometry of the complex from octahedral to square plane [112] as well as the interaction with the silica matrix.

Moreover, Cu (II) presents a d^9 low spin electronic configuration and it is bind to the nitrogen of the CN^- group which according to the spectroscopic series is a strong ligand. Two absorption bands of Cu(II) correspond to the transitions $^2B_{1g} \rightarrow {}^2A_{1g}$ and $^2B_{1g} \rightarrow {}^2E_{1g}$.

The absorption bands for Fe (III) are shown around 420 nm and in the 600-800 nm range in the absorption (K-M) spectrum and are related to charge transfer between the ligands and the matrix [111,115]. Fe (III) has a high spin electronic configuration, it is bind to the nitrogen of the ligands and shows no transitions in the electronic spectrum. However,

water molecules are also found in the silica matrix, so some of the oxygens could be bind to Fe (II), because there is higher affinity between of them.

The diffuse reflectance data were collected and transformed using the Kubelka-Munk function for calculated the band gap for samples (Appendix *5*). Table 17 shows the band gap value for the Mon-ZnHF, Mon-CuHF, Mon-ZnCuHF and Mon-FeHF monoliths.

Table 17 Band gap values for the metal funtionalized silica monoliths after impregnation process by contact

Monoliths samples funcionalized with PBA	Eg [eV]
Mon-ZnHF	2.6203
Mon-CuHF	2.6371
Mon-CuZnHF	2.5511
Mon-FeHF	1.3482

The band gap value for all the monolith samples in Table 17 correspond to the semiconductor energy value [62–64].

According to Rani and Shanker, 2018 [127] the band gap for PBA's is less than 2.0 eV and for PB it is ~1.15eV [128]. The band gap values obtained for the metal functionalized silica monoliths after impregnation process by contact are >2.0 eV for Zn, Cu, and CuZn (See Table 17). The silica matrix and metal oxides are mixed with the PBA's functionalized silica monoliths. They increase the band gap value of silica monoliths functionalized with PBAs. By having different types of metals within the silica matrix, the monolith can be considered an extrinsic semiconductor [93].

4.2.5 Magnetic Susceptibility Balance

Samples of Mon-ZnHF, Mon-CuHF, Mon-ZnCuHF and Mon-FeHF monoliths were characterized by calculating the mass susceptibility value. All samples were analyzed at

room temperature and pulverized. The magnetic susceptibility values for each of the monoliths are listed in Table 18.

Table 18 Magnetic susceptibility measurements of metal functionalized silica monoliths after contact impregnation under controlled conditions.

Monoliths samples funcionalized with PBA	Mass Magnetic Susceptibility measurement (Bm)	Magnetic properties
Mon-ZnHF	$6,63 \times 10^{-8}$	Paramagnetic associated to Fe (III)
Mon-CuHF	$1,28 \times 10^{-6}$	Paramagnetic
Mon-CuZnHF	$4,07 \times 10^{-7}$	Paramagnetic
Mon-FeHF	1.89×10^{-12}	Antiferromagnetic coupling

From the magnetic susceptibility calculations, it was obtained that all the values are greater than zero $(X_g > 0)$ so it is inferred that the four samples have paramagnetic character. Figures 26-28, show the electronic distribution of the d orbitals for the metals that could be coordinating with the nitrogen in the unit cell of the PBA's.

Figure 26 shows the schematic representation of the possible structure of d orbital for Fe (II). $[Fe^{II}(CN)_6]$ shows diamagnetic character, since the Fe (II) metal center has a low spin d^6 (s=0) electronic configuration. The theoretical effective magnetic moment (μ_{eff}^{theo}) for this metal is zero [13,64,129,130].
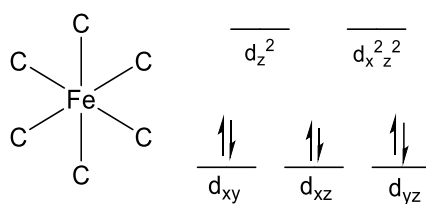
Figure 26 Schematic representation of the possible structure of d orbital for Fe (II).

The metal center Zn (II) has all d orbitals filled (d^{10}, s=0) so the compound is expected to be diamagnetic (Figure 27). In addition, the geometry of Zn is expected to be tetrahedral, but the possibility of an octahedral geometry is not ruled out by the bathchromic shift observed in the DRS-UV-Vis absorption spectra (K-M). For this metal center the μ_{eff}^{theo} is equal to zero [13,64].
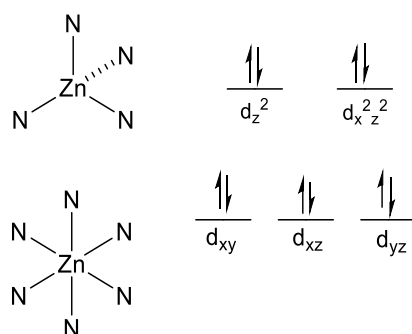
Figure 27 Schematic representation of the possible structure of d orbital for Zn (II).

The Cu (II) metal center is paramagnetic, since it has an electronic configuration d^9, and s=1/2 (Figure 28). The expected geometry for this metal is octahedral, but the bathchromic shift observed in the DRS-UV-Vis absorption spectra (K-M) can be related to a change in the geometry to squared plane. The μ_{eff}^{theo} for this metal center is equal to 1.73BM [13,102,129].
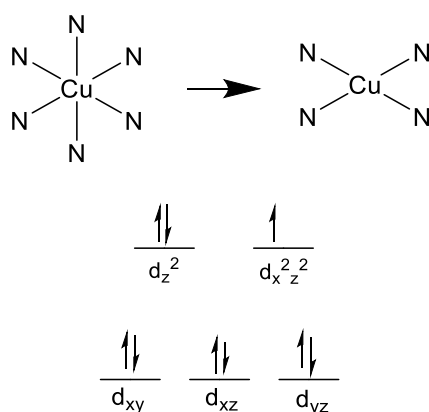
Figure 28 Schematic representation of the possible structure of d orbital for Cu (II).

The Fe (III) metal center has an electronic distribution d^5 high spin, (s=5/2), with paramagnetic character. An octahedral geometry is expected for this metal center, and the value for μ_{eff}^{theo} is equal to 5.8 BM [13,130].
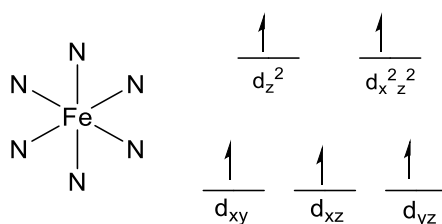
Figure 29 Schematic representation of the possible structure of d orbital for Fe.

Therefore, to Mon-ZnHF was expected a magnetic susceptibility measurement of less than zero because its diamagnetic character. However, the measurement obtained experimentally indicates that this sample is paramagnetic. This is possible due to that inside the monolith there are Fe particles of the potassium ferrocyanide used in the impregnation process. This is confirmed by EDX analysis since in the Mon-ZnHF there is 0.92 of iron while for Zn there is 0.63 of atomic percent (Table 15). In addition, this paramagnetism can also be related to the PBA's formation within the monolith.

For the Mon-CuHF and Mon-ZnCuHF samples this magnetic property is shown as the sum of Cu and Fe paramagnetism. For the Mon-FeHF sample a very small value is obtained for the magnetic susceptibility measurement, this is associated to the antiferromagnetic coupling type paramagnetism own to having the iron redox pair (Fe^{2+}/Fe^{3+}) inside the monolith structure[131]. This magnetic behavior is considered because Fe(II) is inert and it is very rare that it changes its oxidation state [130].

In order to explain the magnetic properties of the solid dilutions of silica and to relate it to the pure complex compounds, a calibration curve was elaborated with known complex compounds. Despite obtaining a high ratio coefficient R^2 = 0,9808, the values were not so good, however its use for future measurements is not ruled out (Appendix 6).

After characterization of the monoliths that underwent the contact ferrocyanide impregnation process under controlled conditions, it was determined that the compound synthesized in situ in the monolith is a coordination complex. From its properties it can be assumed that the complex is a PBA.

Furthermore, after analyzing the band gap together with the magnetic susceptibility measurements for the samples Mon-ZnHF, Mon-CuHF, Mon-ZnCuHF and Mon-FeHF, the study of the applications of this material in the field of intrinsic semiconductors and for energy storage is considered [132,133].

4.3 Impregnation of Fe-functionalized monoliths by laminar flow and determination of cyanides ions.

In this section, it evaluates the formation of PBA's into Fe(II-III) functionalized silica monoliths after heavy metal and cyanide impregnation from a laminar flow of synthetic water. For this purpose, the iron-functionalized monoliths were characterized after being used as microreactors.

Also, for this impregnation the synthesis ratios were changed, it was proposed to triple them. This is because when the SEM micrographs of the previous samples were analyzed, it was observed that the silica walls are thin and with a disordered architecture, so the monoliths tend to break easily. However, for this experiment it is necessary to get a higher strength and solid matrix because it must resist the hydraulic pressure of the water flow, for the experiment.

Table 19 describes the parameters of the monoliths used for the experiment.

Table 19 Parameters of monoliths for using as microreactors

Monolith samples	Diameter [cm]	Length [cm]	Initial color	Final Color
SFMon-FeIII (1)	1	2.7	Yellowish	Gray
SFMon-FeIII (2)	0.9	2.8	Yellowish	Beige
SFMon-FeIII-3T (1)	1	2.5	Yellowish	Beige
SFMon-FeIII-3T (2)	0.9	2.7	yellowish	Greenish
SFMon-FeII (1)	1	3.3	Orange (pastel tones)	Beige
SFMon-FeII (2)	1	3.2	Orange (pastel tones)	Beige
SFMon-FeII-3T (1)	0.9	2.4	Brown	Beige
SFMon-FeII-3T (2)	0.8	2.4	Brown	Yellowish

The synthesis of these Fe(II-III) functionalized monoliths was carried out with two different ratios. The SFMon-FeIII (1)-(2) and SFMon-FeII (1)-(2) samples have a 1:1 TEOS:P123 ratio. While the SFMon-FeIII-3T (1)-(2) and SFMon-FeII-3T (1)-(2) samples have a 3:1 TEOS:P123 ratio.

The range of diameter and length of the monoliths is between 0.8-1cm and 2.4-3.3cm respectively. The measurements of the monoliths are very close without matter the proportional ratio.

After impregnation, a change in the color of the monoliths was observed because a chemical reaction occurred. The color change is detailed in Table 19 and can be observed in Figures 30-31.
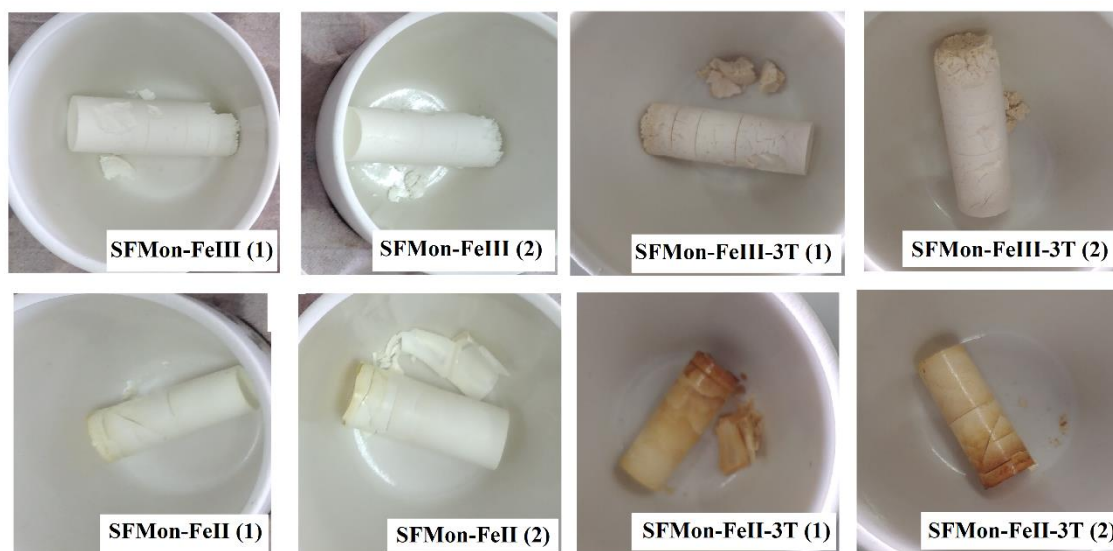
Figure 30 Pyrolyzed Fe(II-III)-functionalized silica monoliths.
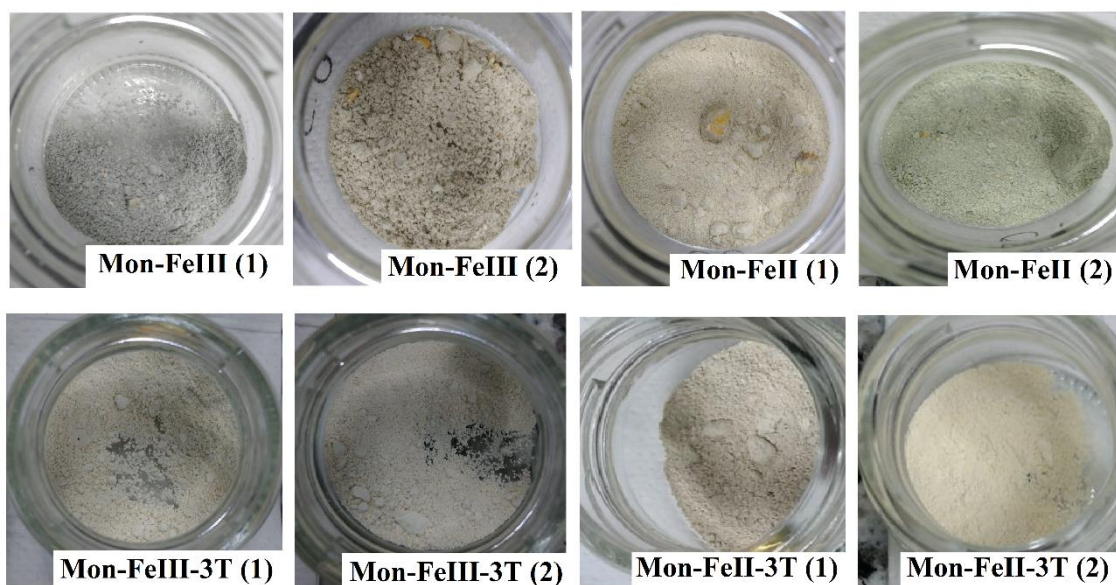
Figure 31 Pulverized samples of Fe(II-III)-functionalized silica monoliths after heavy metal and cyanide impregnation from a laminar flow of synthetic water.

4.2.1 Attenuated Total Reflection FTIR Spectroscopy

FTIR spectra of the Mon-FeIII, MonFeIII-3T, MonFeII, and MonFeII-3T are presented in the Figure 32.
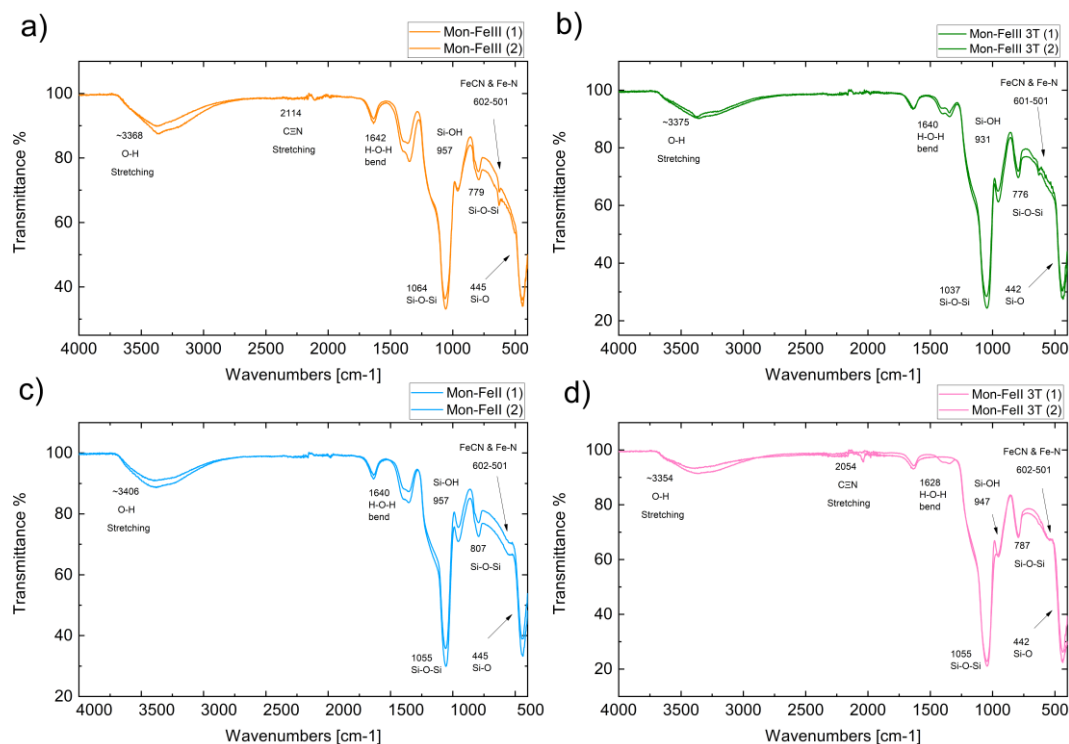
Figure 32 Infrared spectrum of metal functionalized silica monoliths after impregnation by laminar flow. a) Orange IR spectrum of FeIII monoliths, b) Green IR spectrum of FeIII 3T monoliths, c) Light blue IR spectrum of FeII monoliths d) Pink IR spectrum of FeII 3T monoliths.

In all spectra the signals corresponding to the stretching and bending vibrations of silica, water like above mentioned in the last section. In spectra a and d of Figure 32, peaks corresponding to the C≡N bond are observed with very low intensity at wavenumber values of ~2100 cm^{-1}. So PBA's may have formed within the structure of the MonFeIII and MonFeII-3T samples but also other compounds such as cyanide salts, complex compounds with water ligand, and oxides [30].

For spectrum a in Figure 32 it is observed that the C≡N bond is found at 2114 cm^{-1} which means that a Fe^{II}-CN-M^{III} type PBA may be present since the ban. For this sample is found between 2110-2145 cm^{-1} [116,122]. While for spectrum d in Figure 32, a Fe^{II}-CN-M^{II} type PBA is expected [116,122].

For spectra b and c in Figure 32 the possible formation of PBA's in the material is not ruled out because the bands appearing between 602-501 cm^{-1} are attributed to the bending vibrations of Fe with CN^{-}. However, further characterization tests are necessary to ensure the formation of PBAs.

4.3.2 Scanning Electron Microscopy

The SEM characterization for the monoliths used in the laminar flow impregnation are shown in Figure 33 and Figure 34.
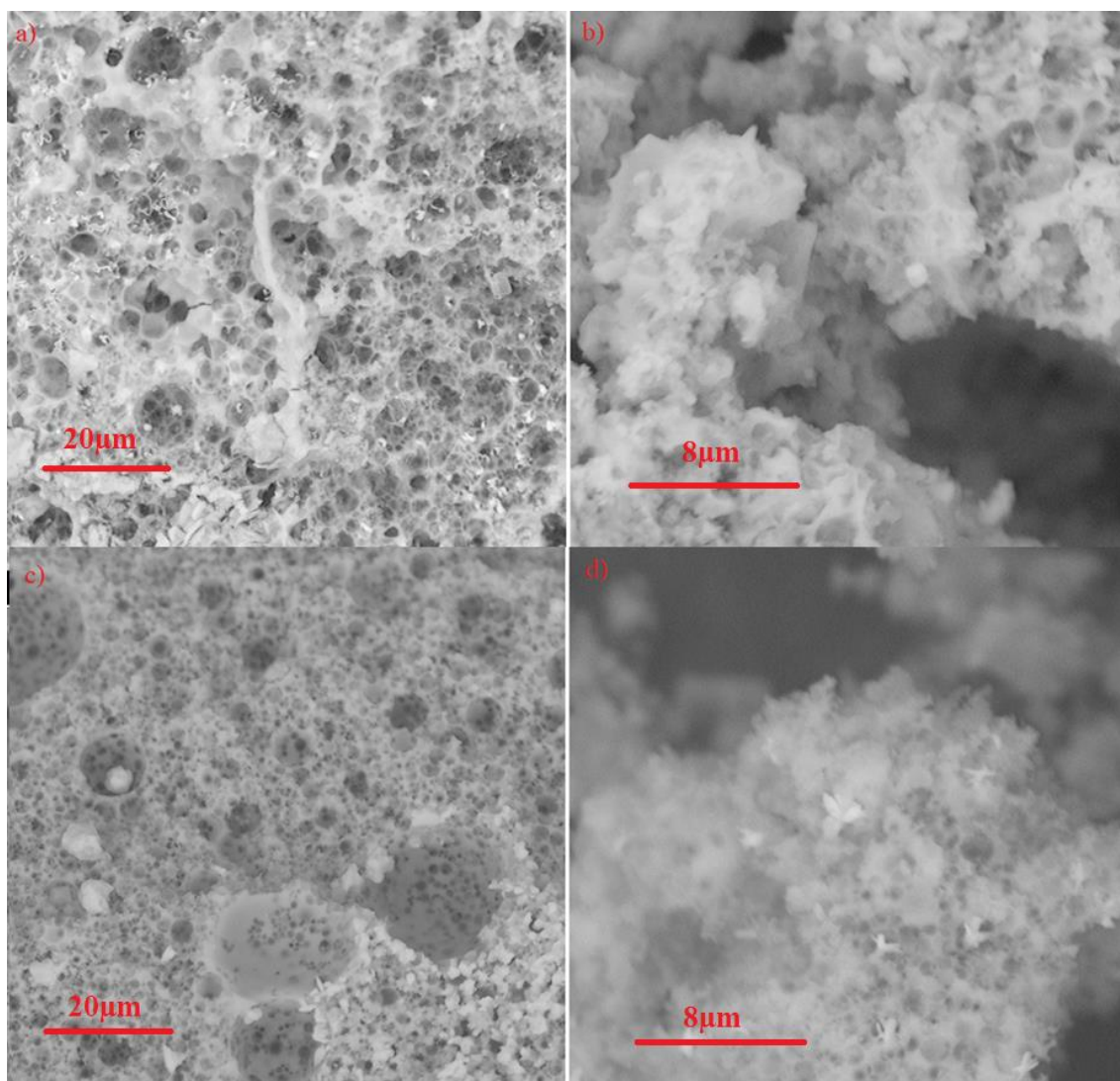
Figure 33 SEM images of metal functionalized silica monoliths after impregnation by laminar flow: a) Mon-FeIII (1) at 3Kx magnification, b) Mon-FeIII (2) at 10Kx magnification, c) Mon-FeIII-3T (1) at 3Kx magnification, d) Mon-FeIII-3T (2) at 10Kx magnification.

The samples show a morphology composed of dispersed particles forming agglomerates in the pores. In the case that PBA's formation has occurred, it is expected to observe cubic structures on the surface of the samples [120]. Most probably, some other cyanide compounds were formed rather than PBA's as it was previously shown when a mixture of salts (Cu-Zn) was used to obtain PBA. Apparently it difficult its formation because of kinetic rate for Cu-PBA formation differs from that of Zn-PBA [134].

EDX analysis made possible to determine the atomic percentage of the different elements that interact in the monoliths (see Appendix 3). Table 20 shows that the percentage of oxygen is the most abundant. In addition, it can be observed that the percentage of metals for the laminar flow impregnation process is higher than that of the contact impregnation process.

Table 20 Atomic percent of metals by EDX analysis of iron III funtionalized monoliths.

Monolith samples	Atomic percent of metals (%)	Atomic percent of carbon (%)	Atomic percent of nitrogen (%)	Atomic percent of silicon (%)	Atomic percent of oxygen (%)
Mon-FeIII (1)	Cu: 21.56 Al: 1.62 Fe: 2.57 Na: 3.02	33.01	17.67	4.14	16.42
Mon-FeIII (2)	Cu: 11.57 Na: 3.87 Fe: 3.09 Zn: 0.71	9.12	13.52	6.66	50.23
Mon-FeIII-3T (1)	Cu: 4.29 Na: 8.36 Zn: 2.21 Fe: 0.25 Al: 0.38	16.50	10.31	4.02	30.34
Mon-FeIII-3T (2)	Cu: 13.08 Na: 2.10 Fe: 0.89 Al: 2.74	34.81	23.09	1.81	21.48

When comparing the images in Figure 33 and Figure 34, differences in the ordering of the porosity of the material are observed since the samples corresponding to FeII 3T shown in Figure 34 look more compact. However, it can be seen that the behavior of the matrix is the same for any of the iron ions.
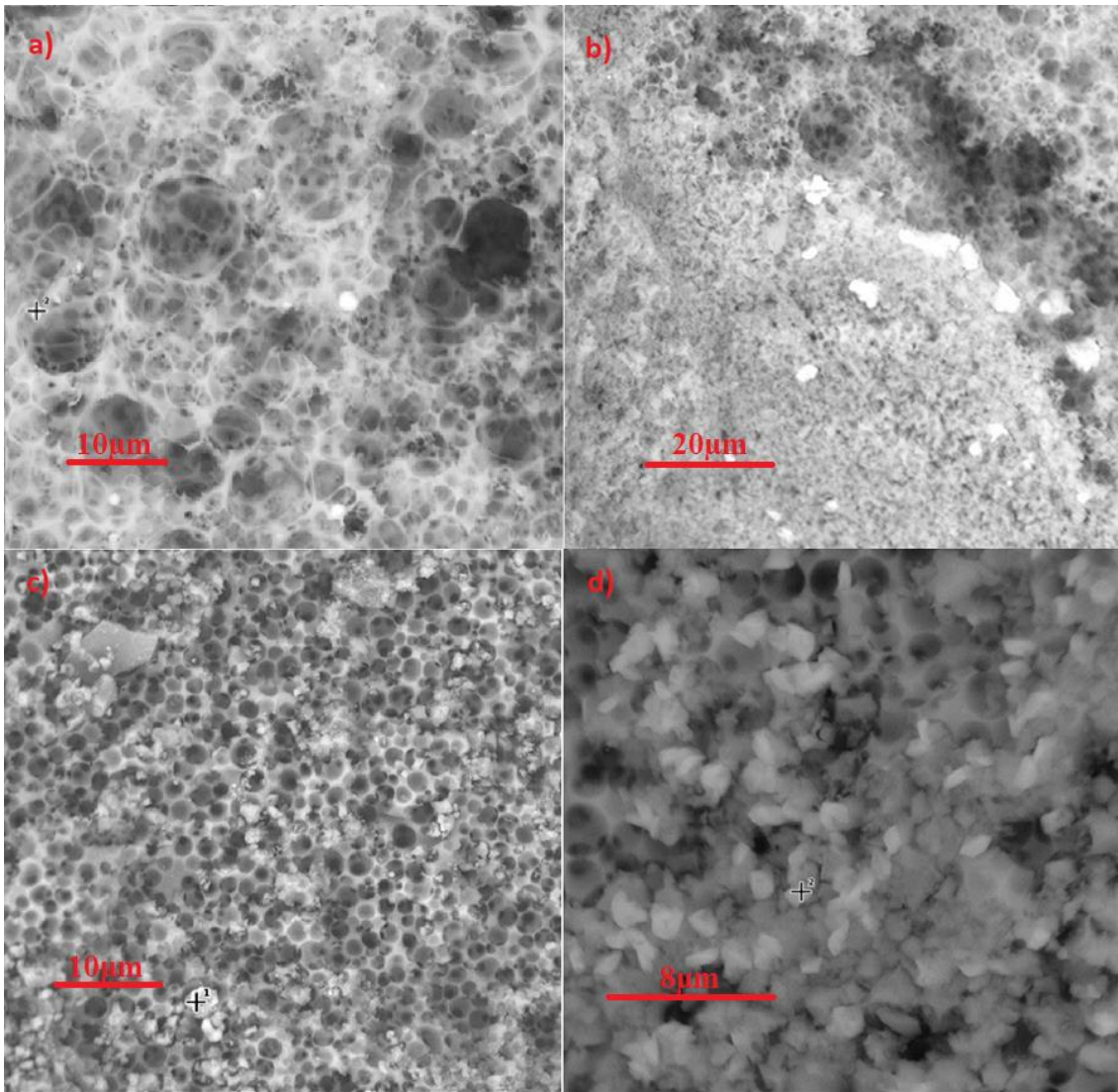
Figure 34 SEM images of functionalized monoliths by laminar flow. a and b items correspond to Mon-FeII (1) at 3Kx magnification, b) Mon-FeII (2) at 5Kx magnification, c) Mon-FeII-3T (1) at 5Kx magnification, d) Mon-FeII-3T (2) at 5Kx magnifications.

In the SEM image corresponding to the MonFeII (1) and (2) samples the bright spots are related to metal agglomerations, this was determined by EDX analysis and the atomic percentages found are described in Table 21. In the SEM images corresponding to the MonFeII-3T samples (1) and (2) can be observed that the porous structure is more compact and with more defined porous cavities. It can also be observed that there are agglomerations in the pores, which according to the SEM analysis correspond to metals as well. It is important to mention that in the FeII-3T samples the walls of the porous

surface of the material have greater thickness, which could improve the mechanical properties of the material, and the granules are coarser.

Table 21 Atomic percent of metals by EDX analysis of iron II funtionalized monoliths.

Monolith Samples	Atomic percent of metals (%)	Atomic percent of carbon (%)	Atomic percent of nitrogen (%)	Atomic percent of silicon (%)	Atomic percent of oxygen (%)
Mon-FeII (1)	Cu: 26.62 Zn: 2.63	13.93	23.31	19.40	25.91
Mon-FeII (2)	Cu:19.37 Zn: 1.40 Na: 4.76	13.93	12.82	23.10	38.56
Mon-FeII-3T (1)	Cu: 0.71 Zn: 0.76 Fe: 7.30 Na: 2.56	11.78	9.6	11.78	57.33
Mon-FeII-3T (2)	Fe: 4.06 Na: 1.84 Cu: 1.23 Zn: 1.17	11.49	11.68	16.35	51.62

From Table 21 it can be seen that Zn, and Cu are present in all particle agglomerations on the surfaces. Moreover, the signal for C-N group is present, so there is a possibility that a cyanide salt has been formed or trapped in the matrix of the functionalized monolith. EDX spectra are shown in the (see Appendix 4).

The percentage of metals, carbon, and nitrogen for MonFe(II-III) 3T monoliths is lower than for MonFe(II-III) because of morphology differences in monoliths.

4.2.3 X-Ray Powder Diffraction Spectroscopy

The samples were pulverized for XRD analysis. Diffractograms of the iron II and iron III funtionalized silica monoliths are showing in Figure 35.
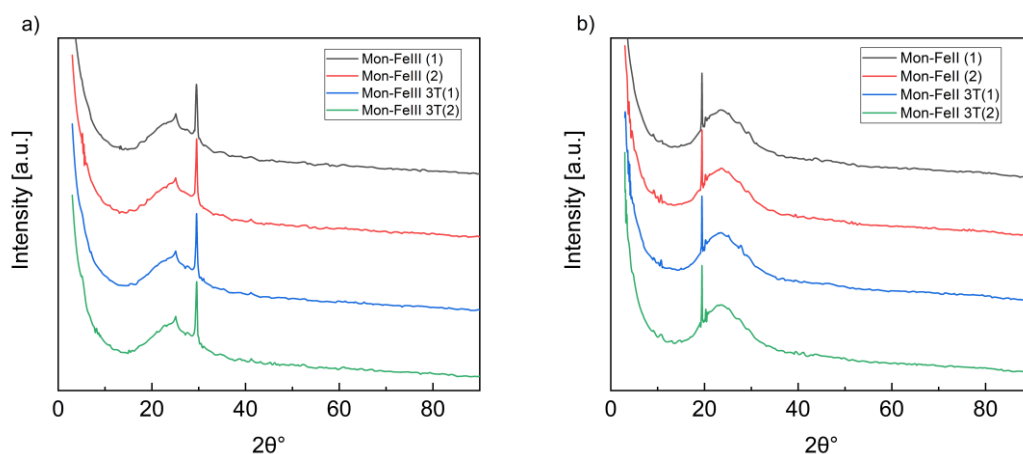
Figure 35 X-Ray Powder Diffraction spectra of metal functionalized silica monoliths after impregnation by laminar flow. Diffractogram of color black and red correspond to the samples of FeIII and FeII and the diffractograms of color blue and green correspond to FeIII 3T and FeII 3T for each plot.

The diffractograms of the Figure 35a correspond to the signals of °2Θ= 25.09 ° with miller indices of (3 4 2) and °2Θ= 29.55 ° with miller indices of (7 0 -1). These values were obtained from the match from peak matches with chart 00-702-3095. While for the digractograms in Figure 35b correspond to signals of °2Θ= 19.51 ° and °2Θ= 23.08 ° with miller indices (4 3 -2) and (5 0 3) respectively. The 00-720-6030 chart was used to verify peak matches.

The XRD patterns show an important peak for this characterization in the range of °2Θ= 23 ° to 25 ° in the equivalent Bragg. This indicates that the material is amorphous, as well as for the rest of the samples previously presented. The peak that appear next to the characteristic silica peak shows that the silica of material became crystalline according to Deshmukl, 2012 [135].

However, the peak that appears next to the silica signal in diffractograms a) and b) indicates that a more ordered or defined structure is present. However, one cannot say that they correspond to the PBA formation or to other cyanide compound. The expected peaks for PBA is highlighted in the Figure 36 taken from Sommer-Márquez et. al., 2016 [83].
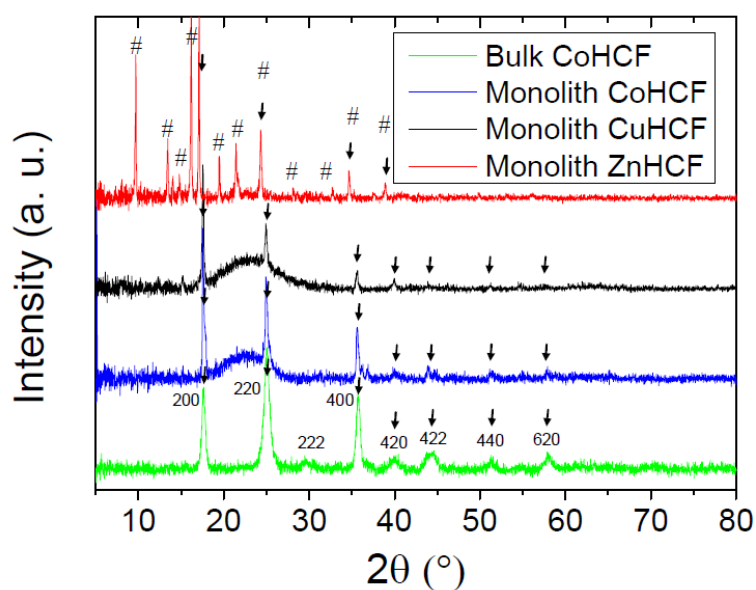
Figure 36 XRD pattern for bulk CoHCF and monoliths CuHCF, ZnHCF and CoHCF. Taken from Sommer-Márquez, 2016 [83].

After comparing the spectrum reported by Sommer-Marquez in 2016 [83] and the spectrum obtained for the eight Fe(II-III) functionalized silica monolith samples, no similarities were found. Therefore, it is again concluded that the metal:silica ratio is too small to be detected by the Rigaku MiniFlex 600 equipment.

4.2.4 Diffuse Reflectance UV-Vis Spectroscopy

The electronic spectra for the Fe (III) and Fe (II) functionalized silica monolith samples (MonFeIII(1-2), MonFeIII-3T(1-2), MonFeII(1-2), MonFeII 3T (1-2)) are shown in Figure 37.

Figure 37a-b shows a single absorption band at 436 nm and 434 nm. These absorption bands can be related with the presence of Cu or FeO/SiO2. Although the signal for the bands is very close, the relationship with Cu can be ruled out because the band around 780 nm is absent [62,125].
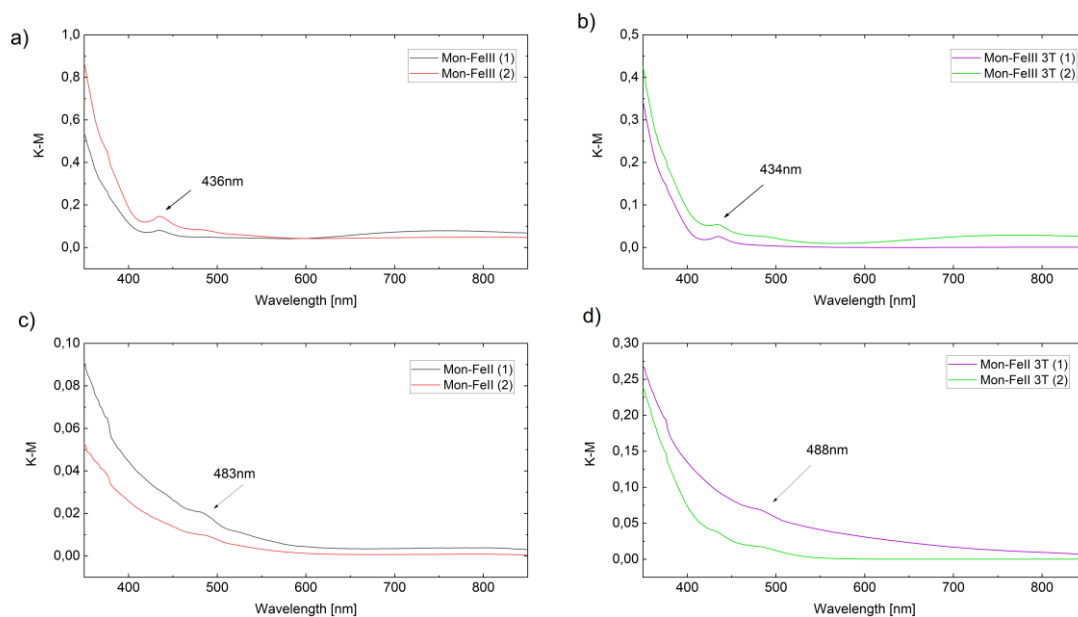
Figure 37 DRS-UV-Vis spectra of iron III and iron II functionalized silica monoliths after impregnation by laminar flow. a)MonFeIII(1-2) b) MonFeIII-3T(1-2), c)MonFeII(1-2), d)MonFeII 3T (1-2).

Also, Figure 37c-d shows a single broad absorption band at 483 nm and 488 nm respectively. They have low intensity and is located on the slope of the spectrum. This signal may correspond to Fe functionalized in the silica matrix (FeO/SiO_2) since the electronic spectrum is very similar to the electromagnetic spectrum for the Mon-Fe pyrolyzed monolith (Figure 20d) and the value is similar to the reported literature [136].

Whole absorptions bands of DRS-UV-Vis spectra correspond to Fe. Therefore, they can be related with the funtionalized iron II and iron III on the matrix or the signal to ligand-metal charge between oxygen and iron.

4.2.5 Magnetic Susceptibility Balance

The magnetic properties of the iron II and iron III functionalized monoliths were analyzed through magnetic balance measurements. The values for the mass magnetic susceptibility and the experimental effective magnetic moment for Mon-FeIII (1-2), Mon-FeIII 3T(1-2), Mon-FeII (1-2), Mon-FeII3T (1-2) are shown in Table 22.

Table 22 Magnetic susceptibility measurements of metal functionalized silica monoliths after impregnation by laminar flow.

Monolith Samples	Mass magnetic susceptibility Xg $[10^{-6}]$ emu.mol^{-1}	Magnetic properties
Mon-FeIII (1)	1,2557	Paramagnetic
Mon-FeIII (2)	4,4798	Paramagnetic
Mon-FeIII-3T (1)	1,9938	Paramagnetic
Mon-FeIII-3T (2)	2,9985	Paramagnetic
Mon-FeII (1)	1,4956	Paramagnetic
Mon-FeII (2)	1,4204	Paramagnetic
Mon-FeII-3T (1)	1,4151	Paramagnetic
Mon-FeII-3T (2)	3,8050	Paramagnetic

Table 22 show Xg values are greater than zero, so the samples are paramagnetic. For iron (II) and iron (III) have a d^6 and d^5 electronic configuration respectively. The possible electronic distribution for of iron (II) is high spin and to iron (III) high spin or low spin. These values are in magnitudes of 10^{-6} so that an antiferromagnetic coupling behavior can be ruled out. The main reason is due to the fact that in this experimental process no extra Fe dilution was added to the silica matrix. Then it is concluded that the compound formed after laminar flow impregnation inside the iron-functionalized monolith is paramagnetic.

4.3.6 Determination of cyanide concentration (Preliminary study)

The aim of this experiment was to analyze the use of Fe(II-III) functionalized silica monoliths as an environmental mitigation agent for water. Figure 38 shows the laminar flow system and how the monoliths were coated with plastic to form the micro-reactor.

Figure 38 Flux system representation

A plastic cladding was used to place the monolith samples inside a laminar flow system (Figure 38). The color change in the monoliths after the passage of emulated wastewater indicates that a reaction occurred in the wastewater (see Figure 39) .
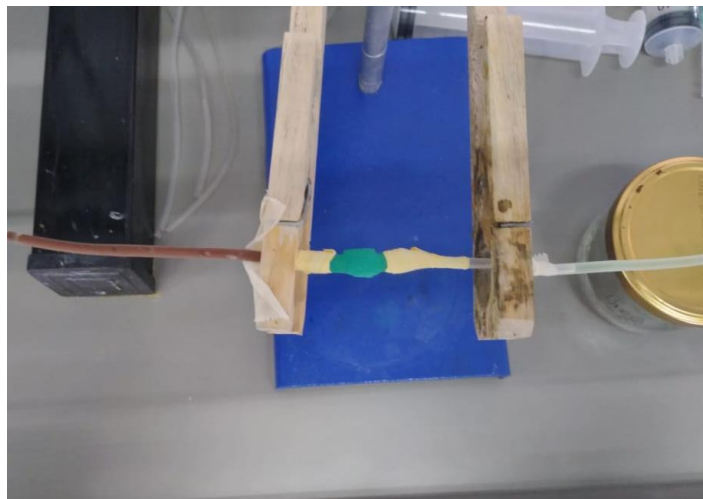
Figure 39 Synthetic water flow through the cladding monolith.

Cyanide determination was performed by a volumetric method [1,15,137]. From aliquots emulating mining wastewater taken downstream from the line (see Appendix 8). A calibration curve with $R^2 = 0.9972$, an instrumental error of 0.05 and a lineal equation y = 13.604x + 0.2315 was used to determine the concentration of the test samples. Where "x" corresponds to the concentration of the solution and "y" to the volume required to reach the end point.

The initial concentration of the emulated wastewater was 1 M, and the calibration curve was used to determine the final concentration downstream. It is important to mention that there was no recirculation of the water flow through the monolith. It was passed only once. Table 23 shows the final concentration for the 1 M cyanide flow after passing

through the monoliths Mon-FeIII (1)-(2), Mon-FeIII 3T(1)-(2), Mon-FeII (1)-(2), Mon-FeII3T (1-2).

Table 23 Final concentration of the emulated water flow for each of the monolith samples.

Monoliths samples	Final concentration [M]	Percentage of cyanide reduced (%)
Mon-FeIII (1)	0,534	46.590
Mon-FeIII (2)	0,644	35.564
Mon-FeIII-3T (1)	0,696	30.419
Mon-FeIII-3T (2)	0,733	36.743
Mon-FeII (1)	0,571	42.914
Mon-FeII (2)	0,527	47.325
Mon-FeII-3T (1)	0,806	19.392
Mon-FeII-3T (2)	0,747	25.273

Table 23 shows the final concentrations for the emulated water flow, it is observed that the cyanide concentration decreased for all samples. From this, possible reasons for the decrease in cyanide concentration are proposed. Furthermore, it is observed that the reduction of cyanide concentration after passing through the Fe(II-III)-functionalized monoliths is at least 30%. It is important to mention that this reduction was obtained after the synthetic water flow passed through the monoliths only once.

From these results it is said that heavy metals and cyanide found in the synthetic water stream formed *in situ* PBA's on the Fe(II-III) functionalized silica monoliths or other cyanocompounds. In addition, to confirm this premise, a further test was performed on a silica monolith without iron functionalization in its structure (Mon-Blank). The results indicated that the cyanide concentration was kept constant so there was no adsorption of CN- by the Mon-Blank.

Summary

ATR-FTIR

FTIR spectra allowed to verify the release of the mesoporosity of the silica skeleton after the pyrolyzation process. The functionalization of the silica monoliths with the metals was also verified. For second stage of the experiment, allowed the first approach to identify the compounds that formed in the silica structure after impregnating potassium ferrocyanide and by laminar flow with emulated residual water. In the case of the first impregnation, they were PBA. It is essential to mention that although peaks with high intensity were not obtained for the second impregnation, the formation of complexes can be considered for the other bands that appear below 700nm.

SEM-EDX

In SEM micrographs, the distribution of macroporosity within the monolith was observed. It observed thin walls that may affect the mechanics properties of monoliths. The presence of metals (Cu, Zn, Fe) functionalized in the structure was determined through EDX analysis with atomic percentages less than 4. In addition, in the impregnation process it was observed that there are concentrations of C and N in the structure, so there are probabilities that the CN- group is interacting with the metals in the matrix.

XRD

The XRD analysis showed that the structure is amorphous but did not indicate the presence of PBA's in the silica structure since the peaks obtained correspond to the aluminum sample holder of the equipment. This is because the Metal/Si ratio is very low and the detection limit of the equipment is high and not very sensitive to lower concentrations.

DRS-UV-Vis

The DRS-UV-Vis electronic spectra allowed us to determine the oxidation states for Fe, and Cu, along with the geometries of the compounds. However, a bathochromic shift is observed for the absorption bands, for the first analysis between the pyrolyzed and nonpyrolyzed samples is related to a change in the polarity of the solvent that is forming the aqueous phase. While for impregnations the bathochromic shift observed can be related with a change in geometry $O_h \rightarrow T_d$.

Magnetic susceptibility measurements

When calculating the magnetic susceptibility and effective magnetic moment, the expected values for the PBAs were found to be influenced by two main aspects. The first one corresponds to the diamagnetic effect of the silica, and the atomic percentage of the metals which EDX determined. These two factors can invert the magnetic properties, such is the case for the Mon-ZnFH sample, which is paramagnetic.

Chapter 5

5. Conclusion and future work

In conclusion, the synthesis of metal-functionalized silica monoliths with hierarchical structure was achieved. This was verified by the different spectroscopic and morphological characterization tests. It was also possible to follow up the structural changes in the silica matrix after the pyrolyzation process. The influence of the different reagents used for the synthesis of the functionalized silica monoliths on the spectra was also observed.

The characterization techniques ATP-FTIR, SEM-EDX, DRS-UV-Vis, and magnetic susceptibility measurements allowed to verify the presence of Prussian blue analogues in the porous structure of the material after ferrocyanide impregnation by contact under controlled conditions. It was also determined that the silica monoliths impregnated with ferrocyanide have paramagnetic properties and their band gap allows them to be classified as extrinsic semiconductors. Likewise, the monoliths functionalized with iron II and iron III that underwent a laminar flow impregnation process were characterized. From the analyses it can be said that there was a reaction within the material used as microreactor, but the compound is not necessarily a PBA, for which more characterization techniques are needed.

Unfortunately, the XRD technique only to confirm the amorphous crystallinity of monoliths samples.

The preliminary study of cyanide concentration reduction in mining wastewater was positive, since the silica monoliths functionalized with iron II and iron III reduced the initial concentration of the flux by at least 30%, with a single step.

As future work, it would be interesting to investigate the magnetic properties of PBAs within the silica matrix with possible applications in energy storage or batteries.

Bibliography

(1) Anning, C.; Wang, J.; Chen, P.; Batmunkh, I.; Lyu, X. Determination and Detoxification of Cyanide in Gold Mine Tailings: A Review. *Waste Manag. Res.* **2019**, *37* (11), 1117–1126. https://doi.org/10.1177/0734242X19876691.

(2) Botz, M. M.; Mudder, T. I.; Akcil, A. U. *Cyanide Treatment*; Elsevier B.V., 2016. https://doi.org/10.1016/b978-0-444-63658-4.00035-9.

(3) Jaszczak, E.; Polkowska, Ż.; Narkowicz, S.; Namieśnik, J. Cyanides in the Environment—Analysis—Problems and Challenges. *Environ. Sci. Pollut. Res.* **2017**, *24* (19), 15929–15948. https://doi.org/10.1007/s11356-017-9081-7.

(4) Callis, C. F. The Structure of the Heavy Metal Cyanides. *J. Chem. Educ.* **1948**, 150–156. https://doi.org/10.1021/ed025p150.

(5) Nakao, Y. Metal-Mediated C-CN Bond Activation in Organic Synthesis. *Chem. Rev.* **2021**, *121* (1), 327–344. https://doi.org/10.1021/acs.chemrev.0c00301.

(6) Fleming, F. F.; Wang, Q. Unsaturated Nitriles: Conjugate Additions of Carbon Nucleophiles to a Recalcitrant Class of Acceptors. *Chem. Rev.* **2003**, *103* (5), 2035–2077. https://doi.org/10.1021/cr020045d.

(7) Ferris, J.; Ryan, T.; Wos, J.; Lobo, A.; Donner, B. Biomolecules from Hcn*. **1974**, *5* (1973), 153–157.

(8) Fleming, F. F. Nitrile-Containing Natural Products. **1999**, 597–606.

(9) Bhagavan, N. V.; Ha, C.-E.; Bhagavan, N. V.; Ha, C.-E. Chapter 26 – Hemoglobin. *Essentials Med. Biochem.* **2015**, No. Chapter 6, 489–509. https://doi.org/10.1016/B978-0-12-416687-5.00026-9.

(10) Piernas Muñoz, M. J.; Castillo Martínez, E. Prussian Blue and Its Analogues. Structure, Characterization and Applications. *SpringerBriefs Appl. Sci. Technol.* **2018**, 9–22. https://doi.org/10.1007/978-3-319-91488-6_2.

(11) Hahn, T. *International Tables for Crystalography*, Fifth.; Penfold, D., Dacombe, S., Barnes, N., Ashcroft, J., Eds.; Springer US: Norwell, 2005; Vol. 148.

(12) Hanusa, T. P. Cyanide Complexes of the Transition MetalsBased in Part on the Article Cyanide Complexes of the Transition Metals by Timothy P. Hanusa & David J. Burkey Which Appeared in the Encyclopedia of Inorganic Chemistry, First Edition . . *Encycl. Inorg. Chem.* **2006**, 1–11. https://doi.org/10.1002/0470862106.ia059.

(13) Huheey, J.; Keiter, E.; Keiter, R. *Inorganic Chemistry_ Principles of Structure and Reactivity*, 4th Editio.; 1993.

(14) Klein, D. *Organic Chemistry*, 3rd ed.; 2017; Vol. 3. https://doi.org/10.1002/9780470771044.ch11.

(15) S. Obiri*, D.K. Dodoo, F. O.-S. and D. K. E. DETERMINATION OF FREE CYANIDE AND TOTAL CYANIDE h ν h ν. *Chem. Soc. Ethiop.* **2007**, *21* (2), 213–220.

(16) Song, Y.; Lei, S.; Zhou, J.; Tian, Y. Removal of Heavy Metals and Cyanide from Gold Mine Waste-Water by Adsorption and Electric Adsorption. *J. Chem.*

Technol. Biotechnol. **2016**, *91* (9), 2539–2544. https://doi.org/10.1002/jctb.4859.

(17) Pérez, R. Los Cianuros Como Veneno En La Toxicología Forense. *Gac Int Cienc Forense* **2019**, *33* (Octubre-Diciembre), 44–80.

(18) Tarras-Wahlberg, N. H.; Flachier, A.; Lane, S. N.; Sangfors, O. Environmental Impacts and Metal Exposure of Aquatic Ecosystems in Rivers Contaminated by Small Scale Gold Mining: The Puyango River Basin, Southern Ecuador. *Sci. Total Environ.* **2001**, *278* (1–3), 239–261. https://doi.org/10.1016/S0048-9697(01)00655-6.

(19) Lovasoa, C. R.; Hela, K.; Harinaivo, A. A.; Hamma, Y. Bioremediation of Soil and Water Polluted by Cyanide: A Review. *African J. Environ. Sci. Technol.* **2017**, *11* (6), 272–291. https://doi.org/10.5897/ajest2016.2264.

(20) Harari, R.; Harari, F.; Gerhardsson, L.; Lundh, T.; Skerfving, S.; Strömberg, U.; Broberg, K. Exposure and Toxic Effects of Elemental Mercury in Gold-Mining Activities in Ecuador. *Toxicol. Lett.* **2012**, *213* (1), 75–82. https://doi.org/10.1016/j.toxlet.2011.09.006.

(21) Acheampong, M. A.; Meulepas, R. J. W.; Lens, P. N. L. Removal of Heavymetals and Cyanide from Gold Mine Wastewater. *J. Chem. Technol. Biotechnol.* **2010**, *85* (5), 590–613. https://doi.org/10.1002/jctb.2358.

(22) Dash, R. R.; Gaur, A.; Balomajumder, C. Cyanide in Industrial Wastewaters and Its Removal: A Review on Biotreatment. *J. Hazard. Mater.* **2009**, *163* (1), 1–11. https://doi.org/10.1016/j.jhazmat.2008.06.051.

(23) Bolarinwa, I. F.; Orfila, C.; Morgan, M. R. A. Amygdalin Content of Seeds, Kernels and Food Products Commercially- Available in the UK. *Food Chem.* **2014**, *152*, 133–139. https://doi.org/10.1016/j.foodchem.2013.11.002.

(24) Qadir, M.; Fatima, K. Review on Pharmacological Activity of Amygdalin. *Arch. Cancer Res.* **2017**, *05* (04), 10–12. https://doi.org/10.21767/2254-6081.100160.

(25) Yildirim, F. A.; Atilla Askin, M. Variability of Amygdalin Content in Seeds of Sweet and Bitter Apricot Cultivars in Turkey. *African J. Biotechnol.* **2010**, *9* (39), 6522–6524. https://doi.org/10.4314/AJB.V9I39.

(26) Gómez, G.; Valdivieso, M. Cassava Foliage: Chemical Composition, Cyanide Content and Effect of Drying on Cyanide Elimination. *J. Sci. Food Agric.* **1985**, *36* (6), 433–441. https://doi.org/10.1002/jsfa.2740360602.

(27) Ma, J.; Dasgupta, P. K. Recent Developments in Cyanide Detection: A Review. *Anal. Chim. Acta* **2010**, *673* (2), 117–125. https://doi.org/10.1016/j.aca.2010.05.042.

(28) Surleva, A.; Drochioiu, G. A Modified Ninhydrin Micro-Assay for Determination of Total Cyanogens in Plants. *Food Chem.* **2013**, *141* (3), 2788–2794. https://doi.org/10.1016/j.foodchem.2013.05.110.

(29) Haque, M. R.; Bradbury, J. H. Total Cyanide Determination of Plants and Foods Using the Picrate and Acid Hydrolysis Methods. **2002**, *77*, 107–114.

(30) Agbesi Acheampong, M.; Jackson, A.; Okwaning, E. Physico-Chemical Characteristics of a Gold Mining Tailings Dam Wastewater. *J. Environ. Sci. Eng.*

2013, *2* (January 2013), 469–475.

(31) Randviir, E. P.; Banks, C. E. The Latest Developments in Quantifying Cyanide and Hydrogen Cyanide. *TrAC - Trends Anal. Chem.* **2015**, *64*, 75–85. https://doi.org/10.1016/j.trac.2014.08.009.

(32) Bark, L. S.; Higson, H. G. A Review of the Methods Available for the Detection and Determination of Small Amounts of Cyanide. *Analyst* **1963**, *88* (1051), 751–760. https://doi.org/10.1039/AN9638800751.

(33) Nyamunda, B. C. Review of the Impact on Water Quality and Treatment Options of Cyanide Used in Gold Ore Processing. *Water Qual.* **2017**. https://doi.org/10.5772/65706.

(34) Pohlandt, C.; Jones, E. A.; Lee, A. F. Critical Evaluation of Methods Applicable To the Determination of Cyanides. *J. South African Inst. Min. Metall.* **1983**, *83* (1), 11–19.

(35) Greene, R.; Robert, A.; Breazeale, E. The Detection and Determination of Cyanides in Water. *Am. Water Work. Assoc.* **1937**, *29* (12), 1971–1977.

(36) Cacace, D.; Ashbaugh, H.; Kouri, N.; Bledsoe, S.; Lancaster, S.; Chalk, S. Spectrophotometric Determination of Aqueous Cyanide Using a Revised Phenolphthalin Method. **2007**, *589*, 137–141. https://doi.org/10.1016/j.aca.2007.02.004.

(37) Doe-puplampu, S.; Choodum, A.; Wongniramaikul, W. Detection of Cyanide in Water by Environmentally Friendly Colorimetry with Digital Image Analysis. **2017**, *2017* (Paccon), 15–20.

(38) Schilt, A. Colorimetric Determination of Cyanide Tris(1 ,10- Phenanthroline)-Lron (II) Ion as a Selective and Sensitive Reagent. *Anal. Chem.* **1958**, *30* (8), 1409–1411. https://doi.org/10.1021/ac60075a018.

(39) Skoog, D. A.; Holler, J. F.; Crouch, S. R. *Principios de Análsis Instrumental*; 2008; Vol. 53.

(40) Burgot, J.-L. Ionic Equilibria in Analytical Chemistry. *Ion. Equilibria Anal. Chem.* **2012**, *9781441983*, 1–770. https://doi.org/10.1007/978-1-4419-8382-4.

(41) Nava-Alonso, F.; Elorza-Rodríguez, E.; Uribe-Salas, A.; Pérez-Garibay, R. Análisis Químico de Cianuro En El Proceso de Cianuració n Revisión de Los Principales Métodos. *Rev. Metal.* **2007**, *43* (1), 20–28. https://doi.org/10.3989/revmetalm.2007.v43.i1.48.

(42) Michaowski, T.; Asuero, A. G.; Ponikvar-Svet, M.; Toporek, M.; Pietrzyk, A.; Rymanowski, M. Liebig-Denigès Method of Cyanide Determination: A Comparative Study of Two Approaches. *J. Solution Chem.* **2012**, *41* (7), 1224–1239. https://doi.org/10.1007/s10953-012-9864-x.

(43) Breuer, P. L.; Sutcliffe, C. A.; Meakin, R. L. Hydrometallurgy Cyanide Measurement by Silver Nitrate Titration : Comparison of Rhodanine and Potentiometric End-Points. *Hydrometallurgy* **2011**, *106* (3–4), 135–140. https://doi.org/10.1016/j.hydromet.2010.12.008.

(44) Barnes, D. E.; Wright, P. J.; Graham, S. M.; Jones-Watson, E. A. Techniques for

the Determination of Cyanide in a Process Environment: A Review. *Geostand. Newsl.* **2000**, *24* (2), 183–195. https://doi.org/10.1111/j.1751-908X.2000.tb00770.x.

(45) Wu, W.; Xiao, Q.; Zhang, P.; Ye, M.; Wan, Y.; Liang, H. Rapid Measurement of Free Cyanide in Liquor by Ion Chromatography with Pulsed Amperometric Detection. *Food Chem.* **2015**, *172*, 681–684. https://doi.org/10.1016/j.foodchem.2014.09.052.

(46) Sumiyoshi, K.; Yagi, T.; Nakamura, H. Determination of Cyanide by High-Performance Liquid Chromatography Using Postcolumn Derivatization with o-Phthalaldehyde. *J. Chromatogr. A* **1995**, *690* (1), 77–82. https://doi.org/10.1016/0021-9673(94)00976-G.

(47) Kruse, J. M.; Mellon, M. G. Colorimetric Determination of Cyanide and Thiocyanate. *Anal. Chem.* **1953**, *25* (3), 446–450. https://doi.org/10.1021/ac60075a018.

(48) Pope, A.; Boulevard, H. O. Preliminary Data Search Report for Locating and Estimating Air Emissions From Sources Of. **1993**, No. September.

(49) Gail, E.; Gos, S.; Kulzer, R.; Lorösch, J.; Rubo, A.; Sauer, M. Cyano Compounds, Inorganic. *Ullmann's Encycl. Ind. Chem.* **2004**. https://doi.org/10.1002/14356007.a08_159.pub2.

(50) Khare, B. N.; Sagan, C.; Thompson, W. R.; Arakawa, E. T.; Meisse, C.; Tuminello, P. S. Optical Properties of Poly-HCN and Their Astronomical Applications. *Can. J. Chem.* **1994**, *72* (9), 678–694. https://doi.org/10.1139/v94-093.

(51) Pirie, J. The Manufacture of Hydrocyanic Acid by the Andrussow Process. *Anatolia* **1958**, *2* (1), 146–147. https://doi.org/10.1080/13032917.2017.1416216.

(52) d'Ischia, M.; Manini, P.; Moracci, M.; Saladino, R.; Ball, V.; Thissen, H.; Evans, R. A.; Puzzarini, C.; Barone, V. Astrochemistry and Astrobiology: Materials Science in Wonderland? *Int. J. Mol. Sci.* **2019**, *20* (17). https://doi.org/10.3390/ijms20174079.

(53) Tian, F.; Kasting, J. F.; Zahnle, K. Revisiting HCN Formation in Earth's Early Atmosphere. *Earth Planet. Sci. Lett.* **2011**, *308* (3–4), 417–423. https://doi.org/10.1016/j.epsl.2011.06.011.

(54) Das, T.; Ghule, S.; Vanka, K. Insights into the Origin of Life: Did It Begin from HCN and H2O? *ACS Cent. Sci.* **2019**, *5* (9), 1532–1540. https://doi.org/10.1021/acscentsci.9b00520.

(55) Villafañe-Barajas, S. A.; Colín-García, M.; Negrón-Mendoza, A.; Ruiz-Bermejo, M. An Experimental Study of the Thermolysis of Hydrogen Cyanide: The Role of Hydrothermal Systems in Chemical Evolution. *Int. J. Astrobiol.* **2020**, *19* (5), 369–378. https://doi.org/10.1017/S1473550420000142.

(56) Ruiz-Bermejo, M.; De, L.; Cristina, P.; Mateo-mart, E. A Comprehensive Review of HCN-Derived Polymers. **2021**.

(57) Matthews, C. The HCN World: Establishing Protein – Nucleic Acid Life via Hydrogen Cyanide Polymers. *Environ. Chem.* **2004**.

(58) Adams, M. D.; Kyle, J. H. Precipitation of Cyanide as Cu2Fe(CN)6 Compounds from Cyanidation and Detoxification Circuits. *Australas. Inst. Min. Metall. Publ. Ser.* **2000**, No. 5, 201–206.

(59) Samain, L.; Grandjean, F.; Long, G. J.; Martinetto, P.; Bordet, P.; Strivay, D. Relationship between the Synthesis of Prussian Blue Pigments, Their Color, Physical Properties, and Their Behavior in Paint Layers. *J. Phys. Chem. C* **2013**, *117* (19), 9693–9712. https://doi.org/10.1021/jp3111327.

(60) Yang, Y.; Ph, D.; Brownell, C.; Sadrieh, N.; Ph, D.; May, J.; Ph, D.; Grosso, A. D. E. L.; Ph, D.; Place, D.; Ph, D.; Leutzinger, E.; Ph, D.; Duffy, E.; Ph, D.; He, R.; Houn, F.; Lyon, R.; Ph, D.; Faustino, P.; Ph, D. Quantitative Measurement of Cyanide Released from Prussian Blue. **2007**, 776–781. https://doi.org/10.1080/15563650601181562.

(61) Karyakin, A. A. Prussian Blue and Its Analogues : Electrochemistry and Analytical Applications. **2001**, No. 10, 813–819.

(62) Lejeune, J.; Brubach, J.; Roy, P.; Bleuzen, A. Application of the Infrared Spectroscopy to the Structural Study of Prussian Blue Analogues. *Comptes rendus - Chim.* **2014**, *17* (6), 534–540. https://doi.org/10.1016/j.crci.2014.01.017.

(63) Verdaguer, M.; Galvez, R.; Desplanches, C. Electrons at Prussian Blue Work in Analogues. *Electrochem. Soc. Interface* **2002**, No. c, 29–32.

(64) Verdaguer, M.; Girolami, G. *Magnetic Prussian Blue Analogs Prussian Blue Analogs (PBA), Brief History , Synthesis*; 2004.

(65) Yi, H.; Qin, R.; Ding, S.; Wang, Y.; Li, S.; Zhao, Q.; Pan, F. Structure and Properties of Prussian Blue Analogues in Energy Storage and Conversion Applications. *Adv. Funct. Mater.* **2021**, *31* (6), 1–25. https://doi.org/10.1002/adfm.202006970.

(66) Zentkova, M.; Mihalik, M. The Effect of Pressure on Magnetic Properties of Prussian Blue Analogues. *Crystals* **2019**, *9* (2). https://doi.org/10.3390/cryst9020112.

(67) Li, W.; Han, C.; Cheng, G.; Chou, S.; Liu, H.; Dou, S. Chemical Properties , Structural Properties , and Energy Storage Applications of Prussian Blue Analogues. **2019**, *1900470*, 1–21. https://doi.org/10.1002/smll.201900470.

(68) Chen, J.; Wei, L.; Mahmood, A.; Pei, Z.; Zhou, Z.; Chen, X.; Chen, Y. Prussian Blue, Its Analogues and Their Derived Materials for Electrochemical Energy Storage and Conversion. *Energy Storage Mater.* **2020**, *25*, 585–612. https://doi.org/10.1016/j.ensm.2019.09.024.

(69) Rasmussen, P. G.; Meyers, E. A. AN INVESTIGATION OF PRUSSIAN BLUE ANALOGUES BY MC) SSBAUER SPECTROSCOPY AND MAGNETIC SUSCEPTIBILITY. **1984**, *3* (2).

(70) Kaye, S. S.; Long, J. R. The Role of Vacancies in the Hydrogen Storage Properties of Prussian Blue Analogues. *Catal. Today* **2007**, *120* (3-4 SPEC. ISS.), 311–316. https://doi.org/10.1016/j.cattod.2006.09.018.

(71) Preisner, M.; Neverova-Dziopak, E.; Kowalewski, Z. An Analytical Review of Different Approaches to Wastewater Discharge Standards with Particular

Emphasis on Nutrients. *Environ. Manage.* **2020**, *66* (4), 694–708. https://doi.org/10.1007/s00267-020-01344-y.

(72) Mamani, E. Implementción de Procesos de Destrucción de Cianuro de Los Efluentes de La Minería Artesanal En La Rinconada-Puno, Universidad nacional de san agustin escuela profesional ambiental, 2013, Vol. 8.

(73) Vela-Almeida, D.; Kolinjivadi, V.; Kosoy, N. The Building of Mining Discourses and the Politics of Scale in Ecuador. *World Dev.* **2018**, *103*, 188–198. https://doi.org/10.1016/j.worlddev.2017.10.025.

(74) Roy, B. A.; Zorrilla, M.; Endara, L.; Thomas, D. C.; Vandegrift, R.; Rubenstein, J. M.; Policha, T.; Ríos-Touma, B.; Read, M. New Mining Concessions Could Severely Decrease Biodiversity and Ecosystem Services in Ecuador. *Trop. Conserv. Sci.* **2018**, *11*. https://doi.org/10.1177/1940082918780427.

(75) Sandoval, F. Small-Scale Mining in Ecuador. *Mining, Miner. Sustain. Dev.* **2001**, *75* (75), 28.

(76) Pereyra, G. Sector Minería. *Boletín Científico la Esc. Super. Atotonilco Tula* **2015**, *2* (4). https://doi.org/10.29057/esat.v2i4.1469.

(77) Warnaars, X. S. Why Be Poor When We Can Be Rich? Constructing Responsible Mining in El Pangui, Ecuador. *Resour. Policy* **2012**, *37* (2), 223–232. https://doi.org/10.1016/j.resourpol.2011.10.001.

(78) Enami EP. *Ecuador Mining Country 2020*; 2020.

(79) Rodrigues, D.; Rocha-Santos, T. A. P.; Freitas, A. C.; Gomes, A. M. P.; Duarte, A. C. Strategies Based on Silica Monoliths for Removing Pollutants from Wastewater Effluents: A Review. *Sci. Total Environ.* **2013**, *461–462*, 126–138. https://doi.org/10.1016/j.scitotenv.2013.04.091.

(80) Galarneau, A.; Sachse, A.; Said, B.; Pelisson, C. H.; Boscaro, P.; Brun, N.; Courtheoux, L.; Olivi-Tran, N.; Coasne, B.; Fajula, F. Les Monolithes Siliciques à Porosité Hiérarchique: Une Nouvelle Classe de Microréacteurs Pour l'Intensification Des Procédés En Catalyse et En Adsorption. *Comptes Rendus Chim.* **2016**, *19* (1–2), 231–247. https://doi.org/10.1016/j.crci.2015.05.017.

(81) Causse, J.; Tokarev, A.; Ravaux, J.; Moloney, M.; Barré, Y.; Grandjean, A. Facile One-Pot Synthesis of Copper Hexacyanoferrate Nanoparticle Functionalised Silica Monoliths for the Selective Entrapment of 137Cs. *J. Mater. Chem. A* **2014**, *2* (25), 9461–9464. https://doi.org/10.1039/c4ta01266f.

(82) Cameron, N.; Sherrinton, D. High Internal Phase Emulsions (HIPEs)- Structure, Properties and Use in Polymer Preparation. **1996**, *126*.

(83) Sommer-Marquez, A.; Mansas, C.; Talha, N.; Rey, C.; Causse, J. Reinforced Silica Monoliths Functionalised with Metal Hexacyanoferrates for Cesium Decontamination: A Combination of a One-Pot Procedure and Skeleton Calcination. *RSC Adv.* **2016**, *6* (77), 73475–73484. https://doi.org/10.1039/c6ra16980e.

(84) Mayer, M.; Dedovets, D.; Guari, Y.; Larionova, J.; Long, J.; Causse, J. Journal of Colloid and Interface Science Synthesis of Poly (Diallyldimethylammonium) Capped Copper Hexacyanoferrate (CuHCF) Nanoparticles : An Efficient

Stabiliser for Pickering Emulsions. *J. Colloid Interface Sci.* **2017**, *505*, 364–372. https://doi.org/10.1016/j.jcis.2017.05.113.

(85) Cartes, P.; Pereira, J. C. Emulsiones Como Agentes Templantes Empleados En La Elaboración de Materiales Porosos. *Rev. Ing. UC* **2016**, *23* (3), 308–318.

(86) Vaca, A. Encapsulation of Photosynthetic Plant Cells within Hierarchical Silica Monolith Enriched with Chlorophyll a by High Internal Phase Emulsion (HIPE) for CO2 Adsorption, Universidad de Investigación de Tecnología Experimental Yachay, 2020.

(87) López, N. Algae Encapsulation into Silica Monoliths Synthesized by High Internal Phase Emulsions (HIPE), Universidad de Investigación de Tecnología Experimental Yachay, 2020.

(88) Terán, D. Environmental Water Depollution by Using Hierarchically Textured Hybrids Algae-Silica Monoliths, Universidad de Investigación de Tecnología Experimental Yachay, 2021.

(89) Tipán, A. Possibility of Reusing Industrial Waste to Synthesize a Depolluting Silica Monolith through HIPE Method : An Experimental and Theoretical Study, Universidad de Investigación de Tecnología Experimental Yachay, 2020.

(90) Carn, F.; Colin, A.; Achard, M.; Sellier, E.; Birot, M.; Recherche, C. De; Pascal, P.; Schweitzer, A. A.; E-mail, F.; E-mail, F. Inorganic Monoliths Hierarchically Textured via Concentrated Direct Emulsion and Micellar Templates {. **2004**, 1370–1376.

(91) Callister, W.; Rethwisch, D. Materials Science. *Phys. Educ.* **2014**, *9* (2), 70–71. https://doi.org/10.1088/0031-9120/5/2/304.

(92) Aguilar-Marín, P.; Angelats-Silva, L.; Noriega-Diaz, E.; Chavez-Bacilio, M.; Verde-Vera, R. Understanding the Phenomenon of X-Ray Diffraction by Crystals and Related Concepts. *Eur. J. Phys.* **2020**, *41* (4). https://doi.org/10.1088/1361-6404/ab8e53.

(93) Moore, E.; Smart, L. *Solid State Chemistry*, Third.; 2005.

(94) Pavia, D.; Lampman, G.; Kriz, G.; Vyvyan, J. *Introduction to Spectroscopy*, Fifth.; 2013: Bellingham, 2013. https://doi.org/10.1887/0750303468/b293c1.

(95) Hummel, R. E. Differential Reflectance Spectroscopy in Analysis of Surfaces. *Encycl. Anal. Chem.* **2000**, 1–24. https://doi.org/10.1002/9780470027318.a2504.

(96) Blitz, J. *Diffuse Reflectance Spectroscopy*; 1971; Vol. 2. https://doi.org/10.1080/10408347108542764.

(97) Musić, S.; Filipović-Vinceković, N.; Sekovanić, L. Precipitation of Amorphous SiO2 Particles and Their Properties. *Brazilian J. Chem. Eng.* **2011**, *28* (1), 89–94. https://doi.org/10.1590/S0104-66322011000100011.

(98) Prabhakaran, D.; Subashini, C.; Akhila Maheswari, M. Synthesis of Mesoporous Silica Monoliths - A Novel Approach towards Fabrication of Solid-State Optical Sensors for Environmental Applications. *Int. J. Nanosci.* **2016**, *15* (5–6). https://doi.org/10.1142/S0219581X16600140.

(99) Tenkyong, T.; Bachan, N.; Raja, J.; Kumar, P. N.; Shyla, J. M. Investigation of

Sol-Gel Processed CuO/SiO2 Nanocomposite as a Potential Photoanode Material. *Mater. Sci. Pol.* **2015**, *33* (4), 826–834. https://doi.org/10.1515/msp-2015-0097.

(100) Tohidi, S. H.; Gholamzadeh, S.; Shirazi, M. A. Z.; Novinrooz, A. J. Characterization of Sol–Gel Derived CuO/SiO2 Nanostructure on Temperature. *Int. J. Ind. Chem.* **2014**, *5* (3–4), 63–68. https://doi.org/10.1007/s40090-014-0017-5.

(101) Yang, H.; Xiao, Y.; Liu, K.; Feng, Q. Chemical Precipitation Synthesis and Optical Properties of ZnO/SiO 2 Nanocomposites. *J. Am. Ceram. Soc.* **2008**, *91* (5), 1591–1596. https://doi.org/10.1111/j.1551-2916.2008.02340.x.

(102) Ishii, A.; Torii;, A.; H., I.; T., K.; Mizoguchi, Y. Kodera, A.; Matsushima, K.; Inada, Y. Photostabilization of Chlorophyll a Adsorbed onto Smectite. **1995**, *28* (1), 77–82.

(103) Yi, Z.; Jiang, T.; Cheng, Y.; Tang, Q. Effect of SiO2aerogels Loading on Photocatalytic Degradation of Nitrobenzene Using Composites with Tetrapod-like ZnO. *Nanotechnol. Rev.* **2020**, *9* (1), 1009–1016. https://doi.org/10.1515/ntrev-2020-0081.

(104) Lacombe, S.; Cardy, H.; Soggiu, N.; Blanc, S.; Habib-Jiwan, J. L.; Soumillion, J. P. Diffuse Reflectance UV-Visible Spectroscopy for the Qualitative and Quantitative Study of Chromophores Adsorbed or Grafted on Silica. *Microporous Mesoporous Mater.* **2001**, *46* (2–3), 311–325. https://doi.org/10.1016/S1387-1811(01)00315-8.

(105) Lopez, T.; Villa, M.; Gomez, R. UV-Vis Diffuse Reflectance Spectroscopic Study of Pt, Pd, and Ru Catalysts Supported on Silica. *J. Phys. Chem.* **1991**, *95* (4), 1690–1693. https://doi.org/10.1021/j100157a038.

(106) Sarkar, J.; Manna, S.; Mukherje, S.; Das, G. Study on the Biostability of Chlorophyll a Entrapped in Silica Gel Nanomatrix. **2009**, 1068–1072. https://doi.org/10.1007/s10854-008-9827-6.

(107) Mayerhöfer, T.; Zhijian, S.; Leonova, E.; Edén, M.; Kriltz, A. Journal of Solid State Chemistry Consolidated Silica Glass from Nanoparticles. **2008**, *181*, 2442–2447. https://doi.org/10.1016/j.jssc.2008.06.011.

(108) Torrent, J.; Barrón, V. Diffuse Reflectance Spectroscopy of Iron Oxides. **2002**.

(109) Yang, H.; Sun, L.; Zhai, J.; Li, H.; Zhao, Y.; Yu, H. In Situ Controllable Synthesis of Magnetic Prussian Blue/Graphene Oxide Nanocomposites for Removal of Radioactive Cesium in Water. *J. Mater. Chem. A* **2014**, *2* (2), 326–332. https://doi.org/10.1039/c3ta13548a.

(110) Lv, Y.-X.; Zhang, L. H.; Li, X. P.; Zhang, X. Photoinduced Chromism of a Zinc–Iron Cyanide at Room Temperature. *Inorg. Chem. Commun.* **2017**, *76*, 44–47. https://doi.org/10.1016/j.inoche.2017.01.007.

(111) Muñoz, E. C.; Henríquez, R. G.; Córdova, R. A.; Schrebler, R. S.; Cisternas, R.; Ballesteros, L.; Marotti, R. E.; Dalchiele, E. A. Photoelectrochemical and Optical Characterization of Prussian Blue onto P-Si(100). *J. Solid State Electrochem.* **2012**, *16* (1), 165–171. https://doi.org/10.1007/s10008-010-1287-2.

(112) Tabbì, G.; Giuffrida, A.; Bonomo, R. P. Determination of Formal Redox Potentials

in Aqueous Solution of Copper(II) Complexes with Ligands Having Nitrogen and Oxygen Donor Atoms and Comparison with Their EPR and UV-Vis Spectral Features. *J. Inorg. Biochem.* **2013**, *128*, 137–145. https://doi.org/10.1016/j.jinorgbio.2013.07.035.

(113) Parma, A.; Freris, I.; Riello, P.; Cristofori, D. Structural and Magnetic Properties of Mesoporous SiO 2 Nanoparticles Impregnated with Iron Oxide or Cobalt-Iron Oxide Nanocrystals. *J. Mater. Chem.* **2012**, *22*, 19276–19288. https://doi.org/10.1039/c2jm32314a.

(114) Nielsen, P.; Dresow, B.; Heinrich, H. C. In Vitro Study of 137Cs Sorption by Hexacyanoferrates(II). *Zeitschrift fur Naturforsch. - Sect. B J. Chem. Sci.* **1987**, *42* (11), 1451–1460. https://doi.org/10.1515/znb-1987-1114.

(115) Bustos, E.; Godínez, L. A. Modified Surfaces with Nano-Structured Composites of Prussian Blue and Dendrimers. New Materials for Advanced Electrochemical Applications. *Int. J. Electrochem. Sci.* **2011**, *6* (1), 1–36.

(116) Ojwang, D. O.; Grins, J.; Wardecki, D.; Valvo, M.; Renman, V.; Häggström, L.; Ericsson, T.; Gustafsson, T.; Mahmoud, A.; Hermann, R. P.; Svensson, G. Structure Characterization and Properties of K-Containing Copper Hexacyanoferrate. *Inorg. Chem.* **2016**, *55* (12), 5924–5934. https://doi.org/10.1021/acs.inorgchem.6b00227.

(117) Martínez-García, R.; Knobel, M.; Goya, G.; Gimenez, M. C.; Romero, F. M.; Reguera, E. Heat-Induced Charge Transfer in Cobalt Iron Cyanide. *J. Phys. Chem. Solids* **2006**, *67* (11), 2289–2299. https://doi.org/10.1016/j.jpcs.2006.05.045.

(118) Fukaya, R.; Asahara, A.; Ishige, S.; Nakajima, M.; Tokoro, H.; Ohkoshi, S. I.; Suemoto, T. Probing of Local Structures of Thermal and Photoinduced Phases in Rubidium Manganese Hexacyanoferrate by Resonant Raman Spectroscopy. *J. Chem. Phys.* **2013**, *139* (8), 0–7. https://doi.org/10.1063/1.4818809.

(119) Fukaya, R.; Nakajima, M.; Tokoro, H.; Ohkoshi, S.; Suemoto, T. Photoinduced Charge-Transfer Process in Rubidium Manganese Hexacyanoferrate Probed by Raman Spectroscopy. *J. Chem. Phys.* **2009**, *131* (15), 1–10. https://doi.org/10.1063/1.3245863.

(120) Sciacca, R.; Zamponi, S.; Berrettoni, M.; Giorgetti, M. Stable Films of Zinc-Hexacyanoferrate: Electrochemistry and Ion Insertion Capabilities. *J. Solid State Electrochem.* **2021**, No. 0123456789. https://doi.org/10.1007/s10008-021-05005-w.

(121) Jassal, V.; Shanker, U.; Kaith, B. S.; Shankar, S. Green Synthesis of Potassium Zinc Hexacyanoferrate Nanocubes and Their Potential Application in Photocatalytic Degradation of Organic Dyes. *RSC Adv.* **2015**, *5* (33), 26141–26149. https://doi.org/10.1039/c5ra03266k.

(122) Mink, J.; Stirling, A.; Ojwang, D. O.; Svensson, G.; Mihály, J.; Németh, C.; Drees, M.; Hajba, L. Vibrational Properties and Bonding Analysis of Copper Hexacyanoferrate Complexes in Solid State. *Appl. Spectrosc. Rev.* **2019**, *54* (5), 369–424. https://doi.org/10.1080/05704928.2018.1459659.

(123) Pajerowski, D. M.; Watanabe, T.; Yamamoto, T.; Einaga, Y. Electronic Conductivity in Berlin Green and Prussian Blue. *Phys. Rev. B - Condens. Matter*

Mater. Phys. **2011**, *83* (15), 3–6. https://doi.org/10.1103/PhysRevB.83.153202.

(124) Barsan, M. M.; Butler, I. S.; Fitzpatrick, J.; Gilson, D. F. R. High-Pressure Studies of the Micro-Raman Spectra of Iron Cyanide Complexes: Prussian Blue (Fe4[Fe(CN)6]3), Potassium Ferricyanide (K3[Fe(CN)6]), and Sodium Nitroprusside (Na2[Fe(CN)5(NO)]·2H2O). *J. Raman Spectrosc.* **2011**, *42* (9), 1820–1824. https://doi.org/10.1002/jrs.2931.

(125) Srivastava, R.; Srinivas, D.; Ratnasamy, P. Fe-Zn Double-Metal Cyanide Complexes as Novel, Solid Transesterification Catalysts. *J. Catal.* **2006**, *241* (1), 34–44. https://doi.org/10.1016/j.jcat.2006.04.002.

(126) Khan, Z. Synthesis, Characterization, and In-Vitro Anti-Microbial and Anti-Oxidant Activities of Co+2, Ni+2, Cu+2 and Zn+2 Complexes of 5-Chloro-2-Hydroxybenzaldehyde-N-(2-Oxo-1,2-Dihydro-3H-Indol-3-Ylidene)Hydrazone. *Pakistan J. Chem.* **2015**, *5* (3), 143–149. https://doi.org/10.15228/2015.v05.i03.p07201509310955.

(127) Rani, M.; Shanker, U. Removal of Chlorpyrifos, Thiamethoxam, and Tebuconazole from Water Using Green Synthesized Metal Hexacyanoferrate Nanoparticles. *Environ. Sci. Pollut. Res.* **2018**, *25* (11), 10878–10893. https://doi.org/10.1007/s11356-018-1346-2.

(128) Rachna; Rani, M.; Shanker, U. Sunlight Active ZnO@FeHCF Nanocomposite for the Degradation of Bisphenol A and Nonylphenol. *J. Environ. Chem. Eng.* **2019**, *7* (3). https://doi.org/10.1016/j.jece.2019.103153.

(129) Simonov, A.; De Baerdemaeker, T.; Boström, H. L. B.; Ríos Gómez, M. L.; Gray, H. J.; Chernyshov, D.; Bosak, A.; Bürgi, H. B.; Goodwin, A. L. Hidden Diversity of Vacancy Networks in Prussian Blue Analogues. *Nature* **2020**, *578* (7794), 256–260. https://doi.org/10.1038/s41586-020-1980-y.

(130) Ye, S.; Neese, F. The Unusual Electronic Structure of Dinitrosyl Iron Complexes. **2010**, 3646–3647.

(131) McDonald, W.; Philips, D.; Mower, H. An Electron Spin Resonance Study of Some Complexes of Iron, Nitric Oxide, and Anionic Ligands. **1961**, *1* (4), 268–273.

(132) Tang, P. Semiconductor Composite Materials for Energy Storage and Conversion Applications, Universitat Autònoma de Barcelona, 2018.

(133) Bleuzen, A.; Escax, V.; Ferrier, A.; Villain, F.; Verdaguer, M.; Münsch, P. Thermally Induced Electron Transfer in a CsCoFe Prussian Blue Derivative: The Specific Role of the Alkali-Metal Ion. *Zuschriften* **2004**, 3814–3817. https://doi.org/10.1002/ange.200460086.

(134) Adhikamsetty, K.; Jonnalagadda, S. KINETICS AND MECHANISM OF PRUSSIAN BLUE FORMATION. *Chem. Soc. Ethiop.* **2008**, *23* (1), 47–54.

(135) Deshmukh, P.; Bhatt, J.; Peshwe, D.; Pathak, S. Determination of Silica Activity Index and XRD, SEM and EDS Studies of Amorphous SiO 2 Extracted from Rice Husk Ash. *Trans. Indian Inst. Met.* **2012**, *65* (1), 63–70. https://doi.org/10.1007/s12666-011-0071-z.

(136) Yu, H.; Wang, R.; Guo, J.; Li, J.; Yang, X. Color-Inducing Elements Mechanisms

in Nephrites from Golmud, Qinghai, NW China: Insights from Spectroscopic and Compositional Analyses. **2016**. https://doi.org/10.2465/jmps.151103.

(137) Yu, Y.; Shu, T.; Dong, C. A Convenient Colorimetric and Ratiometric Fluorescent Probe for Detection of Cyanide Based on BODIPY Derivative in Aqueous Media. *Anal. Chem. Res.* **2017**, *12*, 34–39. https://doi.org/10.1016/j.ancr.2017.01.004.

(138) Jiménez-Gallegos, J.; Rodríguez, J.; Yee, H.; Reguera, E. Structure of Porous Copper Prussian Blue Analogues : Nature of Their High H 2 Storage Capacity. **2010**, 5043–5048.

(139) Yuan, X.; Zhou, C.; Jing, Q.; Tang, Q.; Mu, Y.; Du, A. Facile Synthesis of G-C3N4 Nanosheets/ZnO Nanocomposites with Enhanced Photocatalytic Activity in Reduction of Aqueous Chromium(VI) under Visible Light. *Nanomaterials* **2016**, *6* (9). https://doi.org/10.3390/nano6090173.
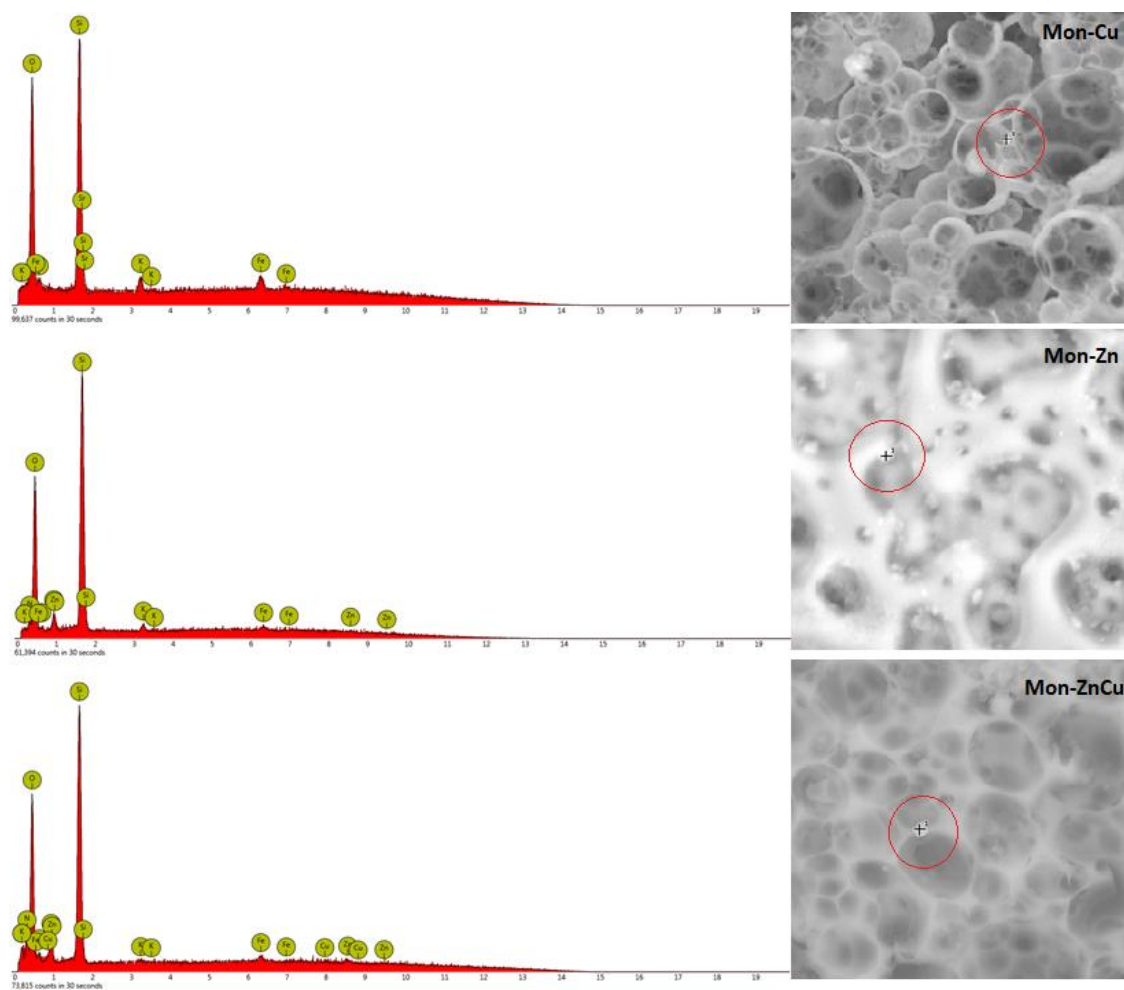
Appendix:

Appendix 1 EDX analysis for the pyrolyzed metal functionalized silica monoliths.
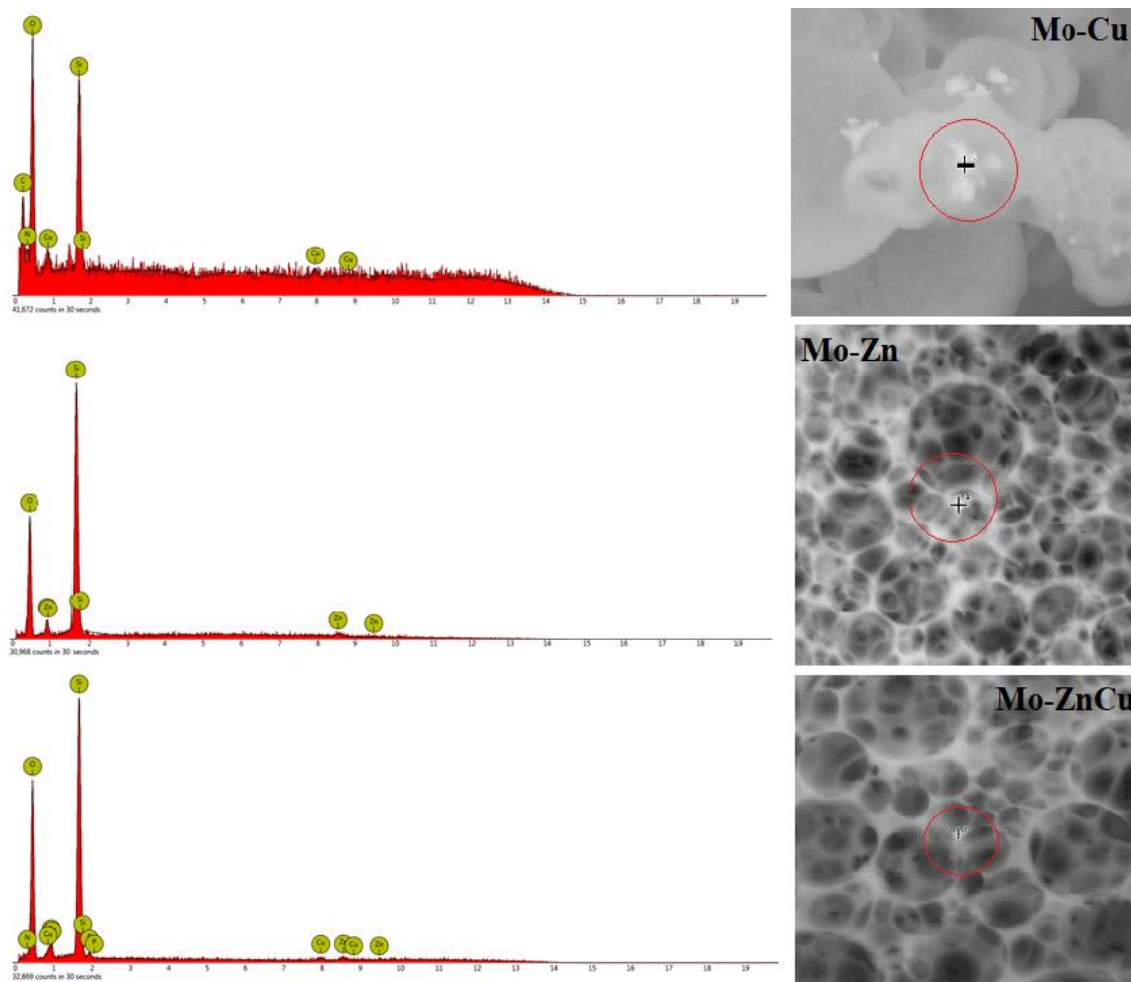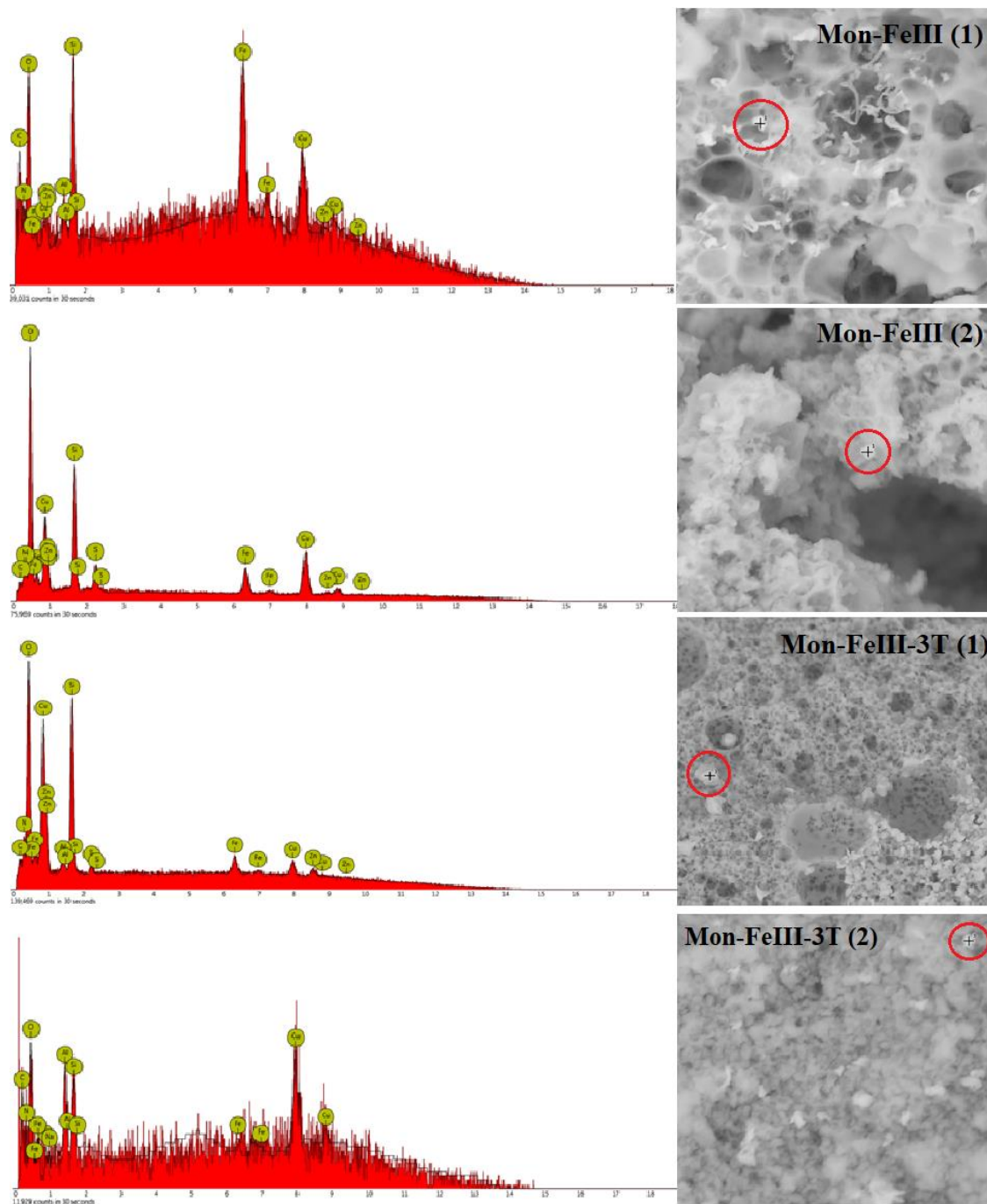
Appendix 2 EDX analysis for the PBA's functionalized   silica monoliths after the impregnation contact with potassium ferrocyanide.

Appendix 3 EDX analysis for Fe(III) functionalized silica monoliths after the impregnation by laminar flux of synthetic water.

Appendix 4 EDX analysis for Fe(II) functionalized silica monoliths after the impregnation by laminar flux of synthetic water.
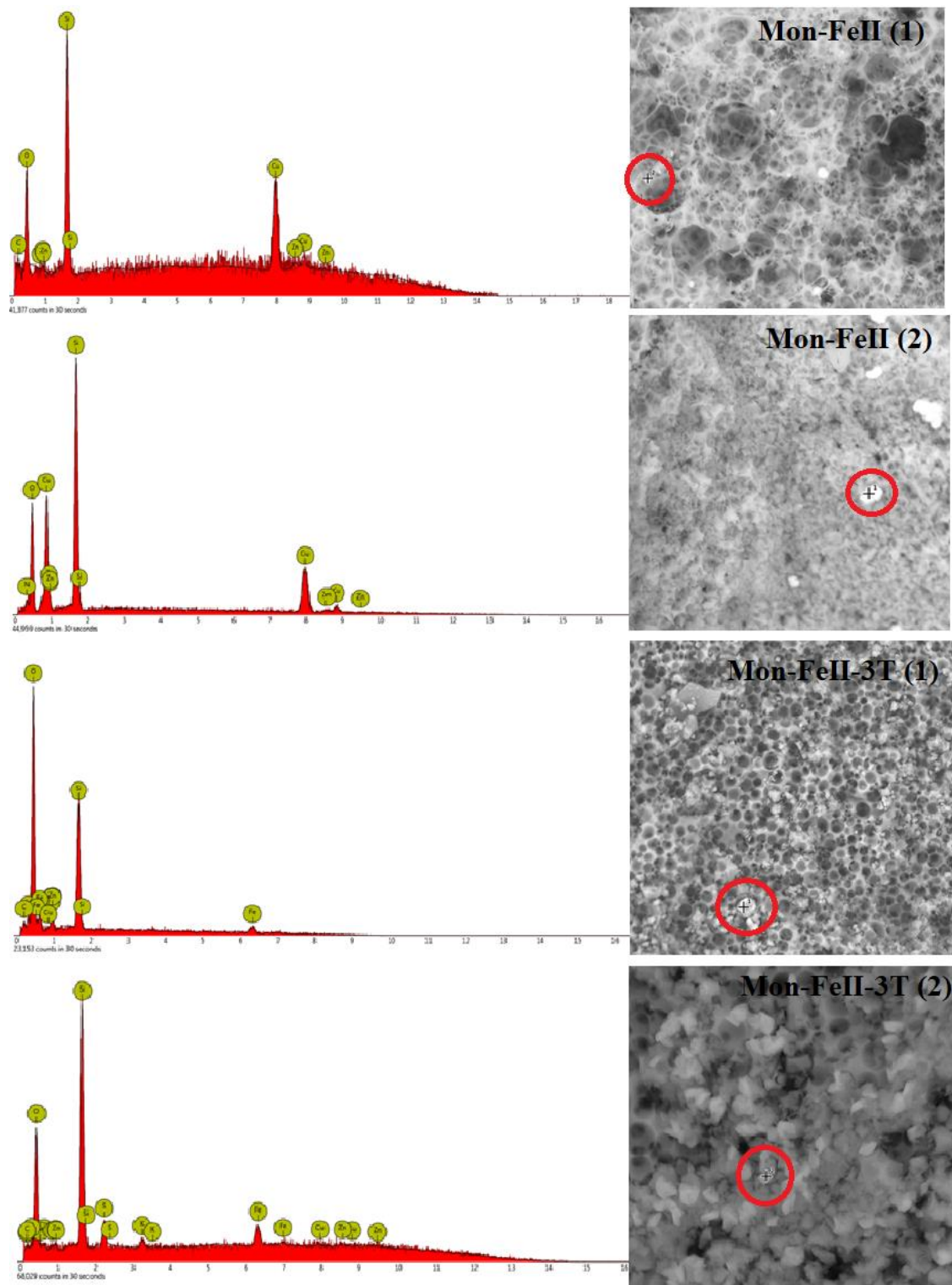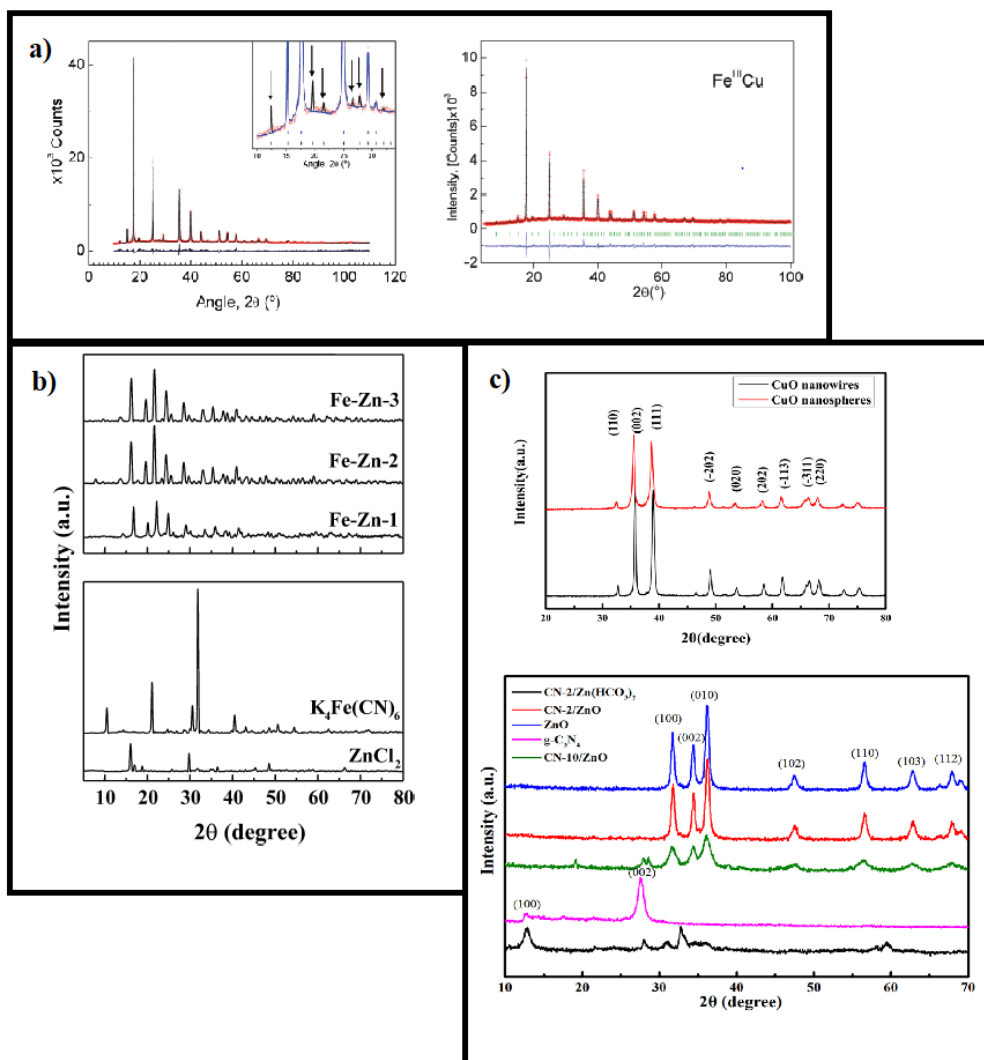
Appendix 5 (a) Diffuse reflectance spectra for Mo-Zn measured (b) Tauc plots. The linear region is extrapolated to the x-axis to extract the estimated optical band gap (red lines).
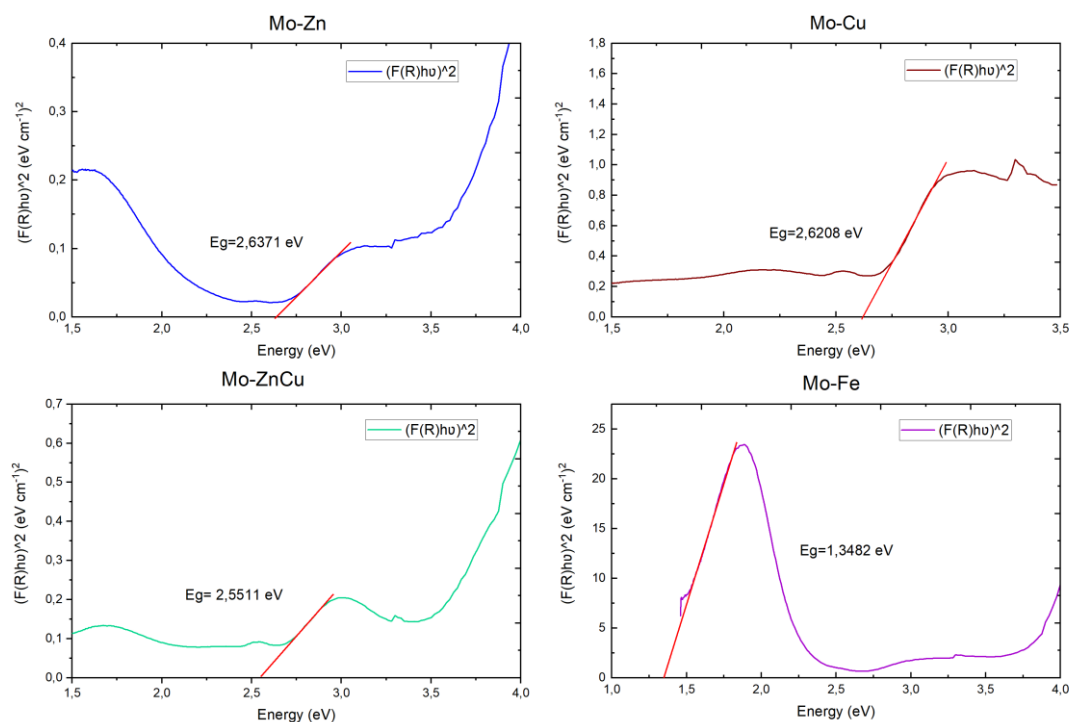
Appendix 6 Calibration curve for magnetic susceptibility measurements.
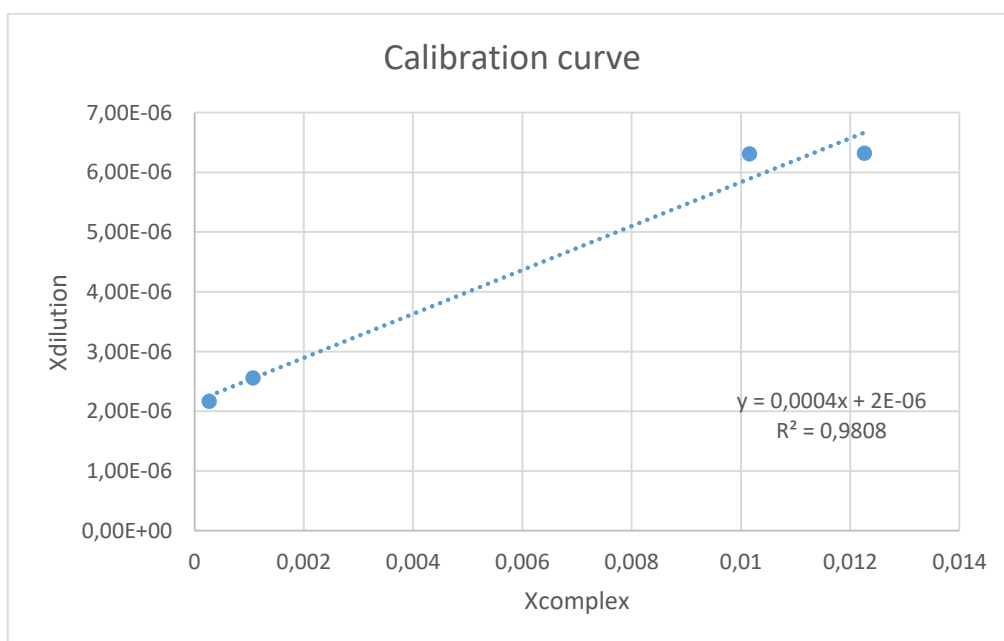
Appendix 7 XRD patterns for: a) cyano complex with Cu, b) cyano complex with Zn, c) Cu-Zn oxides [125,138,139]

Appendix 8 Calibration curve of titration method.

Calibration curve

y = 13,604x + 0,2315
R² = 0,9972